Supersonic Multi-Objective Optimization of a Rocket Based Combined Cycle Inlet By Differential Evolution

by

Craig Jee

A Thesis submitted to
the Faculty of Graduate Studies and Research
in partial fulfilment of
the requirements for the degree of
Master of Applied Science
in

Aerospace Engineering
Department of Mechanical and Aerospace Engineering
Carleton University
Ottawa, Ontario, Canada
TBA 2018

The undersigned recommend to

the Faculty of Graduate Studies and Research

acceptance of the Thesis

Supersonic Multi-Objective Optimization of a Rocket Based Combined Cycle Inlet By Differential Evolution

Submitted by **Craig Jee**

in partial fulfilment of the requirements for the degree of

Master of Science

Dr. Jason Etele, Supervisor

R. Miller, Department Chair

Carleton University

2018

Abstract

The use of differential evolution (DE) is investigated for the optimization of a novel rocket based combined cycle (RBCC) engine inlet, over the supersonic flight regime. An RBCC engine is designed to incorporate the advantages of both rocket propulsion and airbreathing engines. This novel design is the result of ongoing research, at Carleton University, to improve the efficiency of future single stage to orbit engine designs. This novel inlet design, referred to as the exchange inlet, is designed to entrain air using a semi-annular rocket-ejector exhaust profile. The purpose of the exchange inlet is to increase the air mass flow and air/fuel mixing over existing rocket ejector/RBCC designs. In addition, by using a single circular rocket throat the exchange inlet is designed to be compatible with existing rockets.

In supersonic flight, the exchange inlet external geometry generates shock waves which affect both the air mass flow and total pressure recovery of the entrained air. The geometry of the exchange inlet is controlled by 8 normalized input variables. Using these 8 input variables to create both an internal (rocket path) and external geometry, results in 100 million possibilities in design geometries. Since investigating each geometry is not practical, DE is used to find near optimal solutions. By treating each unique exchange inlet geometry as an individual in a population, the DE algorithm can narrow in on potential optimal designs using a process similar to natural selection. As there are multiple design objectives, each individual design is evaluated using a weighted sum method to determine how fit (or optimal) the design is. Varying

the objective weights shows the trade-off in the different optimal designs at a single flight speed. A single optimum is selected for three flight conditions M_∞=1.5, 2.5 and 3.5. By comparing their off-design performance over the supersonic flight range, each geometry is compared to determine an optimal for a fixed geometry design. The final fixed geometry design is selected to be the optimum at M_∞=2.5. In addition, a variable geometry is considered, however, it is not recommended given its added complexity for resulting minimal performance gains.

Acknowledgments

I would like to express my gratitude to my supervisor, professor J. Etele, for his guidance over the last two years on this work, and for his encouragement to attend the AIAA conference in Orlando, Fl, where I presented an earlier version of this work.

I would also like to thank my colleagues and the support staff of Carleton University for their assistance.

Table of Contents

List of Tables

List of Figures

List of Acronyms

Acronyms	Definition
CFD	Computation Fluid Dynamics
DAB	Diffusion and Afterburning
DE	Differential Evolution
EA	Evolutionary Algorithm
EI	Exchange Inlet
GA	Genetic Algorithm
L/D	Length to Diameter Ratio
RBCC	Rocket Based Combined Cycle
SMC	Simultaneous Mixing and Combustion
SSTO	Single Stage to Orbit
TBCC	Turbine Based Combined Cycle
TSTO	Two Stage to Orbit

List of Symbols

Symbols	Definition
A_{EI}	Area through which air enters the EI inlet
A_{in}	Air intake frontal area of rocket flowpath
A_{LE}	Area at the leading edge of the cowl
A_{max}	Maximum cross-sectional area of rocket exhaust plane
A_R	Rocket exhaust area
AR	Area ratio plane 2/3
$B_{j_{max}}$	Upper limit of solution individual gene
$B_{j_{min}}$	Lower limit of solution individual gene
C_r	Crossover probability
CR	Cowl lip contraction ratio
$c_{fair_{max}}$	Air path maximum fairing chord length at the cowl
$\widetilde{c}_{fair_{max}}$	Air path maximum fairing chord ratio
F	Differential weight

F_{th}	Vehicle engine thrust force
f_i^k	Fitness of an individual (i), current generation (k)
f_{best}^k	Fitness of the individual with the highest fitness value in the current generation (k)
g_0	Acceleration due to gravity
H	Objective vector
I	Total impulse
I_{sp}	Specific impulse
J_{rand}	Randomly selected gene, binomial crossover
K_a	Weight of first objective, fitness function
K_b	Weight of second objective, fitness function
K_c	Weight of third objective, fitness function
K_d	Weight of fourth objective, fitness function
K_e	Weight of fifth objective, fitness function
L_{arc}	Arc length of rocket exhaust
L_{max}	Circumference of rocket exhaust
M	Local Mach number
M_∞	Freestream Mach number
m	Population size, number of individuals per generation

$\dot{m}_a$	Air mass flow of the inlet
$\dot{m}_{max}$	Maximum theoretical air mass flow of the inlet, based on freestream conditions
m_v	Propellant mass
$\dot{m}_v$	Propellant mass flow
n	Number of genes in individual vector
P_o	Total pressure after all inlet shocks
$\overline{P_o}$	Average total pressure after all inlet shocks
P_{o_∞}	Freestream total pressure
P_∞	Freestream static pressure
R_{air}	Ideal gas constant for air
R_i	Random number for crossover selection
r_{CB_1}	Center body radius at rocket exhaust throat (plane 1)
$\widetilde{r}_{CB_1}$	Center body radius ratio
r_e	Radius of rocket exhaust at exit plane
res_j	Resolution of variable (gene) index j
r_g	Radius of rocket exhaust at gate
$\widetilde{r}_g$	Rocket gate radius ratio
$r_{NZ_{3in}}$	Inner radius of the rocket exhaust at exit plane

r_{th}	Radius of the rocket exhaust at the throat
S	Maximum number of possible solutions
T_∞	Freestream static temperature
t_3	Cowl inner wall thickness at rocket exhaust exit (plane 3)
$\widetilde{t}_3$	Cowl thickness ratio
Δt	Time over which thrust force is applied
$\boldsymbol{u_i^{k+1}}$	Potential individual of next generation
$\boldsymbol{v_i^k}$	Mutant (donor) individual for current individual and generation
w	Objective vector weight
$\boldsymbol{X^k}$	Solution population vector for the current generation
$\boldsymbol{x_i^k}$	An individual of current generation
$\boldsymbol{x_i^{k+1}}$	An individual of next generation
$\boldsymbol{x_{BEST}}$	The best individual possible (using 4 genes)
$\boldsymbol{x^*_{Best}}$	An approximate or known best individual (using 8 genes)
z_e	Depth of rocket flow path exhaust plane
z_g	Depth of rocket flow path at gate
$\widetilde{z}_g$	Rocket gate depth ratio
z_2	Depth of minimum airflow area (plane 2)

$\widetilde{z}_2$	Air path duct length ratio
Γ	Total number of solution evaluations
γ	Specific heat ratio
δ	Weighted difference vector for DE mutation
ϕ	Flow turning angle at the gate
Ψ_e	Rocket flow path exhaust arc angle
$\widetilde{\Psi}_e$	Rocket exit arc angle ratio
Ψ_g	Rocket flow path gate arc angle
$\widetilde{\Psi}_g$	Rocket gate arc angle ratio
σ	Rocket to total flow area ratio

Superscript

$*$	Throat/choked conditions
k	Index of the population generation

Subscript

cb	Center body
cs	Cone shock
d	Number of objectives
FF	Flow field
i	Individual index

j	Gene index
$r0, r1, r2$	Index of randomly selected and mutually exclusive members of the population

Chapter 1

Introduction

1.1 Overview and Motivation

The human desire to reach the stars has been embedded in our minds and civilizations throughout history, from artists, to inventors, to scientists and engineers. From Leonardo da Vinci's concept of a flying machine, to the Wright brothers first flight over 400 years later. From Jules Verne's 1865 novel (From the Earth to the Moon), to Wernher von Braun's development of the V2 rocket in WWII, and the space race of the 20th century. The progress of humanity has always been towards the stars and its future will continue to lie in the exploration of space, both for scientific knowledge and practical applications. The world will continue to expand its reliance on space transportation, for applications such as global communications, geomatics, navigation and weather forecasting. These applications benefit our society on a global scale and are the result of the ever-increasing number of artificial satellites.

The mainstay of space transportation and exploration has been liquid rocket engines, which are sometimes accompanied with solid rockets as boosters. Liquid rocket engines use fuel and an oxidizer, which is pressurized, and injected into the combustion chamber to provide thrust, see Fig. 1.1 [1].

After combustion, the gases flow through a converging-diverging nozzle before

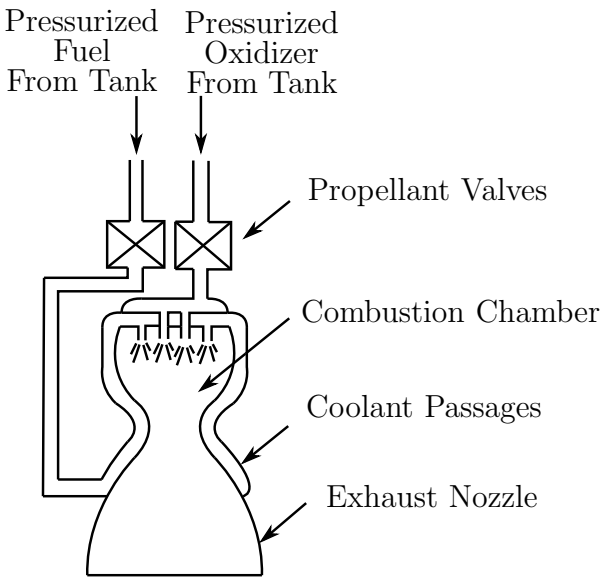

Figure 1.1: Simplified schematic of a rocket engine [1].

exiting the vehicle. The disadvantage of rocket engines is that they carry both their fuel and oxidizer onboard, which contributes to the vehicle weight. In contrast to this, airbreathing engines carry only fuel, as they utilize oxygen from the atmosphere. Airbreathing propulsion systems include conventional turbojet engines, ramjets and scramjets. Turbojet engines work by pulling air into a combustion chamber using a mechanical compressor at the inlet. In a ramjet, this compression is provided by the forward speed of the vehicle, and the engine inlet geometry. This, however, requires a minimum speed of $M_\infty \approx 2.5$, to achieve the required aerodynamic ram effect [2], but requires no mechanical compressor and its associated weight. After the inlet, the speed of the air is reduced to subsonic speeds ($M = 0.4 - 0.6$) and the pressure is increased by a diffuser [3], prior to combustion. Like rockets, converging-diverging nozzles are used in ramjet engines [4]. Ramjet engine afterburners are commonly combined with turbojet engines on fighter planes. The Pratt & Whitney J58 engines on the SR-71 BlackBird are an example of a turbojet/ramjet combination, which can cruise at Mach 3.2 [5]. Beyond $M_\infty \approx 5$, the deceleration of the air to subsonic speeds causes excessive stagnation/momentum losses due to the terminal shock, which affects

thrust performance [6]. For Mach numbers between $M_\infty \approx 5$ to $M_\infty \approx 15$ a scramjet (supersonic combustion ramjet) engine is required, where flow remains supersonic, as there is no diffuser [3]. This requires the flow path to be straight and/or diverging. A scramjet, therefore, burns fuel at supersonic speeds, as this becomes more efficient after $M_\infty \approx 5$. To prevent blow off at supersonic speeds, fuels such as hydrogen (H_2) or ethylene (C_2H_4) with high reaction rates are required [2]. An example of a scramjet powered aircraft is the NASA X-43A, which achieved a speed of Mach 9.6 [7].

Typically, oxygen fluxes for airbreathing vehicles are around 10 $(kg/s)/m^2$ [8] and are measured per air capture area. Since density decreases with increasing altitude, an airbreathing vehicle will need to fly faster as its altitude increases. Liquid rockets typically have 4 to 10 times as much oxygen flux, measured per vehicle cross sectional area [8]. This leads to different flight profiles as is illustrated in Fig. 1.2 [8].

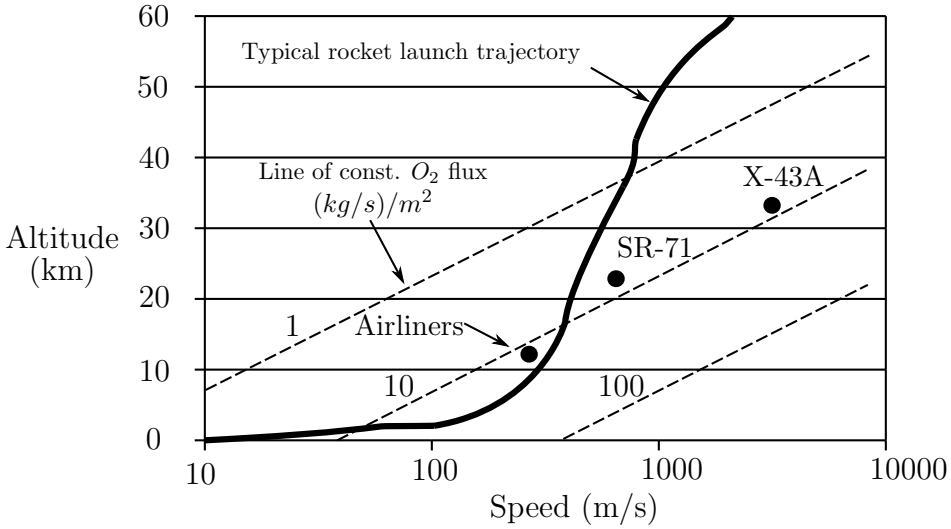

Figure 1.2: Flight profiles of airbreathing vs rocket engines [8].

Rocket vehicles take a much steeper trajectory to orbit to avoid atmospheric drag, due to dynamic pressure on the front of the vehicle. Airbreathing engines, however, remain in the atmosphere, to maintain the oxygen flux needed for thrust [8]. By using this atmospheric oxygen, airbreathing vehicles have lower vehicle propellent mass fractions compared to rocket engines. However, airbreathing vehicles are limited

to atmospheric operation.

1.1.1 Combined Cycle Engines

To reduce launch vehicle propellant mass fractions and costs, programs such as the NASA Advanced Space Transportation Program [9] have investigated alternatives to traditional rocket engines. One approach that has been examined is to combine rocket engines with other forms of airbreathing propulsion. This is referred to as a combined cycle engine. Since airbreathing engines do not carry their oxidizer, they offer high specific impulse (I_{sp}), but low thrust to weight. Rocket engines, on the other hand, offer high thrust to weight, but low specific impulse. The impulse provided by an engine is simply its average thrust, or force (F_{th}), multiplied by the total time it is applied to the vehicle (Δt). This is also referred to as total impulse (I) [10]. Specific impulse is the total impulse divided by the weight of the fuel mixture (i.e. propellants), see Eq.(1.1).

$$I_{sp} = \frac{I}{m_v g_0} = \frac{F_{th}\Delta t}{m_v g_0} = \frac{F_{th}}{\dot{m}_v g_0} \tag{1.1}$$

As Eq.(1.1) shows, the specific impulse is a measure of efficiency, in that it's the ratio of thrust force produced, per unit of propellant mass flow. The specific impulse for different airbreathing and rocket engines is shown in Fig. 1.3 [4].

As Fig. 1.3 indicates, turbojet engines provide superior specific impulse at speeds below Mach number $M_\infty \approx 3$. For increasing speed, the ramjet mode is superior between $M_\infty \approx 3$ to $M_\infty \approx 6$. After $M_\infty \approx 6$ the scramjet mode is the mode of choice, until the lack of oxygen at high altitudes requires rocket propulsion. The purpose of a combined cycle engine, therefore, is to combine one or more of these cycles together, to utilize the advantages of each mode over the entire flight range.

There are two main types of combined cycle engines, the turbine based combined

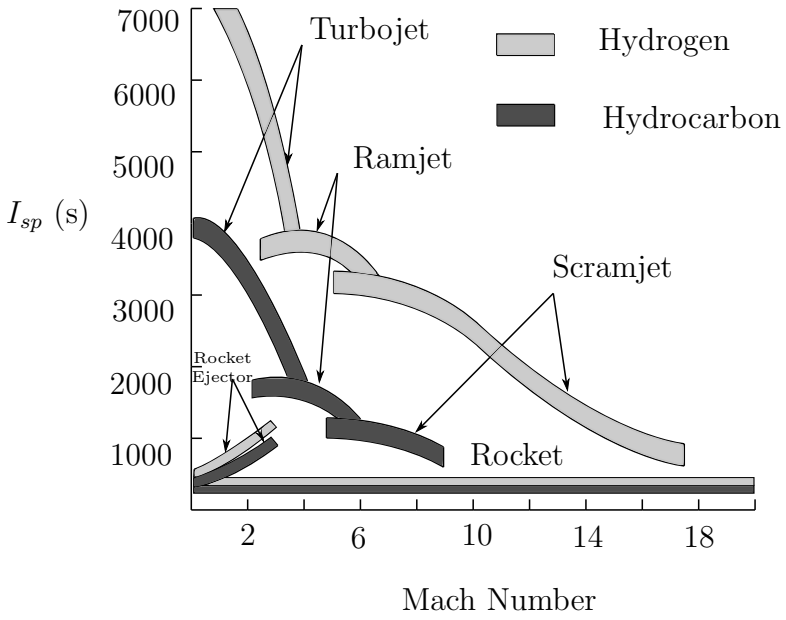

Figure 1.3: Specific impulse performance for various propulsion cycles [4].

cycle (TBCC) and the rocket based combined cycle (RBCC). For atmospheric flight, these two combined cycles differ mainly in their first stage [11], below the minimum ramjet speed. The TBCC engine uses a turbojet to accelerate up to $M_\infty \approx 3$, whereas the RBCC engine uses a rocket-ejector. An ejector is a device which uses a high velocity fluid to act as a pump, without the use of moving parts. A rocket-ejector, therefore, uses high velocity rocket exhaust to pump (or pull) air into the engine for downstream mixing and combustion. A simple example is shown in Fig. 1.4, in which a single rocket engine is surrounded by a duct.

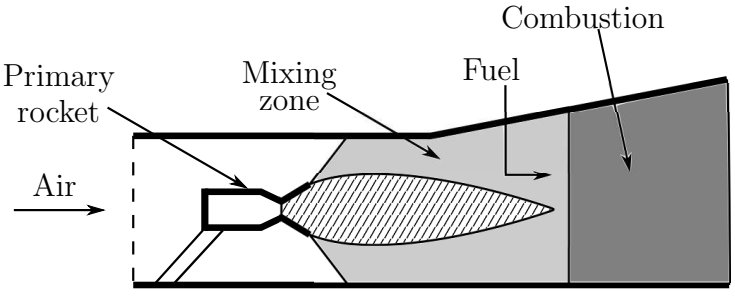

Figure 1.4: A simple rocket-ejector [4].

Therefore, a rocket-ejector in an RBCC engine and a turbojet in a TBCC engine serve the same purpose of accelerating the vehicle up to $M_\infty \approx 3$. After $M_\infty \approx 3$ a TBCC engine turbojet (or RBCC engine) transitions to ramjet mode. To avoid instability, the transition between these two modes has been investigated, by varying fuel flow and geometry [12].

The TBCC engine concept has also been studied at the NASA Glenn Research Center (GRC), where the air flow path was split into a low speed turbine section above and a high speed dual mode scramjet (DMSJ) section below [13]. This is referred to as an over/under configuration [13, 14]. Simulation at the GRC was completed using their High Mach Transient Engine Combined Cycle (HiTECC) software [15], with validation at the GRC's 10x10ft supersonic wind tunnel [13]. Since only airbreathing cycles are used, the TBCC engine is considered a two stage to orbit vehicle (TSTO) [6, 13], as it would require additional rocket propulsion for low earth orbit. Though the turbojet offers superior specific impulse below $M_\infty \approx 3$, it also adds extra weight and moving parts, which are unused during later flight modes. Other concepts such as the turbojet-rocket hybrid system $KLIN^{TM}$ have been explored as well [16].The focus of this work, however, is on the RBCC concept, which is described in the next section.

1.1.2 The RBCC Engine

The RBCC engine combines rocket-ejector, ramjet and scramjet modes for atmospheric flight, but can transition back to rocket propulsion for transatmospheric flight and low earth orbit. Therefore, the RBCC engine allows for a single stage to orbit vehicle (SSTO). An example of an RBCC powered vehicle is the NASA GTX airbreathing SSTO Vehicle Concept [17]. This vehicle consists of a main body with three RBCC engines, two of which are located on each side and the third on the top of the vehicle. The fuel (liquid H_2/O_2) is stored inside the main body of the vehicle,

which was designed for vertical launches and horizontal landings [17]. Black Brant solid rockets could also be added between the RBCC engines for additional thrust. A concept image of the vehicle is shown in Fig. 1.5.

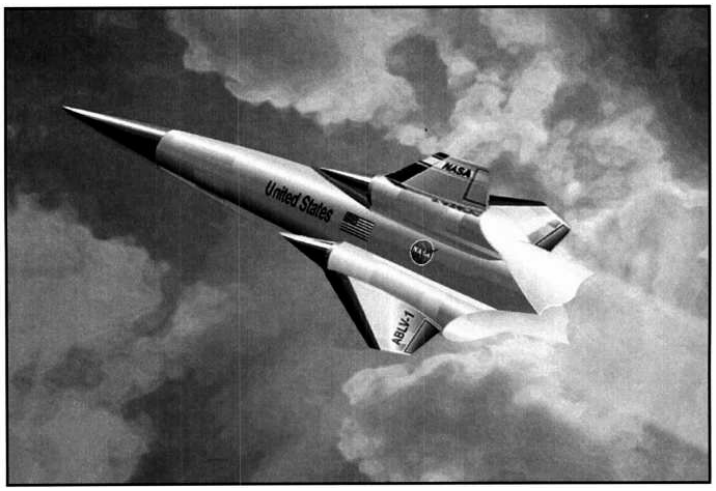

Figure 1.5: NASA GTX concept vehicle [17].

By utilizing atmospheric oxygen, the vehicle propellent mass fractions of RBCC powered vehicles can be reduced by up to 20% when compared to rocket engines. [18]. An RBCC engine consist of a primary rocket-ejector surrounded by a mixing duct, see Fig. 1.6, which can have a circular or annular exhaust flow.

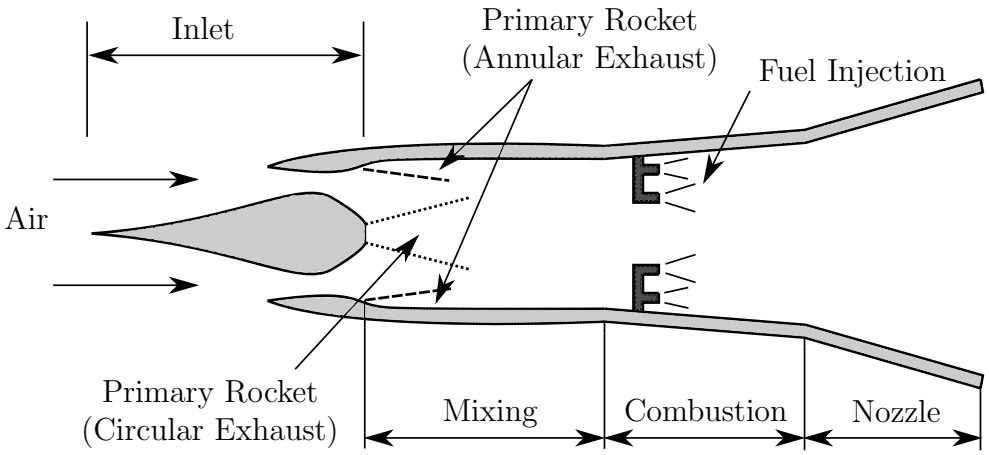

Figure 1.6: RBCC engine cross section [6].

The primary rocket-ejector effect is used in place of a turbine, where the high velocity primary rocket exhaust transfers its momentum to air at the inlet/mixing sections [19]. In addition, as momentum is transferred through the shear area the two streams are mixed. This serves to entrain air into the engine, and allow afterburning, for thrust augmentation via the ramjet/scramjet fuel injectors [20]. In ejector mode, the primary rocket still produces the majority of the thrust [21]. As the rocket-ejector accelerates the vehicle towards $M_\infty \approx 3$ the incoming air has a higher inlet velocity. Thus, the transfer of momentum is highest at static conditions and is reduced as the vehicle approaches the primary rocket exhaust velocity [22].

There are two common methods for thrust augmentation and afterburning, known as diffusion and afterburning (DAB) and simultaneous mixing and combustion (SMC) [23]. In DAB, the rocket exhaust is inert and serves only to transfer momentum, and provide mixing, as the fuel is added downstream by injectors. This allows high thermodynamic performance, at the expense of a relatively longer mixing duct [23]. The performance of DAB is higher than SMC at static sea level, but degrades as the vehicle Mach number increases [6]. In SMC, the primary rocket exhaust is fuel rich and the combustion happens simultaneously, as the two streams mix. The SMC scheme does not require a convergent-divergent nozzle, as opposed to DAB that does, which is advantageous for subsequent scramjet operation [23].

The shape of the primary rocket-ejector shear area profile affects both the mixing duct length and air mass flow into the engine [4, 6]. An increased mixing duct length is detrimental to vehicle performance, as it adds extra weight. Therefore, a high shear area between the rocket exhaust and entrained air is desirable, as it promotes increased mixing and reduces the L/D ratio of the duct [24]. A single circular rocket exhaust configuration requires L/D ratios of 8-10, whereas this ratio can be reduced to 2.5-1, by using either multiple circular exhaust bells or annular exhaust bells [24].

Additionally, it has been shown that a key aspect of RBCC engine performance is

the air mass flow at the inlet [25]. Therefore, increasing air entrainment by utilizing an annular rocket-ejector exhaust profile has been the focus of both numerical [26] and experimental [27, 28] studies. In both the simulation and experimental data, the results indicated that an annular, or semi-annular, exhaust provides superior air entrainment over a circular profile.

Once the rocket-ejector accelerates the vehicle to $M_\infty \approx 2.5 - 3$ the ramjet mode is implemented, followed by the scramjet mode. Investigations into the rocket-ejector to ramjet mode have shown that $M_\infty = 2.6$ provides an optimal transition point, when fuel throttling is employed [29]. The transition from ramjet to scramjet mode is also sensitive to the fuel injection scheme, which according to computational analysis, affects the development of a shock wave train inside the engine [30]. The air mass flow into the engine remains a key performance metric. In supersonic flight, shock waves are generated at the engine inlet due to its external geometry. These shockwaves affect both air mass flow and total pressure drop at the inlet. Stronger (bow) shock waves cause a larger total pressure drop across the shock, therefore reducing total pressure recovery of the inlet [31]. Since total pressure recovery is important to inlet performance [32], the design of the inlet external geometry is critical to overall RBCC engine performance. The focus of this work is on the optimization of an RBCC engine inlet performance over the supersonic flight regime. The RBCC inlet of interest is described in detail in the next section.

1.2 The Exchange Inlet

Since an RBCC engine inlet must operate over all flight modes, its design is of critical importance [33]. To utilize the advantages of a semi-annular rocket exhaust profile, for both improved mixing and air entrainment, previous research at Carleton University has resulted in the development of the exchange inlet [34, 35], see Fig. 1.7.

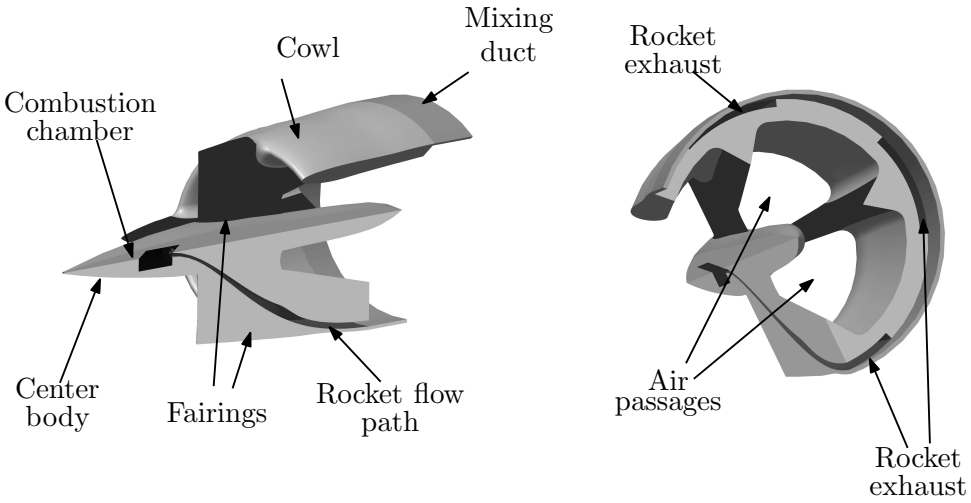

Figure 1.7: The exchange inlet cutaway views [36].

The inlet is composed of an internal rocket path [34] and an external geometry [35], consisting of a center body, fairings and cowl. The center body houses the combustion chamber, while the fairings contain an internal flow path for the primary rocket exhaust and provide structural support. The cowl surrounds the air flow path and provides the exit for the primary rocket exhaust.

The exchange inlet is designed to provide increased shear area compared to a circular primary rocket design, while maximizing entrained air through the air passages around the central axis. The momentum is transferred to the entrained air, around the annulus, to improve thrust and reduce the L/D ratio via improved mixing. The center body also provides a convenient attachment for existing rocket designs, while an axisymmetric profile allows for compatibility with existing nozzle designs. The leading point of the center body has a conical shape, while the fairings and cowl have rounded leading edges. In supersonic freestream conditions, these leading edges lead to the development of shock waves at the inlet. The conical center body causes the formation of a weak oblique shock wave, while the blunt leading edges of the fairings

and cowl cause strong (detached) bow shock waves [37, 38], see Fig. 1.8.

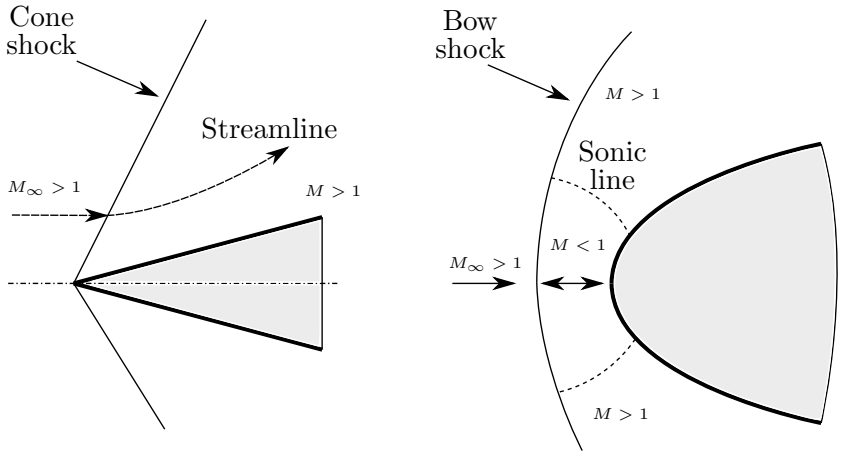

Figure 1.8: Cone shock vs bow shocks generated at leading edges [36, 38].

The oblique shock wave causes the flow direction to turn [39], but remain locally supersonic, after the shock [38]. The bow shocks have a region near the leading edge which is normal or near normal to the flow, and more oblique regions father away from the leading edge. This causes regions of both locally subsonic and supersonic flow after the shock depending on the location [38]. By changing the direction and speed of the incoming air, these shock waves not only affect the air mass flow into the engine, but also the total pressure drop across the inlet. These are the primary performance objectives of the exchange inlet.

1.3 Problem Statement

To facilitate the design and optimization process, both the internal and external geometry of the exchange inlet is determined by multiple input variables. Through the geometry creation, the selection of these variables then affects the performance objectives of the exchange inlet. Since the performance of the exchange inlet is determined

by more than one objective, the design problem becomes a multi-objective optimization problem. In addition, the objectives may also become competitive with each other. Therefore, the problem becomes one of determining the specific combination of input variables that results in maximizing each objective without compromising the others. The resulting combination solution will yield an optimized exchange inlet based on the user defined objectives.

This represents a non-linear multiple input, multiple output objective problem, where the dimensionality of the search space (domain) is determined by the number of input variables. Correspondingly, the dimensionality of the objective space (range) is determined by the number of objectives. The objective space is expected to have local optima, global optima and invalid solution regions. The optimality of an individual input combination is determined by its location in the objective space. The inability to predict the shape of the resulting objective space means that any optimization must be explorative enough to cover a wide range of the search space, while still being able to exploit regions of potential global optima. A random search function would be an inefficient way to find the global optimum due the large number of potential input combinations.

In engineering optimization problems it is expected that solutions do not need to be the exact optimum, especially if a near optimal solution will satisfy the requirements. In this way, solution time can be decreased at the expense of accuracy, provided the accuracy is adequate for engineering requirements. Evolutionary algorithms, such as differential evolution (DE), are well suited for this type of problem as their metaheuristic nature allows them to find near optimal solutions. The purpose of this thesis is to use differential evolution (DE) to solve the multiple objective exchange inlet optimization problem in the supersonic flight regime.

1.4 Overview of Evolutionary Algorithms

Evolutionary algorithms are heuristic (or metaheuristic) optimization methods, which means they are designed to find solutions that are near optimal, rather than an exact optimum. The algorithms achieve this by attempting to mimic nature, through representing solutions as individuals in a population. Using Darwin's theory of natural selection as an inspiration, the population is allowed to evolve to better suit its environment. As in nature, the evolution occurs by creating new generations through reproduction, where more fit individuals have a better chance of mating. The fitness of an individual, in nature, is determined by its environment. In evolutionary algorithms, the program iterates to create new generations in a similar manner, where the fitness of an individual is determined by the objectives. The objective space then becomes equivalent to the natural environment and a more optimal solution is a more fit individual. The fitness of an individual is determined by a fitness function, which determines an individual's fitness (in the objective space) based on single or multiple optimization objectives [40]. Over time this causes the algorithm to converge an initial set of solutions towards a near optimal solution, in the same way natural selection favours individuals who are more fit for their environment. In nature, an individual's characteristics are defined by its genes, which through its environment, determines its fitness. Similarly, in engineering and mathematics, solutions can be expressed as vectors, which through the objective space fitness function define their optimality. The comparison of evolutionary algorithms and natural selection is further illustrated in Table 1.1.

An evolutionary algorithm allows the population to evolve by applying the biological processes of selection, reproduction, and mutation. This allows new generations to be created and evaluated for their fitness. There are many subsets of evolutionary algorithms, however, genetic algorithms (GA) and differential evolution (DE) are two

Table 1.1: A comparison of EA with natural selection.

EA	Natural Selection
Set of solutions	Population
Potential solution vector	Individual
Program iteration	Generation
Optimality	Fitness
More optimal solution	More fit individual
Variables in a vector	Genes in a chromosome
Values of variables	Alleles of genes

of the most common represented in literature and engineering applications.

1.4.1 Genetic Algorithms

The development of the genetic algorithm (GA) began during the 1960's, and continued into the 1970's, by John Holland and his associates [41]. The GA uses Darwin's theory of natural selection as its model, where each iteration is considered analogous to a generation. As it explores the n-dimensional search space, the GA will evolve (converge) towards more fit individuals. The adaptive heuristic nature of these algorithms makes them well suited for real world engineering problems, that require the determination of optimal parameters [42]. An example of this, was the use of a GA for the subsonic optimization of the exchange inlet by Chorkawy [43]. Other examples of aerospace engineering GA applications range from wind tunnels [44], to injector systems [45, 46] and scramjet inlets [47].

For a GA to mimic nature, it follows the steps of genetic representation, selection, reproduction, and mutation. The alleles of a gene can be either binary numbers [48]

or real numbers [49], however, unlike nature only one chromosome represents an individual. The determination of the size of the chromosome and the number of genes is determined by the engineering problem in question. Once a given population is generated, then their fitness can be evaluated by the fitness function. The fitness function value is required for the process of selection. Like natural selection, a GA creates new individuals by mating two selected parents from the current generation, of the existing population. The process of selection can have both stochastic and deterministic properties. An example of a stochastic selection method is the Roulette wheel, where individuals with a higher fitness have a higher probability of being selected [40]. The selection method known as elitism is a deterministic selection method where the most fit individual is always selected for reproduction. Both methods were used by Chorkawy [43] in the previous subsonic optimization of the exchange inlet.

Reproduction takes place by the genetic operator known as crossover. This operator can switch out individual genes, sections of genes or arithmetically combine genes of the parents to create a child [49]. As in nature, mutation can occur on individual genes. In a GA, mutation is stochastically carried out on individual genes of the child, following reproduction. Crossover is an exploitative process, which promotes convergence by exploiting the genes of the parent individuals in the population. Depending on the selection process, these parents may have a higher probability of being selected for reproduction. Mutation, on the other hand, is an explorative process designed to help explore new regions of the search space [41]. Random mutation, therefore, attempts to prevent the solution from prematurely converging in a local optimum by promoting gene combinations that are outside of the current population. The process is repeated, with each generation, with the aim that the individuals will converge near a global optimal solution.

1.4.2 Differential Evolution

Building on the success of genetic algorithms in engineering optimization problems, R. Storn and K. Price [50] developed the metaheuristic search algorithm Differential evolution (DE). As a more recent development than genetic algorithms, it is considered a further evolution of them [41]. Like genetic algorithms, it has seen use in a wide range of engineering optimization problems ranging from chemical synthesis [51], to interplanetary trajectory design [52] and RBCC engines [53].

In their original 1996 paper, Storn and Price [50] laid out three requirements of any practical optimization technique. That (1) for any initial conditions it should converge to the true global optimum, (2) it should be fast and (3) that the number of input control parameters be minimized. The third condition is to ensure ease of use. To implement these requirements, differential evolution uses the operators of selection, reproduction and mutation in a different manner from both genetic algorithms and natural selection. Rather than mate two individuals in the population, a single individual is mated with a donor individual, which is a hybrid of three randomly selected members of the population. This represents a stochastic selection; however, DE implicitly maintains elitist selection in that the new child replaces the original parent in the population pool only if it is more fit. The donor is always discarded. By reproducing with a donor individual the operations of crossover (in reproduction) and mutation (through the randomly created donor) are combined into a single operation. By reducing the number of operations, the number of input parameters is reduced.

Differential evolution remains similar to genetic algorithms and natural selection in that it still uses the same operators, but differs in how they are implemented. In addition, as with GAs, a single chromosome (vector) represents an individual. However, DE only uses real numbers to represent the alleles of genes. The DE algorithm converges in the same way a GA does, as the generations evolve in the objective

space. Fitness is also determined by a fitness function, the same as in a GA. Both algorithms may suffer from premature convergence on a local optimum if their input control parameters are not set correctly. A performance comparison of GA and DE is discussed below, while the DE algorithm used in this work is discussed in more detail in Chapter 2.

Many studies have compared the results of the heuristic optimization techniques of genetic algorithms and differential evolution. A performance evaluation between differential evolution and a real number genetic algorithm, conducted by Tusar and Filipic [54], compared the results of 16 numerical tests. These experiments were done using multi-objective problems. The results of the experiments showed that DE significantly outperformed a standard GA 20% of the time. Only 3% of the time did the GA significantly outperform DE. In another comparison of differential evolution, real number genetic algorithms, and other optimization methods, Deb et al. [55] compared these techniques to optimize the design process of circularly polarized microstrip antennas. The results indicated that DE had statistically better results, in the optimization of microstrip antennas, over the other optimization methods, including real number GA.

Differential evolution and a real number genetic algorithm were also compared by Amorim et al. [56]. The comparison was performed using four case studies. The results showed that GA actually converged faster for the initial generations, but suffered in the later generations in refining the solution. The DE algorithm showed greater success in refining the solution to obtain higher fitness values. Given the performance and simplicity advantages of differential evolution over genetic algorithms, the DE algorithm will be examined for optimizing the exchange inlet problem.

Chapter 2

Methodology

2.1 Multi-Objective Optimization

In simple optimization problems, a solution can be found by minimizing or maximizing a single objective. In this scenario, the objective space is one dimensional, and the scalar objective solution is easily observed. Problems with more than one objective, such as the exchange inlet, are referred to as multi-objective optimization problems, and are described using Pareto optimality [40]. In this type of problem, the objective space becomes multi-dimensional and the objectives can be described using a vector [57]. There are two spaces to consider in this type of problem, the search space and the objective space. The transformation between these two multi-dimensional spaces is given by the system model, see Fig. 2.1.

The input vector ($\boldsymbol{x}$), and the variables in this vector, in Fig. 2.1, are the chromosome and genes described in Table 1.1. The number of genes (n), therefore, dictates the dimensionality of the search space, or the domain, while number of objectives (d) gives the dimensionality of the objective space, or the range. The location in the search space is given by $\boldsymbol{x}$, while the location in the objective space is given by the vector $\mathbf{H}$. Each space is bounded by a feasible region. In the search space, the bounds are given by the designer based on practical or engineering limitations. The

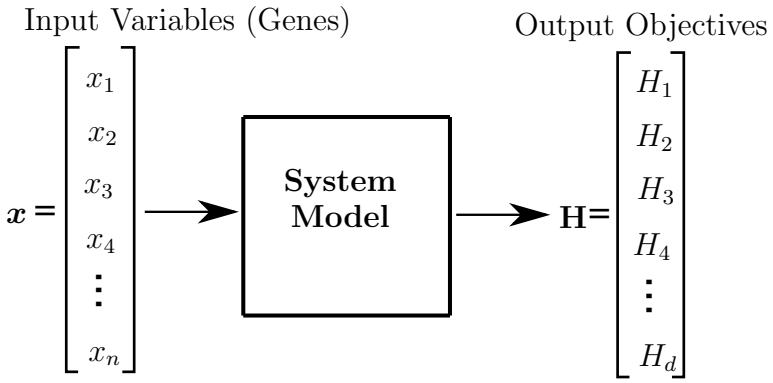

Figure 2.1: Overview of a multi-objective system.

feasible region of the objective space, however, is determined by the system model. In each space there are a set of values known as a Pareto optimal set. In the objective space, this set is often referred to as a Pareto front, since it exists at the boundary of the feasible region [58]. This Pareto front is a region which contains many possible optimal solutions. As the system model transfers the domain of the search space onto the range of the objective space, the Pareto front forms at this boundary. The location of the Pareto front, on this boundary, depends on whether the objectives are to be maximized or minimized.

The dimensionality of the Pareto front depends on the dimensionality of the objective space. In a two-dimensional space, it can be represented as a line, however in three dimensions it can become a surface. Higher dimensions, therefore, result in a front which is at least one dimension less than the objective space [59]. An example of a Pareto set and a Pareto front, where objectives are to be maximized, for two genes and two objectives is given in Fig. 2.2.

The Pareto front represents solutions, or in this case individuals, which are said to be non-dominated. Individuals behind this front are said to be dominated, in that they can be improved in one objective, while not negatively impacting another. In the example shown in Fig. 2.2, individuals which lie in the feasible region of the objective space can improve on H_1, while not impacting H_2 (or in a straight line). The Pareto

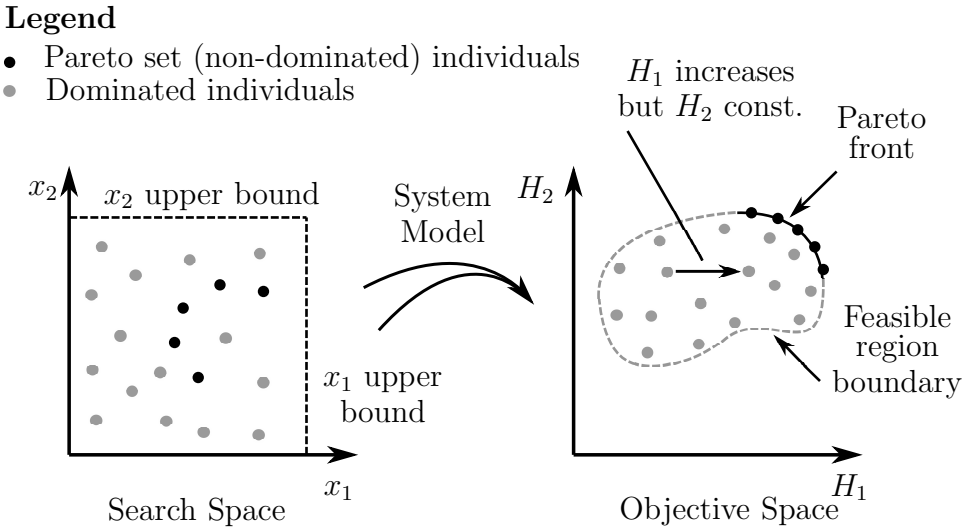

Figure 2.2: Pareto optimal set in search and objective spaces.

front, therefore, is said to be the region in which an individuals location cannot be moved to improve one objective, without negatively impacting another [40, 60].

In multi-objective problems, it is convenient to have a single value to determine the fitness of the resulting location in the objective space. Since the objectives can vary greatly in magnitudes, and represent different unit quantities, they are often normalized. In addition, the designer may also have different preferences for each objective. These preferences are determined by assigning weights to each objective. Consequently, the weighted sum method, see Eq.(2.1), is commonly used for multi-objective design problems.

$$f_i^k = \mathbf{W} \cdot \mathbf{H} = w_1 H_1 + w_2 H_2 + ... + w_d H_d \tag{2.1}$$

Equation (2.1), is referred to as an objective or fitness function, where all weights are positive and sum to 1. The weights can be written as a vector $\mathbf{W}$, see Eq.(2.2).

$$\mathbf{W} = \Big[w_1,\ w_2,\ w_3, ...,\ w_d \Big] \tag{2.2}$$

The fitness function in Eq.(2.1) is the dot product of the objective vector **H** and the weight vector **W**. The resulting most fit individual on the Pareto front depends on the weights assigned to the objectives. By varying the weights, the most fit location will move along the Pareto front [58]. In problems with more than two objectives, hyperplanes can be used to graphically demonstrate the Pareto front, as is the case for the exchange inlet. The fitness function is used to feedback information to the differential evolution algorithm for its selection process.

The objective space shown in Fig. 2.2 represents a simple feasible region, which has a concave Pareto front. In real engineering problems, the objective space may not always present such a simple shape. In addition, for problems with more than two objectives, the shape and location of the Pareto front region may be further complicated, when represented on a two-dimensional hyperplane. The Pareto front may have convex, irregular, or disconnected regions, due to the resulting shape of the feasible boundary in the objective space. Since gaps can appear between these disconnected regions, individuals with different weight settings, in the fitness function, may be forced onto the same Pareto optimal point [61, 62]. Subsequently, it is not possible to determine the shape of the feasible region or the Pareto front beforehand. Therefore, it is not possible to predict which set of weights might overlap on a point. This can be illustrated in Fig.2.3, as the most fit location on the front changes for different weight vectors.

The exchange inlet problem has more than two objectives. The air mass flow and total pressure drop represent the primary objectives, while the remaining secondary objectives relate to the rocket path and mixing. These are covered more extensively in section 2.2, along with the system model. By varying the weights of any two objectives, where the sum of the two weights remains constant, a Pareto front hyperplane can be developed. This not only allows insight for the designer, but also demonstrates the trade off between the two objectives. The shape of this front, however, is

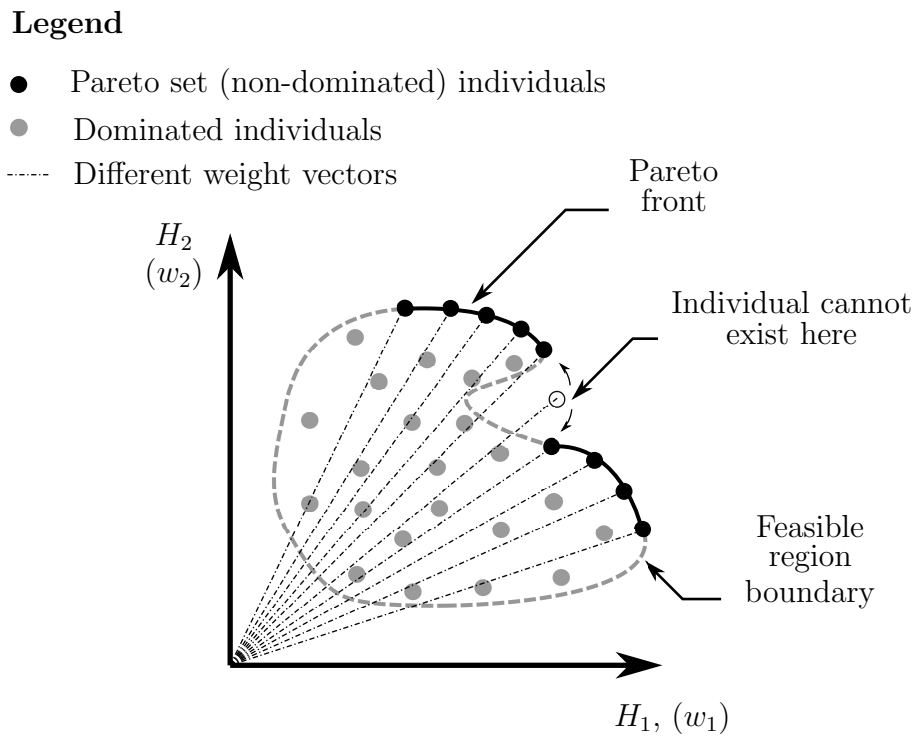

Figure 2.3: Disconnected Pareto front (adapted from [62]).

unpredictable and will depend on the system model.

2.2 The Differential Evolution Algorithm

Differential evolution represents the different geometrical solutions, of the exchange inlet, as individuals in a population. The DE algorithm, therefore, must be able to genetically represent the population, allow reproduction to create new individuals, and perform selection to determine which individuals end up in the next generation. Each individual contains a single chromosome with the genes that describe the geometry of the exchange inlet. Through selection and reproduction, these individuals evolve to better suit their environment, which is akin to their location in the objective space. Through evolution, the population then migrates towards the Pareto front. The population is mathematically represented by Eq.(2.3), where the index of an

individual is given by the subscript $i = 1, 2...m$, with m representing the population size. The generation is represented with the superscript k, with the initial ($k = 1$) generation having a random distribution.

$$\boldsymbol{X^k} = [\boldsymbol{x_1^k}\ \boldsymbol{x_2^k}...\boldsymbol{x_i^k}...\boldsymbol{x_m^k}] \tag{2.3}$$

Within the population, an individual can then be expressed, using the single chromosome, as shown in Eq.(2.4).

$$\boldsymbol{x_i^k} = [x_{i,1}^k\ x_{i,2}^k...x_{i,j}^k...x_{i,n}^k] \tag{2.4}$$

The index of a gene, within the chromosome, is given by the subscript $j = 1, 2, 3...n$. The value of n represents the number of genes, and therefore the dimensionality of the search space.

In order to evolve and create new individuals, the DE algorithm must generate new potential child candidates for the next generation. Therefore, for every individual $\boldsymbol{x_i^k}$, in the current population $\boldsymbol{X^k}$, a temporary donor (or mutant) individual $\boldsymbol{v_i^k}$ is created. The donor individual is created from three other randomly selected, and mutually exclusive, members of the population ($\boldsymbol{x_{r0}^k, x_{r1}^k, x_{r2}^k}$). This donor individual is temporary, as a new one is created for each individual of the population, from $i = 1$ to $i = m$. Therefore, for every generation, an m number of donor individuals must be created. Since the population size is fixed, these donor individuals exist outside the population. Their sole purpose is to be used for mating, and they are discarded afterwards. The donor individual $\boldsymbol{v_i^k}$ is created by first generating a difference vector ($\boldsymbol{\delta^*}$), from two of the randomly selected individuals ($\boldsymbol{x_{r1}^k - x_{r2}^k}$). Using a scaling factor, or differential weight (F), the difference vector $\boldsymbol{\delta^*}$ becomes a weighted difference vector ($\boldsymbol{\delta}$). This weighted difference vector is then added to the remaining randomly selected individual $\boldsymbol{x_{r0}^k}$. The creation of a donor individual is given by Eq.(2.5) [50, 63].

$$\boldsymbol{v_i^k} = \boldsymbol{x_{r0}^k} + F(\boldsymbol{x_{r1}^k} - \boldsymbol{x_{r2}^k}) = \boldsymbol{x_{r0}^k} + F\boldsymbol{\delta^*} = \boldsymbol{x_{r0}^k} + \boldsymbol{\delta} \tag{2.5}$$

The differential weight $F \in [0, 1]$ is set as a real positive number. Since the selection of the individuals $\boldsymbol{x_{r1}^k}$ and $\boldsymbol{x_{r2}^k}$ used to create the difference vector $\boldsymbol{\delta^*}$ is random, this allows the algorithm to explore regions beyond where the current population may lie. This occurs as $\boldsymbol{\delta}$ is added to the randomly selected (current member) of the population $\boldsymbol{x_{r0}^k}$. To illustrate this, consider the two-dimensional search space, and a one-dimensional objective space, shown in Fig. 2.4.

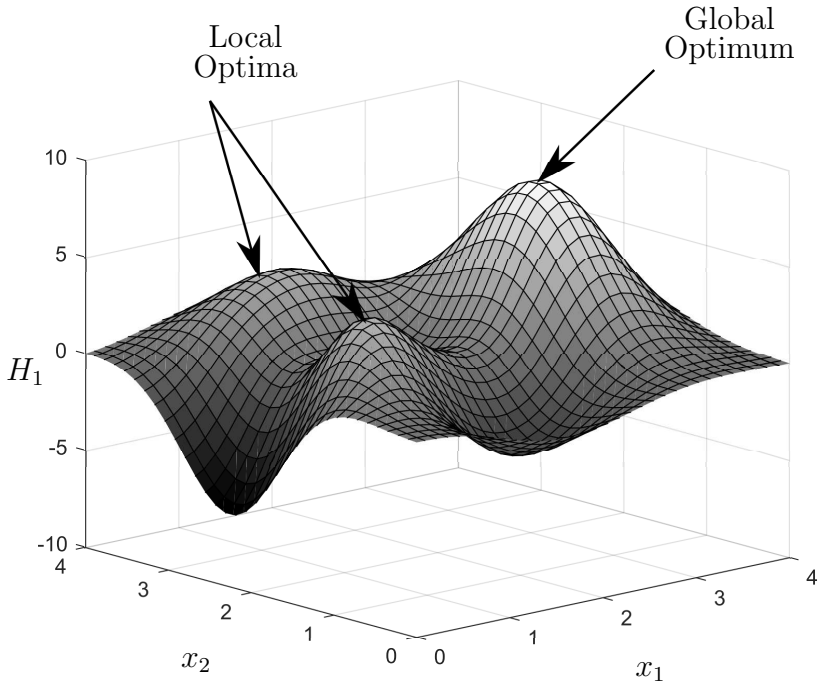

Figure 2.4: Objective function in two-dimensional search space.

As the figure shows, the higher regions are optimal locations, if the objective is to be maximized. The figure also contains both local and global optimal regions. By projecting the objective space contours, onto the search space, a 2D image of the process used to produce the donor individual $\boldsymbol{v_i^k}$, can be illustrated by Fig. 2.5.

For an initial ($k = 1$) randomly distributed population, there is a high probability

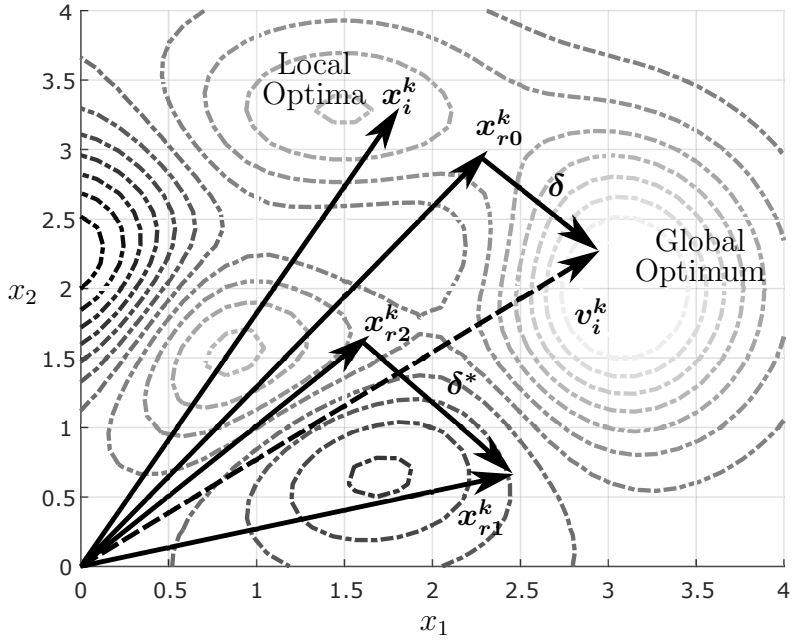

Figure 2.5: DE donor vector generation (adapted from [41]).

that the distances between the individuals ($\boldsymbol{x_{r1}^k}$ and $\boldsymbol{x_{r2}^k}$) in the search space will be relatively large. This means that initially the magnitudes of the difference vectors $\boldsymbol{\delta^*}$ will also be large, which helps explore competing optimal regions of the search space, and corresponding objective space. This occurs when $\boldsymbol{\delta}$ perturbs the donor individual $\boldsymbol{v_i^k}$ towards more optimal regions, as illustrated in Fig. 2.5. Consequently, the value of F also contributes to the distance of the exploratory perturbations. As the population evolves, and more individuals end up in the global optimal region, the distance between them decreases. This means that the distance of the $\boldsymbol{\delta}$ perturbations also decreases, so the exploratory behaviour becomes more confined to the most optimal region found. As a consequence of this, the exploratory nature becomes more exploitative, as it is exploits the region of the potential global optima.

For each index $i = 1, 2...m$, a new child candidate $\boldsymbol{u_i^{k+1}}$ is produced, through reproduction of the parent $\boldsymbol{x_i^k}$, with the newly created donor $\boldsymbol{v_i^k}$. As with other evolutionary algorithms, reproduction takes place by crossover of genes between the

parent $\boldsymbol{x_i^k}$ and the donor $\boldsymbol{v_i^k}$. In differential evolution there are two commonly used methods for implementing crossover, binomial (scattered) crossover and exponential (contiguous) crossover. The later, crosses over a random contiguous section of the genome, from the donor to the child. This method is less commonly used and, in general, it has been shown that binomial crossover can be slightly more efficient [64]. Since the nature of the of search and objective spaces are unknown, and adjacent genes are not necessarily correlated in terms of the objectives, the binomial scheme, see Fig. 2.6, is used in this work.

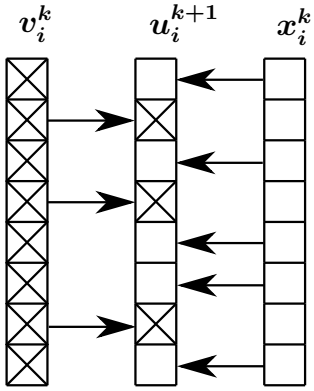

Figure 2.6: Binomial crossover in DE.

As Fig. 2.6 shows, the binomial scheme is where individual genes, from $j = 1, 2...n$, are crossed over from the parent $\boldsymbol{x_i^k}$ and the donor $\boldsymbol{v_i^k}$ to create the child $\boldsymbol{u_i^{k+1}}$. This occurs via the crossover probability C_r parameter and a randomly generated number R_i [65]. The creation of the child candidate is given by Eq.(2.6).

$$u_{i,j}^{k+1} = \begin{cases} v_{i,j}^k, & \text{if } R_i \in [0,1] \leq C_r \ \ or \ \ j = J_{rand} \\ x_{i,j}^k, & \text{otherwise.} \end{cases} \tag{2.6}$$

The child will inherit a gene from the donor $\boldsymbol{v_i^k}$ if the value of the random number R_i is less than or equal to C_r. Otherwise, it will inherit a gene from the parent $\boldsymbol{x_i^k}$. Therefore, if C_r is set to a low value, then the probability of inheriting a gene from

the donor becomes low, and vice versa. A low C_r value may result in the child not inheriting any genes from the donor, resulting in duplication of the parent $\boldsymbol{x_i^k}$. The result would be an inefficient algorithm, therefore, the term $j = J_{rand}$ is added to ensure that one gene is always inherited from the donor. The randomly selected gene index term J_{rand}, is different for each individual $i = 1, 2...m$.

Following reproduction, the new child candidate $\boldsymbol{u_i^{k+1}}$ for generation $(k + 1)$ is generated. The remaining process of selection is used to compare the fitness of this child candidate $\boldsymbol{u_i^{k+1}}$ with that of its parent $\boldsymbol{x_i^k}$. Since the population size remains constant, only one of these two individuals can survive into the next generation. If the child is more fit than its parent, then it replaces the parent individual in the next generation, otherwise it is discarded. Since the objectives are to be maximized, a more fit individual will have a higher fitness value. The selection process is given by Eq.(2.7), where the fitness value (f) is determined by the fitness function (f_i^k).

$$\boldsymbol{x_i^{k+1}} = \begin{cases} \boldsymbol{u_i^{k+1}}, & \text{if } f(\boldsymbol{u_i^{k+1}}) \geq f(\boldsymbol{x_i^k}) \\ \boldsymbol{x_i^k}, & \text{otherwise.} \end{cases} \tag{2.7}$$

This introduces the concept of selection pressure, since the parent individual $\boldsymbol{x_i^k}$ is only replaced if the child $\boldsymbol{u_i^{k+1}}$ is more fit. The selection pressure is what drives the evolution of the population, towards the most fit (global) location, in the Pareto front. This ensures that the next generation $(k+1)$ is more fit, or at least as fit, as the current generation (k). The selection pressure introduced by Eq.(2.7), is a deterministic process, which ensures only the most fit individuals will ultimately end up in the next generation. This implicitly integrates elitism into the DE algorithm [54], as only a more fit child individual $\boldsymbol{u_i^{k+1}}$ can replace its parent $\boldsymbol{x_i^k}$, for all $i = 1, 2...m$. The DE algorithm flowchart is illustrated in Fig. 2.7.

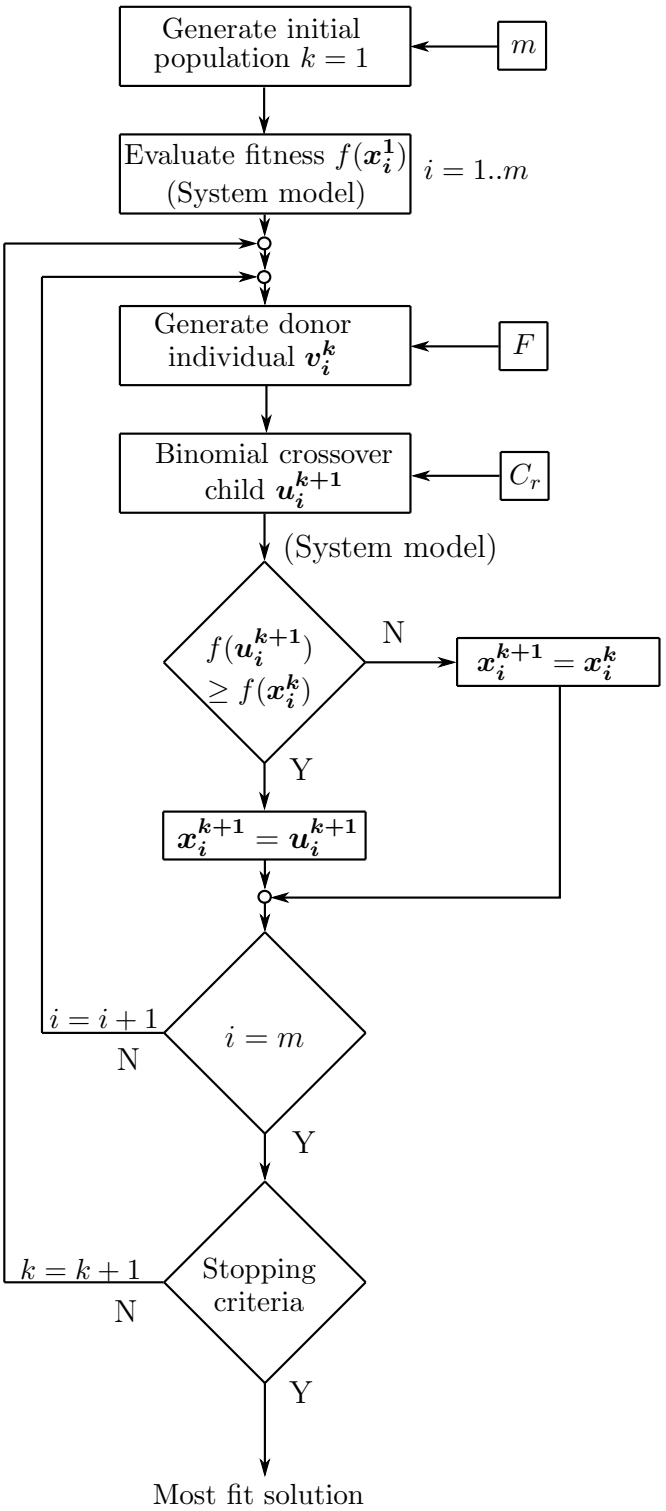

Figure 2.7: DE algorithm flowchart overview

2.2.1 DE Parameter Selection

As with any evolutionary algorithm, the efficiency of the DE algorithm will depend on the selection and tuning of its control parameters. It was noted in section 1.4.2, that the DE algorithm was developed with the intent to minimize the number of control parameters. The result is that using the binomial crossover scheme there are only three input parameters that control the algorithm. These are the population size (m), the differential weight (F) and the crossover probability (C_r).

The population size is critical in natural selection, as when this becomes too small genetic diversity is lost and more individuals become genetically identical. Similarly, this effect occurs in DE where population size can have a significant effect on the rate of convergence, or evolution, of the population. A small population size may result in the premature convergence of DE on a local optimum as the result of a rapid loss in population diversity [66]. In addition, fewer initial candidates means that less of the search space can be covered in any given generation. From Eq.(2.5), this loss of diversity means that its ability to perturb the donor, through $\boldsymbol{\delta}$, is lost if $\boldsymbol{x}_{\boldsymbol{r1}}^{\boldsymbol{k}}$ and $\boldsymbol{x}_{\boldsymbol{r2}}^{\boldsymbol{k}}$ become identical. Reproduction then becomes a crossover between $\boldsymbol{x}_{\boldsymbol{i}}^{\boldsymbol{k}}$ and $\boldsymbol{x}_{\boldsymbol{r0}}^{\boldsymbol{k}}$, which can cause the DE algorithm to stagnate, as more individuals share identical genes. Selection pressure will always cause a loss in diversity as it forces the population to evolve (converge) towards higher fitness values in more optimal locations. However, it is the effect of population size on the rate of this convergence, which must be considered. By contrast, using a large population size will prolong diversity, and slow the rate of this convergence, which allows the algorithm more time to explore the search space. Simply using a very large population, however, may result in a very slow algorithm, thus a method for selecting a proper population size range is needed. One approach that has been developed, is to select the range of the population size (m) based on the number of genes (n). In their papers, Ronkkonen et al. [67] and

Mallipeddi et al. [66] suggested a minimum population size of $2n$ and a maximum size of $40n$, as a common range. However, a smaller range of $2n$ to $10n$ was preferred by Mallipeddi et al. [66]. Additionally, in their original work, Storn and Price also preferred a similar range of $3n$ to $10n$. To examine the effect of population size, three values of $m = 25, 50,$ & 75 will be selected. This then corresponds to $3.125n, 6.25n$ and $9.375n$, for the exchange inlet problem, where there are $n = 8$ genes.

The second parameter is the differential weight F, which theoretically can be any positive real number. Values above 1, however, are rarely considered effective or reliable [67,68]. The common range is $F \in [0, 1]$, though the value of F=1 represents a discontinuity, where the number of potential donor individuals is reduced by half [63], see Eq.(2.8).

$$\boldsymbol{x}_{\boldsymbol{r0}}^{\boldsymbol{k}} + \boldsymbol{x}_{\boldsymbol{r1}}^{\boldsymbol{k}} - \boldsymbol{x}_{\boldsymbol{r2}}^{\boldsymbol{k}} = \begin{cases} \boldsymbol{x}_{\boldsymbol{r0}}^{\boldsymbol{k}} + (1)(\boldsymbol{x}_{\boldsymbol{r1}}^{\boldsymbol{k}} - \boldsymbol{x}_{\boldsymbol{r2}}^{\boldsymbol{k}}) \\ \boldsymbol{x}_{\boldsymbol{r1}}^{\boldsymbol{k}} + (1)(\boldsymbol{x}_{\boldsymbol{r0}}^{\boldsymbol{k}} - \boldsymbol{x}_{\boldsymbol{r2}}^{\boldsymbol{k}}) \end{cases} \tag{2.8}$$

The lower limit of F has been explored by Zaharie [69], based on maintaining the population diversity, as measured by its variance. As DE progresses, the population diversity (variance) is reduced by the selection pressure. If the objective space is flat, all locations have equal fitness, then the selection pressure does not exist. Zaharie demonstrates that, even in the absence of this selection pressure, a minimum theoretical value of $F_{crit} = 0.1341$ is required. Experiments [69], however, show having $F_{crit} = 0.3$ is more useful, since low values can lead to premature convergence [70]. The larger experimental value is the result of using more practical curved objective spaces. These curved objective spaces require a larger value of $F_{crit} = 0.3$, to counteract the selection pressure. The value of F affects the diversity, since it partially controls the magnitude of the perturbation $\boldsymbol{\delta}$. If the perturbation is initially too small,

then the ability to explore competing optimal regions can be compromised. Therefore, higher values are preferred. The generally useful range for F is $F \in [0.4, 0.95]$, with values around 0.9 demonstrating good results [67]. Therefore, the effects of $F = 0.85, 0.9, \& 0.95$ will be investigated.

The final parameter, crossover $C_r \in [0, 1]$, controls the probability that a gene from the donor $\boldsymbol{v_i^k}$ will be inherited by the child $\boldsymbol{u_i^{k+1}}$. This is an explorative process, where each gene represents an axis of the search space. A lower C_r value, then, means the algorithm explores along fewer axes of the search space at a time. If, for example, $C_r = 0$, then only a single axis, or dimension, of the search space is explored at a given time, due to $j = J_{rand}$. Conversely, high C_r values explore multiple axes at a time, which equates to multi-dimensional movements in the search space. From a performance standpoint, the shape and orientation of the objective space, relative to the search space, determines the selection of low vs high values for crossover [71]. Low C_r values are favored, when the objective space contours are oriented along the axes of the search space. If the objective space is oriented at angles to the axis of the search space, high values of C_r would be favored, as a single exploratory move occurs at angles to the axes of the search space [71, 72]. As the objective space orientation is not known in advance, both high and low values of C_r must be explored. Using $C_r = 0.5$ as an initial value [41], the crossover parameter test range will include $C_r = 0.3, 0.5, 0.7, \& \ 0.9$ values.

2.3 Application to the Exchange Inlet

The exchange inlet system model encompasses the creation of an internal rocket flow path, an external geometry, and the evaluation of the external supersonic flow into/around the resulting geometry. Each individual $\boldsymbol{x_i^k}$, contains $n = 8$ genes, which create both the internal and external geometries. The first 4 genes control the creation

of the internal rocket path, while the remaining 4 genes create the external geometry, around this internal path. The supersonic flow characteristics are determined from the external geometry using a semi-analytical shock fitting method [36]. The system model uses the genes of an individual to create a unique exchange inlet geometry, and from this provides the objectives, required by the fitness function.

2.3.1 Geometry Creation

The internal rocket path is a hollow path through which the rocket exhaust is expanded from a single central throat region into a semi-annular profile. The profile is designed to replace the diverging portion of a converging-diverging rocket nozzle. To allow air into the exchange inlet, the rocket flow path is divided into distinct clovers. The creation of these rocket path clovers is based around creating an inviscid rocket nozzle area (assuming isentropic expansion) from a predefined Mach number distribution, and then adjusts for boundary layer growth. The predefined Mach number distribution for this work is based on reproducing the performance characteristics of the liquid (O_2/H_2) fueled LE-7A rocket engine. The LE-7A engine is used as the first stage of the H-IIA launch vehicle, by the Japanese Aerospace Exploration Agency. It is also the profile from which Waung [35], based the exchange inlet external geometry creation on. From the LE-7A, the throat radius ($r_{th} = 0.121m$) is fixed [34, 35, 43] and to match its performance characteristics the exhaust plane depth is $z_e = 8.81m$. The exit radius ($r_e = 3.1m$) is also fixed, at 1m larger than a H-IIA launch vehicle exit radius [34, 43]. The exit Mach number of this rocket engine profile is $M = 3.95$. Its Mach distribution is illustrated in Fig. 2.8.

Since the viscous forces near the walls reduce the velocity, and therefore mass flow, this rocket nozzle area is then increased using a displacement thickness. This is done to ensure the predefined Mach number distribution [34]. The resulting area is made up of cross-sectional slices, beginning at the throat and ending at the exit.

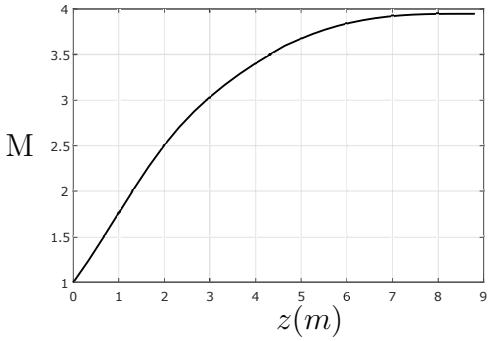

Figure 2.8: Rocket engine predefined Mach number distribution.

The cross-sectional areas for a single clover are shown in Fig. 2.9.

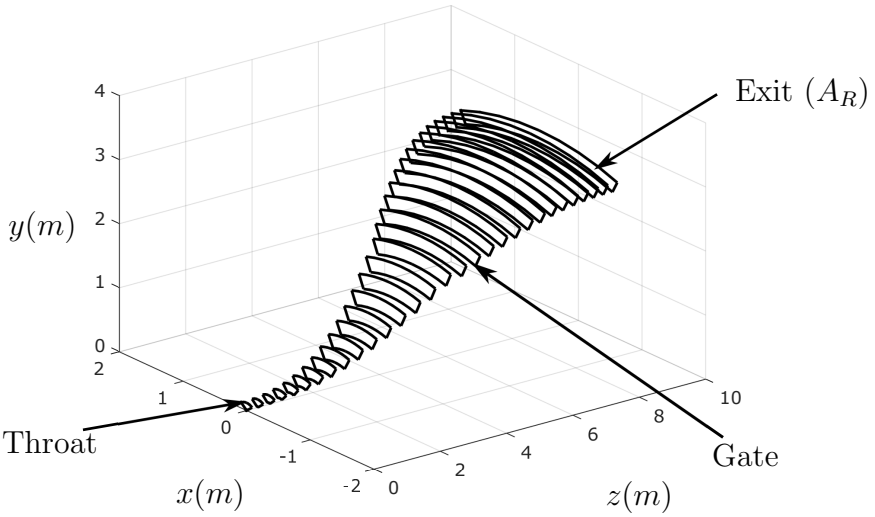

Figure 2.9: Cross-sectional area distribution for a single clover

The rocket path cross-sectional areas, illustrated in Fig. 2.9, show slices of a single clover, however, the internal rocket path, for this work, consists of four clovers. As the rocket exhaust expands through the predefined areas, it passes through a gate. The location and angle of this gate, are determined through the gate depth (z_g), the gate radius (r_g) and the gate arc angle (Ψ_g). The exhaust exit arc angle (Ψ_e), affects the shear layer area of the rocket exhaust at the exit. These four variables (Ψ_e, Ψ_g, z_g, r_g)

then are needed to define the different individual rocket paths, as shown in Fig. 2.10.

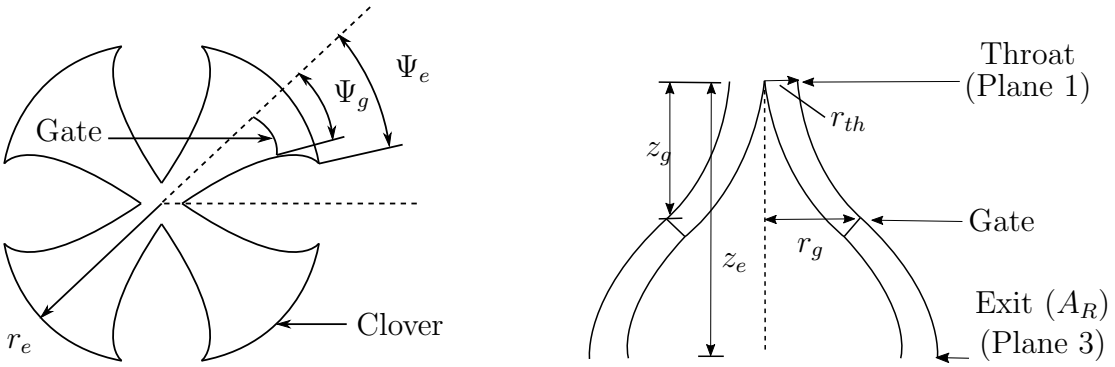

(a) Front View (b) Top view

Figure 2.10: Rocket internal flow path variables [43].

Around this internal rocket flow path is the external geometry of the exchange inlet. The external geometry has three main components: the center body, the fairings and the cowl. These are illustrated in the cutaway view in Fig. 2.11.

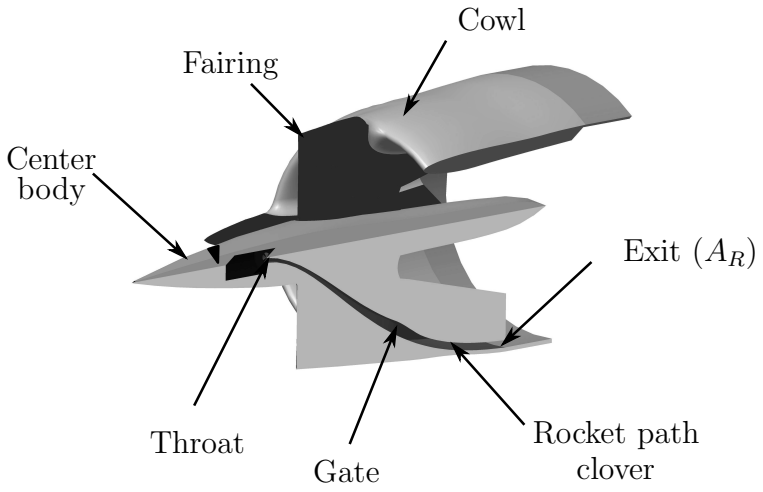

Figure 2.11: External geometry and internal rocket path of EI (adapted from [36]).

Each clover begins at the throat, located in the center body, and expands through

the fairings and exits inside the cowl. Therefore, there are four fairings, each containing a rocket clover. The 2D side profile of the exchange inlet external geometry and internal rocket path are illustrated in Fig. 2.12.

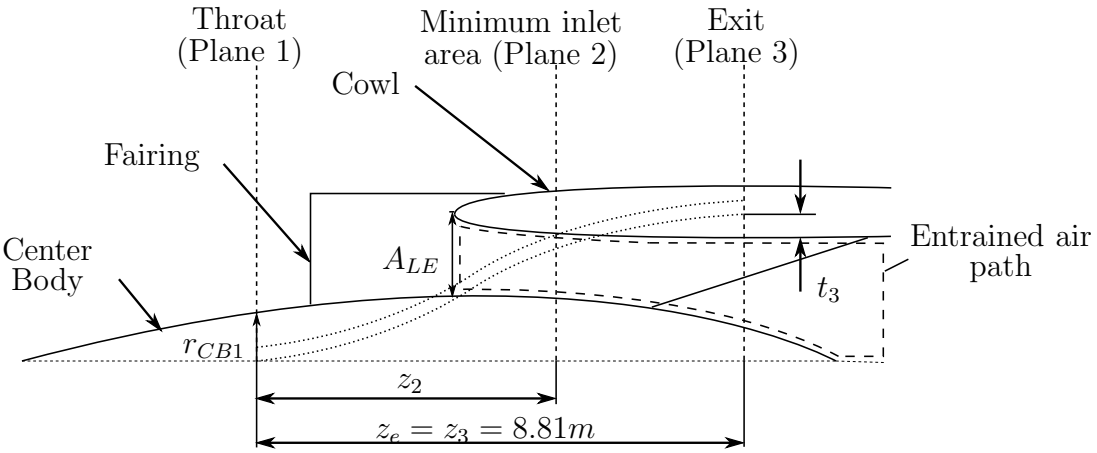

Figure 2.12: Exchange inlet external flow path variables.

The four input variables $(z_2, t_3, r_{CB1}, A_{LE})$ control the creation of the external geometry around the rocket path. The input variable (z_2) controls the location of the minimum inlet area (Plane 2), relative to the rocket exhaust exit (Plane 3). Plane 2 is also the location of the maximum fairing chord width, at its outer radial position. The remaining radial locations of the maximum fairing profile chord width follow the internal rocket clover path until intersection with the center body, see Fig. 2.13.

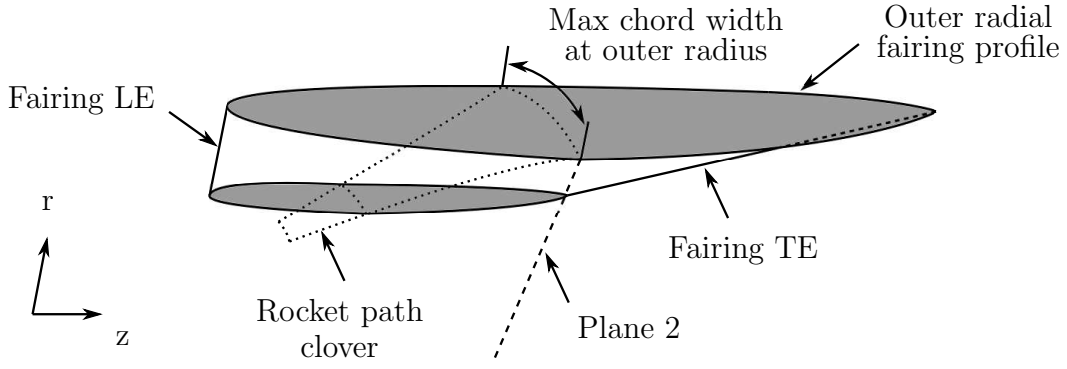

Figure 2.13: Fairing radial profiles [35].

The variable (t_3) is a material thickness constraint, which affects the cowl inner radius at the rocket exhaust exit (Plane 3). At the throat (Plane 1), the center body radius is controlled by (r_{CB1}). This variable also affects the overall center body curvature. The remaining variable is the area at the cowl leading edge (A_{LE}).

The 8 input variables, which determine the geometry, are controlled by the genes of an individual. The 8 genes ($\widetilde{\Psi}_e, \widetilde{\Psi}_g, \widetilde{z}_g, \widetilde{r}_g, \widetilde{z}_2, \widetilde{t}_3, \widetilde{r}_{CB1}, CR$) of the individuals $\boldsymbol{x}^{\boldsymbol{k}}_{\boldsymbol{i..m}}$, are normalized inputs of these 8 variables. The values of the genes are discretized over a predefined range. The genes, along with their bounds and resolutions, are listed in Table 2.1, and are defined to be compatible with the previous subsonic optimization [43].

Table 2.1: Rocket path and air geometry variables.

Gene	Controls variable	Normalized by	Min ($B_{j_{min}}$)	Max ($B_{j_{max}}$)	Resolution (res_j)
$\widetilde{\Psi}_e$	Ψ_e	45°	0.3	1	0.02
$\widetilde{\Psi}_g$	Ψ_g	45°	0.3	0.9	0.02
$\widetilde{z}_g$	z_g	z_e	0.2	0.9	0.05
$\widetilde{r}_g$	r_g	r_e	0.2	0.9	0.05
$\widetilde{z}_2$	$z_3 - z_2$	z_3	0.3	0.5	0.02
$\widetilde{t}_3$	t_3	$r_{NZ_{3in}}$	0.06	0.2	0.02
$\widetilde{r}_{CB1}$	r_{CB1}	r_{th}	2	8	0.5
CR	A_{LE}	A_2	1.06	1.4	0.02

The bounds of the genes, in Table 2.1, are set within the practical limits of the geometry creation process. For example, consider the gene $\widetilde{z}_2$. It controls the location of the minimum inlet area (Plane 2) as a fraction of the overall rocket path length ($z_e = z_3 = 8.81m$) via Eq.(2.9).

$$\widetilde{z}_2 = \frac{z_3 - z_2}{z_3} \tag{2.9}$$

If gene $\widetilde{z}_2$ is set too large, then it forces the minimum inlet area (Plane 2) further from the rocket exhaust exit (Plane 3), or towards the rocket path throat (Plane 1). However, as minimum inlet area is moved closer to the rocket path throat, the rocket path must remain contained within the external geometry. Thus, the radial location of the cowl leading edge decreases. This is due to the decreasing value of the rocket path radius towards the throat, and therefore, begins to affect the center body curvature as the minimum inlet area is maintained. This can result in a poor geometry, as shown in Fig. 2.14(b), if $\widetilde{z}_2$ continues to increase.

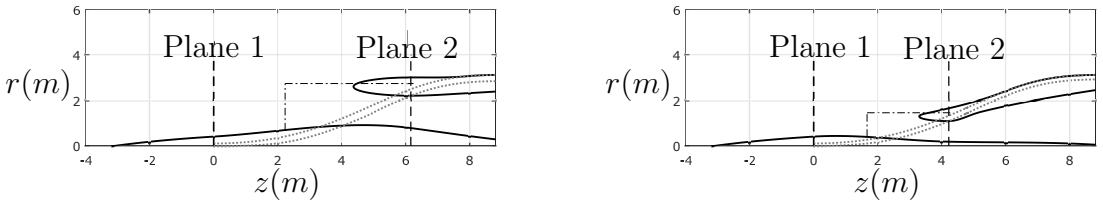

(a) $\widetilde{z}_2 = 0.3$ (b) $\widetilde{z}_2 = 0.52$

Figure 2.14: Effect of varying $\widetilde{z}_2$

Another example of the importance of the bounds can be seen with the gene $\widetilde{r}_{CB1}$, which controls the radius of the center body r_{CB1} at the rocket path throat (Plane 1), via Eq.(2.10).

$$\widetilde{r}_{CB1} = \frac{r_{CB1}}{r_{th}} \tag{2.10}$$

Since it is normalized by the throat radius, it is physically limited to a minimum value of 1. This gene, however, also effects the overall curvature of the center body. If the value is too small, or too large, it can cause regions of large convex and concave curvatures, which can result in flow separation, as shown in Fig.2.15.

A large value of $\widetilde{r}_{CB1}$ can also block the frontal area and lead to low air mass flow

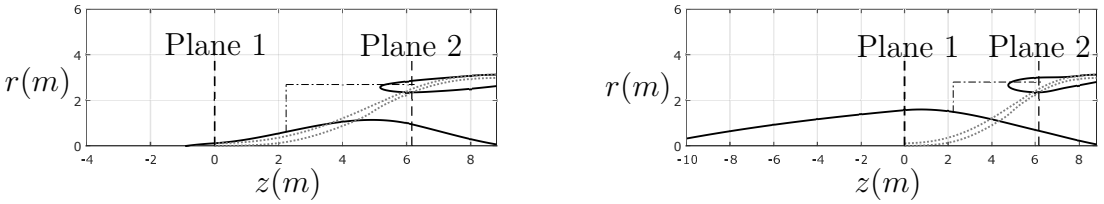

(a) $\widetilde{r}_{CB1} = 1$ (b) $\widetilde{r}_{CB1} = 13$

Figure 2.15: Effect of varying $\widetilde{r}_{CB1}$

into the inlet. Therefore, a range of 2-8, as shown in Table 2.1, is appropriate for this gene.

It is also important to consider a balance between the bound limits and resolution. If bound limits are too large, and the resolution is maintained, then the number of gene alleles increases. This can result in many unnecessary evaluations, as the number of potential combinations is increased. Thus, the bounds set in Table 2.1 are set to be within the realistic range of what the system model can create. The number of potential individuals, defined by Eq.(2.11), is a function of the number of genes (n), the bounds ($B_{j_{max}}, B_{j_{min}}$), and the resolution (res_j), as given by Eq.(2.12).

$$\boldsymbol{x_i^k} = [\, \widetilde{\Psi}_e,\ \widetilde{\Psi}_g,\ \widetilde{z}_g,\ \widetilde{r}_g,\ \widetilde{z}_2,\ \widetilde{t}_3,\ \widetilde{r}_{CB1},\ CR\,] \tag{2.11}$$

$$S = \prod_{j=1}^{n} \left(\frac{B_{j_{max}} - B_{j_{min}}}{res_j} + 1 \right) \tag{2.12}$$

For 8 genes, and the bounds/resolution given by Table 2.1, the number of possible individuals in the search space given by Eq.(2.12) is $S \approx 5 * 10^9$.

The rocket exhaust area (A_R) at the rocket exhaust exit (Plane 3), inside the cowl, and the rocket exhaust inner radius ($r_{NZ_{3in}}$), are controlled by the rocket variables (Ψ_e, Ψ_g, z_g, r_g). The minimum inlet area (A_2) and the exhaust plane inlet area (A_3), however, must also be evaluated in order to determine the curvature of the center

body, as shown in Fig. 2.16.

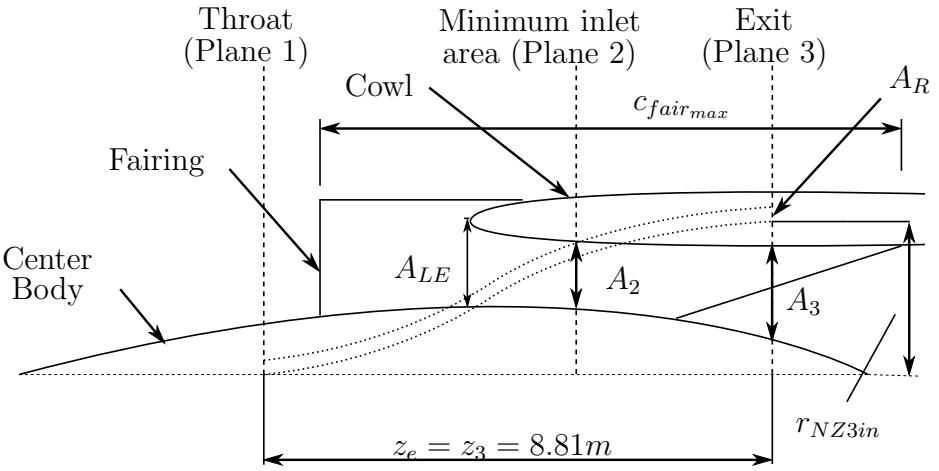

Figure 2.16: Exchange inlet external flow path additional values.

In addition, the fairing maximum chord length ($c_{fair_{max}}$) must also be evaluated to construct the external geometry of Fig. 2.16. This is achieved by three remaining values that are not genes, but must be defined. These values of $\widetilde{c}_{fair_{max}} = 1.115$, $\sigma = 0.1$ and $AR = 0.625$ are set using default values and are not directly controlled by the DE optimization. The fairing chord length ($c_{fair_{max}}$) is given by Eq.(2.13).

$$c_{fair_{max}} = z_3 * \widetilde{c}_{fair_{max}} \tag{2.13}$$

The value σ is the ratio of the rocket exhaust flow area A_R (refer to Fig. 2.9) to the total flow area ($A_R + A_3$), with 1 being a pure rocket and 0 being a pure airbreathing engine. This value is important for the rocket-ejector and is set according to the analysis provided by Waung [35]. The value AR is the ratio of the areas A_2 and A_3, where A_2 is the minimum exchange inlet area and A_3 gradually expands the flow into the engine. The areas A_3 and A_2, which in conjunction with $\widetilde{r}_{CB1}$, control the center body curvature, are determined using Eq.(2.14) and Eq.(2.15).

$$A_3 = A_R\left(\frac{1}{\sigma} - 1\right) \tag{2.14}$$

$$A_2 = A_3 * AR \tag{2.15}$$

The area A_2 and the gene CR define the area at the leading edge of the cowl A_{LE}, via Eq.(2.16).

$$A_{LE} = CR * A_2 \tag{2.16}$$

The center body radius is defined at the throat by r_{CB1} and the radii at Plane 2 & Plane 3, which are evaluated based on A_2 and A_3 and the inner cowl shape. The center body contour is defined by cubic Hermite curves and the radius ($r = 0$) boundary condition for the leading & trailing edges. The slope of the center body trailing edge is constrained at 1° to allow the flow to leave the center body surface as horizontal as possible [35].

2.3.2 The Objectives and Fitness Function

There are five objectives that are evaluated for a single exchange inlet system model. Three of the objectives relate to the rocket flow path performance, while the two remaining objectives are determined by the external geometry and semi-analytical shock fitting method [36].

2.3.2.1 Rocket Path Objective Space

The first rocket objective is to maximize the arc length of the rocket exhaust (L_{arc}). This objective is important as it affects the shear layer area between the primary rocket exhaust and the entrained air. The next objective is the turning angle (ϕ) of

the rocket exhaust path. This angle must not be excessively large as it can cause a sudden reduction in the rocket path cross sectional area thickness (Fig 2.9), due to sudden or excessive expansion in the circumferential direction. A sudden reduction in thickness can cause potential shock waves in the rocket exhaust. Since both objectives affect the inlet frontal area (A_{in}), see Fig. 2.17, they can become competitive with each other.

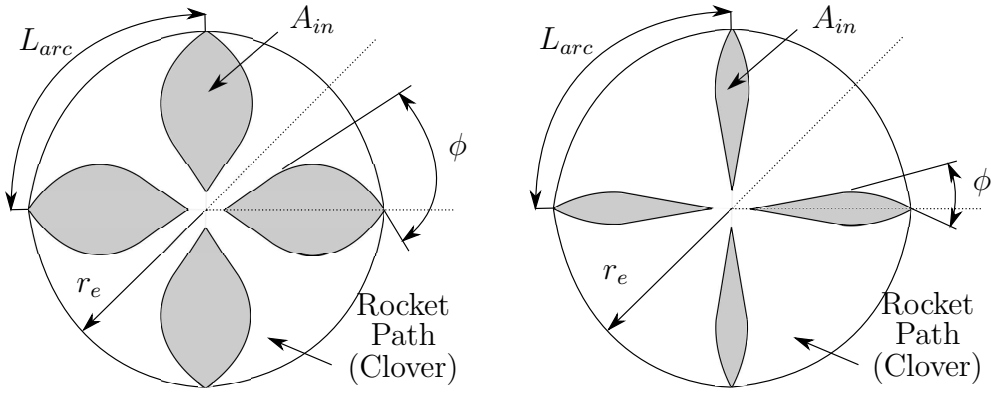

(a) A_{in} is increased at the expense of ϕ.

(b) ϕ is decreased at the expense of A_{in}.

Figure 2.17: Effect of competing objectives ϕ and L_{arc} on A_{in}.

The inlet frontal area A_{in} is the area between the rocket exhaust clovers. This area directly affects the area between the fairings, and therefore the air mass flow of the exchange inlet. The remaining rocket objective is the magnitude of the second derivative ($\frac{d^2\widetilde{r}}{d\widetilde{z}^2}$) of the radial contour. If the slope changes too rapidly, then shock waves can occur in the rocket path. To avoid any sudden changes in the curvature of this path, the rocket exhaust radial contour should be smooth. Examples of both a good and poor radial contours are illustrated in Fig. 2.18.

The plot in Fig. 2.18, shows the normalized radial contour of the rocket exhaust path. An ideal rocket path geometry should have a smooth curvature, and therefore a second derivative very close to zero. If there is a sudden change in the slope of the rocket path radial contour, this shows up as a spike in the magnitude of

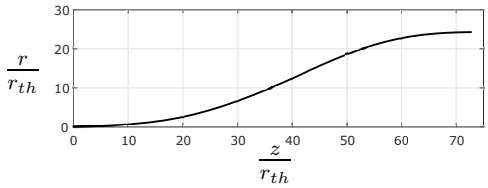

(a) Good radial contour

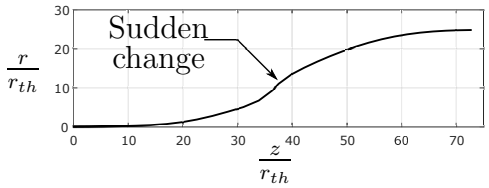

(b) Poor radial contour

Figure 2.18: Radial contour profiles for rocket flow path.

the second derivative. Examples of the corresponding good and poor radial contour second derivatives are illustrated in Fig. 2.19.

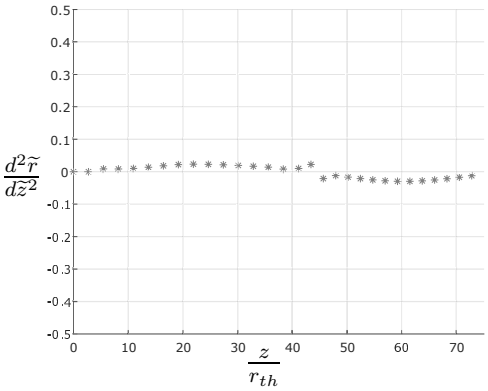

(a) Good second derivative profile

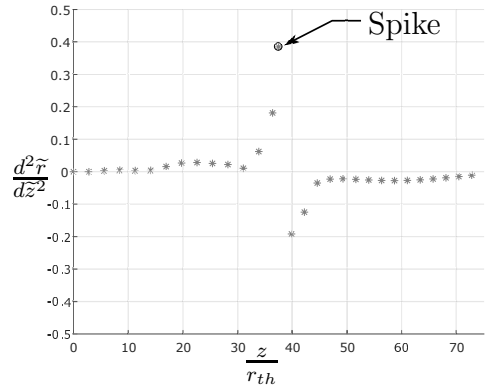

(b) Poor second derivative profile

Figure 2.19: Radial contour second derivative profiles for rocket flow path.

2.3.2.2 External Geometry Objective Space

The remaining two objectives are the air mass flow ($\dot{m}_a$) and the total pressure recovery of the inlet ($\overline{P_o}$). These are affected by the external geometry of the center body, the fairings and cowl, and the external shock waves that are created during supersonic flight. Each of these three components that make up the external geometry generate shock waves. These can be either weak oblique shocks, as in the case of the center body, or stronger bow shocks, as for the fairings and cowl. The three sets of external shock waves generated by the external geometry are illustrated in Fig. 2.20.

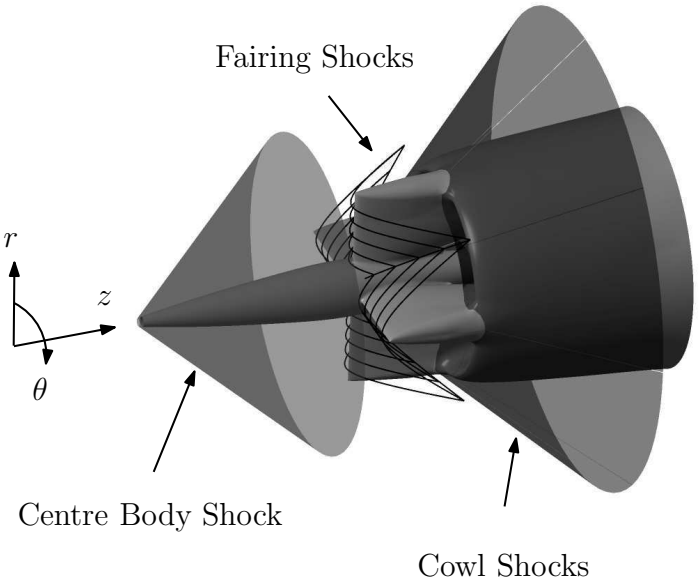

Figure 2.20: Main shocks generated by the geometry [36].

The total pressure recovery of the inlet $\overline{P_o}$, therefore, is the average total pressure behind the cowl shock.

These objectives are determined by the semi-analytical shock fitting method, developed by Murzionak [36]. This supersonic shock fitting method provides a quick estimation and is used instead of a CFD program as a 3D CFD simulation is too time consuming (there are 5 billion possible individuals that could be evaluated). This semi-analytical supersonic estimation method, however, was validated using a 3D CFD simulation, and was found to be within 10% of the CFD simulations, for both $\dot{m}_a$ ($1.1 \leq M_\infty \leq 7$) and $\overline{P_o}$ ($1.1 \leq M_\infty \leq 5$). The value of $\overline{P_o}$ showed a 30% error at $M_\infty = 7$. The % error between the estimation method and the CFD simulations for various Mach numbers is shown in Table 2.2.

The leading edge of the center body generates an oblique shock wave which is treated as a conical shock. The acceleration along the center body surface, behind the center body shock, is determined using a Prandtl-Meyer expansion function. Interpolation, between the center body and its resulting shock wave, is used to determine

Table 2.2: Estimation method % error vs CFD over supersonic regime [36].

Mach Number (M_∞)	1.1	1.3	1.5	2.0	2.5	3.0	4.0	5.0	7.0
$\dot{m}_a$ % error	3.7	6.2	3.3	3.5	-5.0	-3.7	-8.6	-5.1	4.6
$\overline{P_o}$ % error	-0.4	2.0	-1.5	-3.9	1.0	-1.4	-7.9	-1.0	-30.6

the Mach distribution in the radial direction, behind the center body shock [36]. This is illustrated in Fig. 2.21.

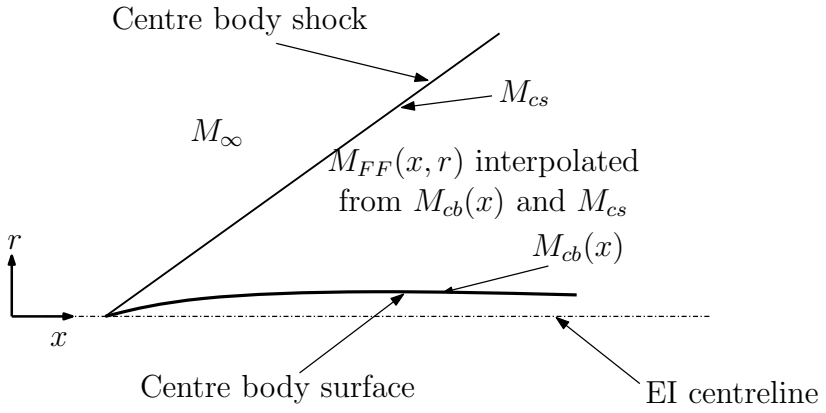

Figure 2.21: Schematic of cone shock generated by a centre body [36].

The flow field behind the center body shock becomes the input to the fairing shocks. The fairing shocks, and the cowl shock, are estimated by iteratively fitting the shock locations, assuming an infinite 2D blunt body solution. The properties behind the fairing shock become the inputs to the cowl shock estimation. The regions between the shocks are assumed to be isentropic, with no total pressure drop between them. The total pressure drop, across each shock, is determined by the normal component of the local Mach number, using the blunt body shock shape and the radial Mach number distribution. The total pressure drop is then the sum of all three drops through the center body, fairings and cowl shocks. The final value of total pressure behind the cowl shock is then averaged in the radial direction to get $\overline{P_o}$.

To evalute the $\dot{m}_a$ objective for the external geometry, it is assumed that there is

a dividing streamline, which separates the flow into two paths. One path enters the exchange inlet, while the other is diverted around the cowl. As shown in Fig. 2.22, this dividing streamline is perpendicular to the cowl surface at point ⓑ [36].

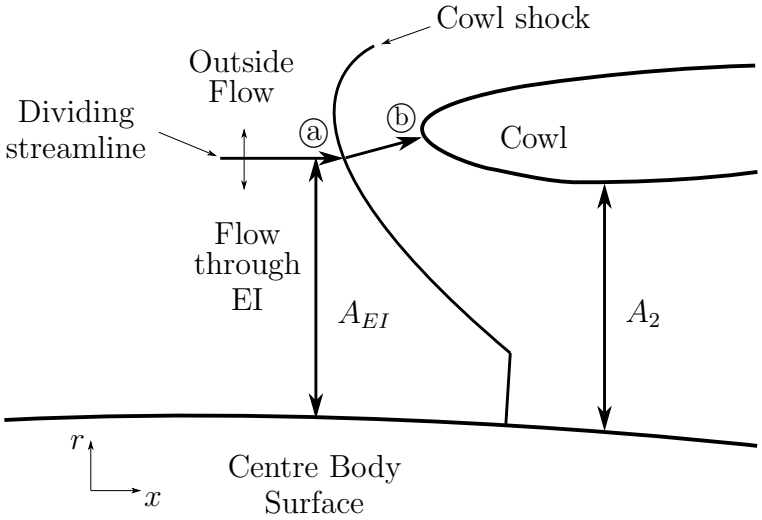

Figure 2.22: Determination of the air mass flow rate through EI [36].

The streamline from point ⓑ to point ⓐ allows the determination of the area A_{EI}, which represents the area through which the air stream enters the exchange inlet. By integrating along this line, the air mass flow into the inlet can be determined. The inlet geometry, however, may result in a condition where the flow is choked at A_2. Since the air mass flow into the inlet cannot exceed the choked flow, the minimum between the two air mass flow evaluations is used as the air mass flow objective.

2.3.2.3 Objective Vector and Fitness Function

Four of the objectives ($\dot{m}_a, \overline{P_o}, \phi, L_{arc}$), must be normalized to ensure that they are on a similar range (0-1) for the weighted sum method proposed by Eq.(2.1). The fifth objective $\frac{d^2\widetilde{r}}{d\widetilde{z}^2}$ is already normalized by the throat radius r_{th}. The normalized objective vector ($\mathbf{H}$), is given by Eq.(2.17).

$$\mathbf{H} = \left[\frac{\dot{m}_a}{\dot{m}_{max}},\ \frac{\overline{P_o}}{P_{o_\infty}},\ \left[1 - \left|\frac{\phi}{90^\circ}\right|\right],\ \frac{L_{arc}}{L_{max}},\ \left[1 - \left|\frac{d^2\widetilde{r}}{d\widetilde{z}^2}\right|^{0.5}\right] \right] \tag{2.17}$$

As shown in Eq.(2.17), the air mass flow objective is normalized by $\dot{m}_{max}$. This is a maximum theoretical value, set by the maximum area ($A_{max} = \pi r_e^2$) and freestream conditions, see Eq.(2.18).

$$\dot{m}_{max} = P_\infty \left(M_\infty \sqrt{\frac{\gamma}{R_{air} T_\infty}} \right) A_{max} \tag{2.18}$$

The total pressure recovery $\overline{P_o}$, is normalized by the freestream total pressure (P_{o_∞}), while the L_{arc} objective is normalized by the length of a fully annular profile ($L_{max} = 2\pi r_e$). The turning angle (ϕ) is desired to be minimized, therefore its 1 minus compliment is used in the objective vector $\mathbf{H}$. It is also normalized by 90°, as values beyond 90° are not realistic and would lead to reverse flow. Similar to the turning angle, a smaller peak value of the radial contour objective ($\frac{d^2\widetilde{r}}{d\widetilde{z}^2}$) is desired. Therefore, its 1 minus compliment is also used in the objective vector $\mathbf{H}$. Its exponent is used to improve the objective sensitivity for low values. Each of the objectives is weighted (weights are positive & sum to 1) using the weight vector in Eq.(2.19).

$$\mathbf{W} = \Big[K_a,\ K_b,\ K_c,\ K_d,\ K_e \Big] \tag{2.19}$$

As the fitness function is the dot product of the objective vector $\mathbf{H}$ with the weight vector $\mathbf{W}$ (see Eq.(2.1)), the fitness function for the exchange inlet is given by Eq.(2.20).

$$f_i^k = K_a \frac{\dot{m}_a}{\dot{m}_{max}} + K_b \frac{\overline{P_o}}{P_{o_\infty}} + K_c \Big[1 - \Big|\frac{\phi}{90^\circ}\Big|\Big] + K_d \frac{L_{arc}}{L_{max}} + K_e \Big[1 - \Big|\frac{d^2\widetilde{r}}{d\widetilde{z}^2}\Big|^{0.5}\Big] \tag{2.20}$$

Chapter 3

Expected Behaviour and Algorithm Tuning

3.1 Overview

The behaviour and performance of the DE algorithm is important to understand, especially its ability to avoid becoming trapped in a local optimum. This is a problem that all evolutionary algorithms can face when not tuned correctly. Therefore, it is important to establish some measure of probability of being near the global optimum. In any objective space landscape, there exists a potential for one or more local optima, which have peaks that are very close in height to the global optimum, regardless of their proximity to it. In this case, it would appear that all runs have found a single optimal region, if only the fitness values are observed. However, since these peaks may be very far apart, they could represent very different individuals, and thus geometries. To indicate the proximity of the individual solution to the global optimum then, the deviation in the genome from the global optimum, or best individual, is observed. The more the magnitudes of the genes differ from this best individual, the farther the evaluated individual exists from the global optimum. This provides an indication of whether or not the result of any run has converged on the global optimum region, or

if it has become stuck in a distant local optimum that has a close fitness (peak) value. To test this concept, it is first implemented on the rocket path in isolation (4 genes), then adapted to the exchange inlet as a whole (8 genes), to estimate its probability of converging in the global optimum region. All runs are done using MATLAB® on a Linux based computer cluster, provided by Carleton University.

3.2 Rocket Path Testing Results

The individuals $\boldsymbol{x_i^k}$ in the rocket path testing are given by Eq.(3.1), which is a simplified version of Eq.(2.11), as they have only 4 genes.

$$\boldsymbol{x_i^k} = [\ \widetilde{\Psi}_e,\ \widetilde{\Psi}_g,\ \widetilde{z}_g,\ \widetilde{r}_g\ ] \tag{3.1}$$

In this case, the system model consists only of the rocket geometry creation. The rocket path also does not provide direct information about the air mass flow $\dot{m}_a$ and total pressure recovery $\overline{P_o}$ objectives. However, the frontal area A_{in}, can be used in place of these objectives, to give a simplified fitness function provided by Eq.(3.2).

$$f_i^k = K_a\frac{A_{in}}{A_{max}} + K_b\Big[1 - \Big|\frac{\phi}{90^\circ}\Big|\Big] + K_c\frac{L_{arc}}{L_{max}} + K_d\Big[1 - \Big|\frac{d^2\widetilde{r}}{d\widetilde{z}^2}\Big|^{0.5}\Big] \tag{3.2}$$

The progress of the DE algorithm can be assessed by monitoring the fitness of the most fit (or best) individual for each generation (k), see Eq.(3.3).

$$f_{best}^k = max(f_i^k) \tag{3.3}$$

Since each initial population is randomly generated each run provides a unique path of the most fit (f_{best}^k) individual in the population. For the algorithm to be successful, it must be able to evolve, or converge, towards the global optimum, regardless of the initial locations of the randomly distributed individuals at $k = 1$. As the total

number of evaluations (Γ) is a function of both the number of generations k and the population size m, it is the metric over which the fitness, and other properties, can be monitored. This is given by Eq.(3.4).

$$\Gamma = k * m \tag{3.4}$$

To demonstrate the convergence of the most fit f^k_{best} individual, for different initial populations, its fitness value is monitored over the total number of evaluations Γ. The DE parameter of population size is set to $m = 38$, which equates to $9.5n$. The remaining parameters are set to default values of $F = 0.9$ and $C_r = 0.5$. The fitness of the most fit individual is illustrated, for four separate runs, in Fig. 3.1, where all weights (K_a, K_b, K_c, & K_d) were equal at 0.25.

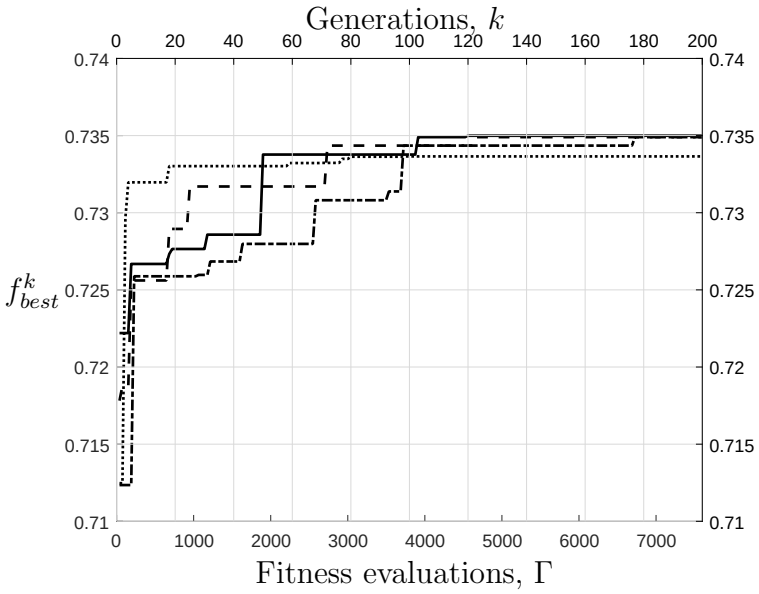

Figure 3.1: Fitness of most fit individual vs total evaluations for rocket path (m=38, F=0.9, C_r=0.5).

As seen in Fig. 3.1, all 4 runs have a unique path of f^k_{best} as they converge. Three of the four runs illustrated converge to a similar fitness value, while a 4th appears to prematurely converge to a lower value. This could indicate that this run has been

trapped in a local optimum. Not all combinations of genes in the search space result in valid individuals. In this case they have a fitness of zero, until they produce a child with a higher fitness. Consequently, the initial population will have only a small percentage of individuals with non-zero fitness. This will increase overtime, as all the individuals are allowed to mate, and will eventually be replaced with more fit children. The number of non-zero (NNZ) fitness individuals is shown in Fig. 3.2, for the same 4 runs as Fig. 3.1.

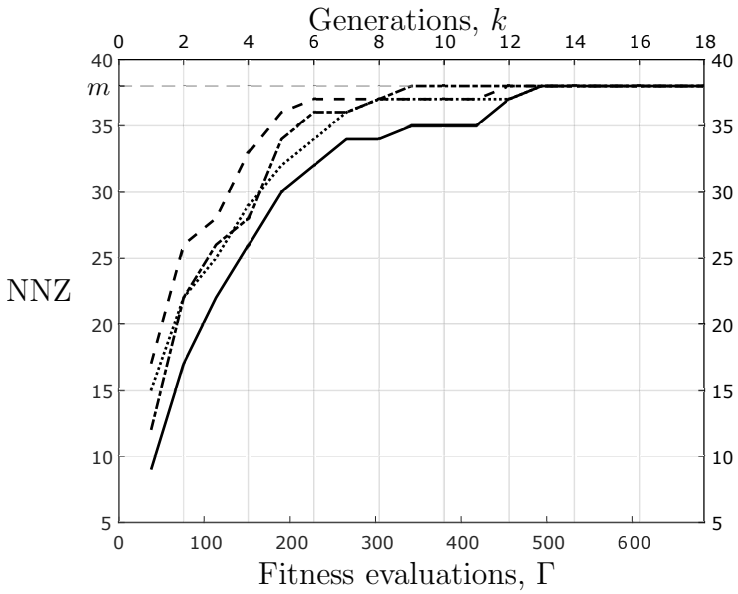

Figure 3.2: Number of non-zero fitness values vs total evaluations for rocket path (m=38, F=0.9, C_r=0.5).

Figure 3.2 shows all runs with a low number of non-zero fitness initially. However, after about 13 generations ($\sim$ 500 evaluations) all runs reach a maximum of number of 38 non-zero individuals, which is the population size m.

With many of the initial population individuals having zero fitness, the variance in the population fitness values ($Var(f_i^k)$), will typically initially be low. This will increase rapidly, as more fit and unique individuals are found. The selection pressure, however, will eventually begin to reduce the variance as it directs more individuals

towards optimal locations. This is illustrated in Fig. 3.3, using the same 4 runs as Fig. 3.1.

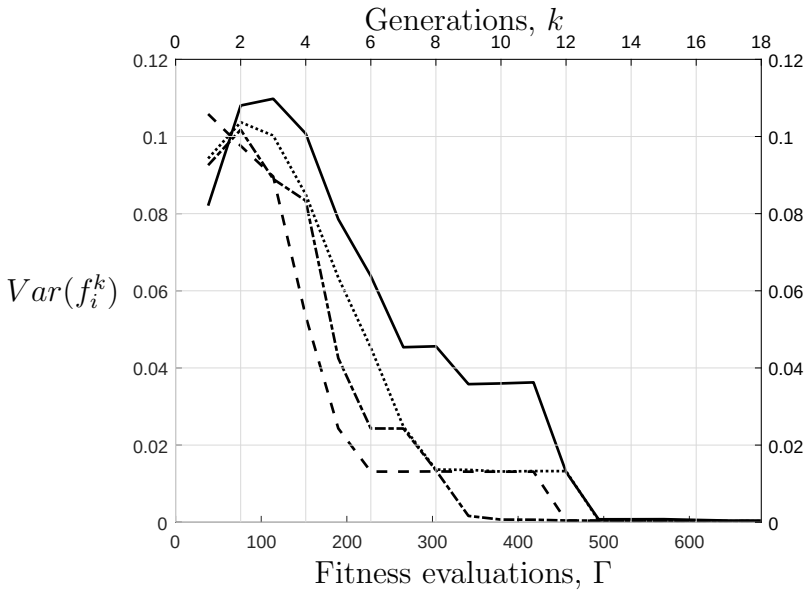

Figure 3.3: Variance of population fitness values vs total evaluations for rocket path (m=38, F=0.9, C_r=0.5).

The variance in the fitness values is given by Eq.(3.5), where $\overline{f_i^k}$ is the mean of f_i^k.

$$Var(f_i^k) = \frac{1}{m-1}\sum_{i=1}^{m} |f_i^k - \overline{f_i^k}|^2 \tag{3.5}$$

The rocket path also provides a good testing ground for the DE algorithms ability to find the global optimum, as it has only 4 genes. This yields a much smaller 4-dimensional search space ($S \approx 2.5 * 10^5$ possible combinations) than the entire exchange inlet. This is four orders of magnitude less than the exchange inlet, with its 8 genes and $S \approx 5 * 10^9$ possible combinations. In addition, a single evaluation of Eq.(3.2) only requires approximately 1.5-2 seconds, whereas for the exchange inlet Eq.(2.20) requires 10-15 seconds. The small size of the rocket path search space, and its faster evaluation time, allows all of its known possibilities to be calculated in

advance. By knowing the location of the true global optimum, or best individual, the probability of the algorithm finding a near optimum solution can be estimated.

The criteria for a near optimal solution is given by its average (%) deviation in its genome from the true global optimum, in addition to its fitness value. This is easily accomplished when the true optimal is known, as is the case for the rocket path. For a given gene $j = 1...n$ of an individual $\boldsymbol{x_i^k}$, its average deviation (Dev_i) is determined by the difference in the number of resolution points (N_{i,res_j}, Eq.(3.6)) from the optimum (best) individual ($\boldsymbol{x_{BEST}}$), divided by the total number of resolution points of that gene ($S_{i,j}$, Eq.(3.7)), summed across all the genes (n) in an individual, see Eq.(3.8).

$$N_{i,res_j} = \frac{|x_{BEST,j} - x_{i,j}^k|}{res_j} \tag{3.6}$$

$$S_{i,j} = \left(\frac{B_{i,j_{max}} - B_{i,j_{min}}}{res_j} + 1 \right) \tag{3.7}$$

$$Dev_i = \frac{1}{n} \sum_{j=1}^{n} \frac{N_{i,res_j}}{S_{i,j}} * 100\% \tag{3.8}$$

The top 4 individuals found using DE for 10 runs of the rocket flow path, using the same parameters as those used to generate Fig. 3.1 to Fig. 3.3, are listed in Table 3.1, along with the best individual. This best individual $\boldsymbol{x_{BEST}}$ was found by evaluating all possible ($S \approx 2.5 * 10^5$) individuals in the rocket path search space.

As Table 3.1 shows, the final (Rank 4) individual has as very similar fitness value to the best $\boldsymbol{x_{BEST}}$ individual, within 0.3%. However, its genome differs from $\boldsymbol{x_{BEST}}$ by 55%. This indicates that although the fitness value peak is very close in magnitude, this individual is actually a distant local optimum, with a very different geometry. The difference in the two rocket path geometries is illustrated in Fig. 3.4.

As shown in Fig. 3.4, the two geometries differ mainly in their frontal area A_{in}

Table 3.1: Top 4 fit individuals found vs the best individual.

Rank	Fitness	$\widetilde{\Psi}_e$	$\widetilde{\Psi}_g$	$\widetilde{z}_g$	$\widetilde{r}_g$	Dev_i (%)
$\boldsymbol{x_{BEST}}$	0.7358	0.32	0.32	0.3	0.6	-
1	0.7350	0.32	0.32	0.3	0.5	3.3
2	0.7349	0.32	0.32	0.25	0.4	8.3
3	0.7343	0.36	0.36	0.2	0.35	14.7
4	0.7337	0.64	0.58	0.9	0.2	54.9

(a) Global (best) optimum (b) Local optimum (Rank 4) individual

Figure 3.4: Global (best) rocket path vs distant local optimum.

and arc length L_{arc} objectives. The two have similar fitness values as improving on one objective compromised another. The distant optimum can also be seen by looking at the objective space landscape. This is illustrated in Fig. 3.5 for $\widetilde{\Psi}_e$ and $\widetilde{\Psi}_g$ respectively.

As shown in Fig. 3.5, the $\boldsymbol{x_{BEST}}$ and the first 3 individuals from Table 3.1 are clustered at low values of $\widetilde{\Psi}_e$. The remaining 4th individual is located at the local optimum, with a $\widetilde{\Psi}_e = 0.64$ and $\widetilde{\Psi}_g = 0.58$. The two peak regions (global & local optima) are separated by a dip in the population fitness values. This is seen in the pattern of the less fit members of the population, represented as smaller dots for various Γ as the individuals evolve.

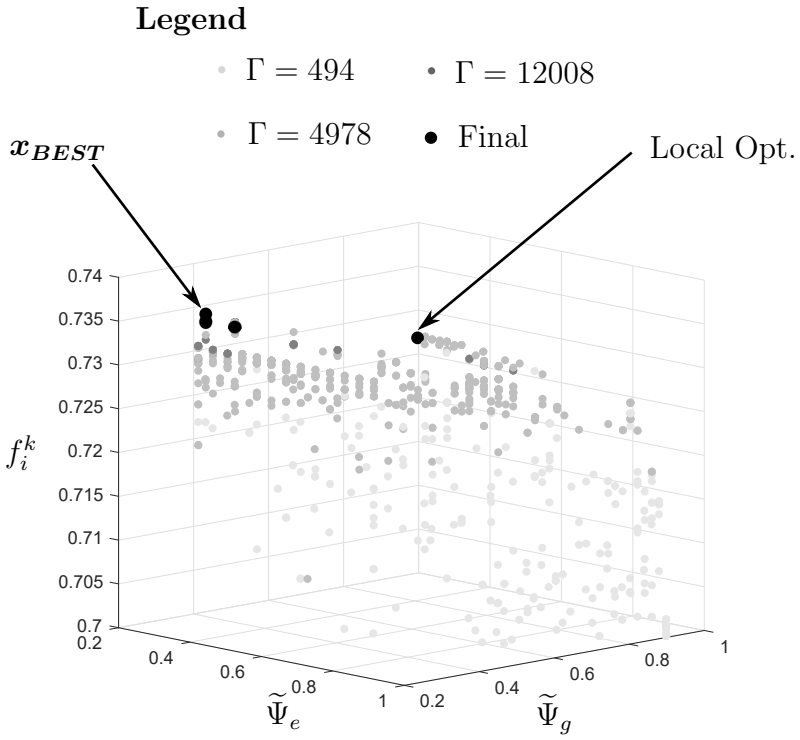

Figure 3.5: Rocket path $\widetilde{\Psi}_e$, $\widetilde{\Psi}_g$ hyperplane vs Fitness.

From Table 3.1, it can be seen that the largest difference between $\boldsymbol{x_{BEST}}$ and the final (Rank 4) individual occurs on the $\widetilde{z}_g$ and $\widetilde{r}_g$ genes. For these genes, this distant local optimum can also be seen in the plot shown in Fig. 3.6.

As with all evolutionary algorithms, DE can become trapped in a local optimum, especially when that optimum fitness value is very close to the true global optimum. However, the measure of performance of the algorithm is the probability of finding the global region on any given run, which can be evaluated using Dev_i in cases where the best individual is known. For the case of the rocket flow path, this is illustrated in Fig. 3.7.

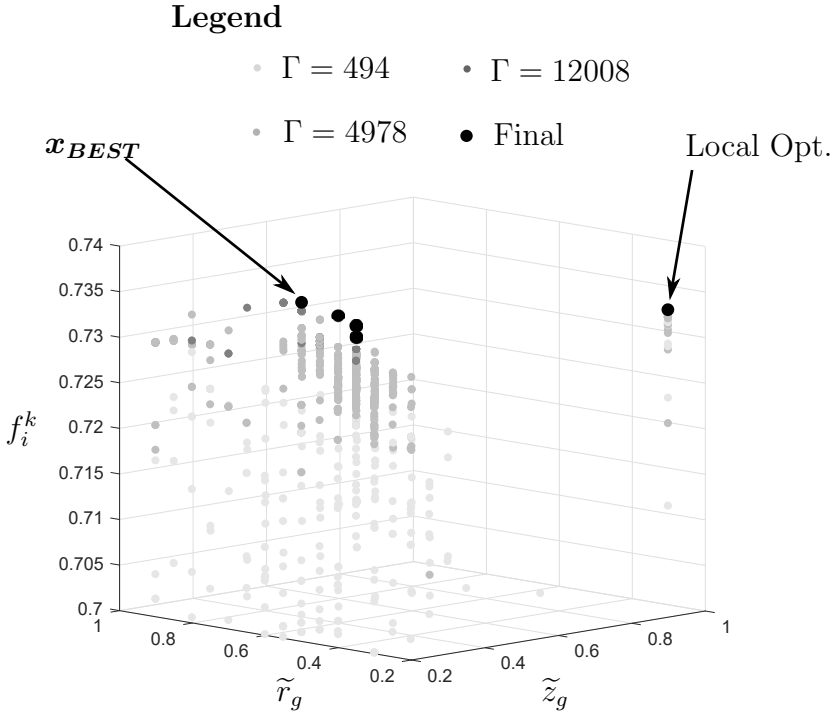

Figure 3.6: Rocket path $\widetilde{z}_g$, $\widetilde{r}_g$ hyperplane vs Fitness.

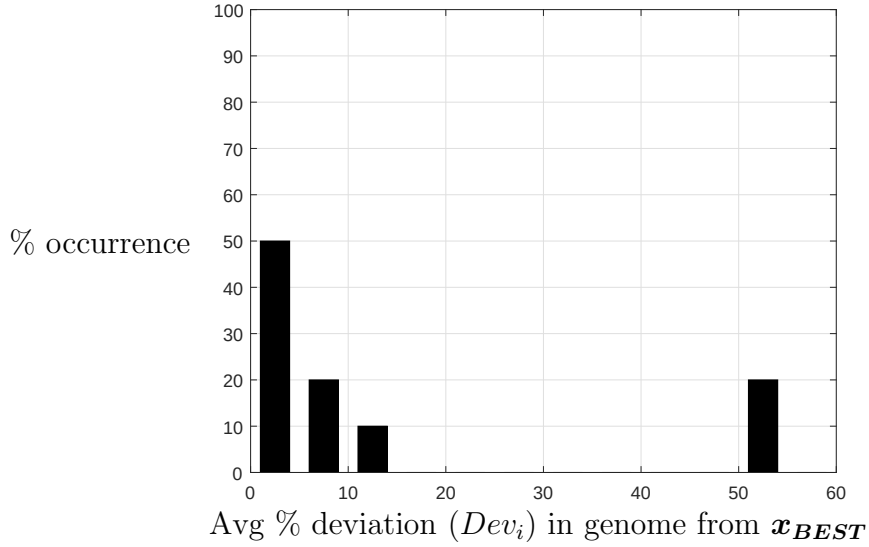

Figure 3.7: Rocket path average genome deviation in final individual from $\boldsymbol{x_{BEST}}$ vs % occurrence for 10 runs.

The distant local optimum shows up as a small spike around 55% difference in the genome. Based on the 10 trails conducted, this distant local optimum spike has a 20% chance of occurring on a given run. Figure 3.7 also shows that 70% of time DE found an individual that was within 10% of the true optimum, while the remaining 10% of the time it was within 15%. This gives an indication of how the DE algorithm will perform for a given set of parameters (m, F, C_r).

3.3 Exchange Inlet DE Tuning Results

Using all 8 genes for the individuals $\boldsymbol{x_i^k}$ from Eq.(2.11) the complete system model for the exchange inlet is able to determine both the air mass flow $\dot{m}_a$ and total pressure recovery $\overline{P_o}$ objectives. Thus, the exchange inlet system model uses the fitness function in Eq. (2.20). Not all individuals are considered fit as their gene combinations may represent non-physical solutions. As mentioned earlier, these individuals are simply assigned a fitness of zero, but they remain in the population and are allowed to mate. Though these individuals may represent invalid solutions, they can still produce fit children $\boldsymbol{u_i^{k+1}}$ through the donor $\boldsymbol{v_i^k}$ individuals and the crossover operation. The number of unfit individuals in any randomly generated population is quite large, while the number of fit individuals $f(\boldsymbol{x_i^k}) > 0$ is on average 2%. Therefore, using the total number of possible combinations $S \approx 5 * 10^9$ (5 billion), the total number of valid or fit possible individuals can be approximated as $S_{fit} \approx 1 * 10^8$ (100 million). Given this large number of possible valid (fit) combinations, and the 10-15 second evaluation time from Eq(2.20), it would take between 32-47 years to check all combinations. This could be reduced using parallel computing, however, given the available resources it is clearly not practical and thus differential evolution is utilized.

To prevent excessively large runs times, a maximum number of evaluations $\Gamma = 75000$ is used, which equates to $k = 1000$ generations at population size of $m = 75$.

As shown in the previous section, this is the metric over which the fitness of the most fit individual and population fitness variance is monitored. While the fitness of f_{best}^{k} shows the most fit individual, the progress of algorithm population convergence is shown by its fitness variance $Var(f_i^k)$. This variance represents the population diversity, which initially increases, then begins to decrease. As the population fitness variance (diversity) decreases, more individuals in the population become identical. Letting the algorithm evaluate individuals that already exist in the population with known fitness values is a waste computational time. Therefore, to avoid unnecessary evaluations and determine when the population has converged, each child candidate is checked to see if it exists in the population already. If it exists in the population, then the new child candidate $\boldsymbol{u_i^{k+1}}$ is simply assigned the same known fitness value. This takes less than $1ms$ or four orders of magnitude lower than an evaluation. Thus, as the population approaches total convergence, with many identical individuals, its computational time for evaluations rapidly decreases. This essentially terminates the algorithm upon convergence, as it will reach the maximum number of evaluations $\Gamma = 75000$ in less than 1 minute. The speed at which this convergence occurs will depend on the parameter settings (m, F, C_r). These settings are tuned to provide the most accurate results, without producing excessive computational run times. They are tuned over the ranges provided in section 2.2.1.

To tune the input parameters, a similar approach to section 3.2 is utilized. However, as it is not possible to know the best individual $\boldsymbol{x_{BEST}}$ given the large number of fit possible combinations, an approximation or known best $\boldsymbol{x^*_{Best}}$ is used in its place. This known best $\boldsymbol{x^*_{Best}}$ represents the best possible individual found during the DE parameter tuning for a single fixed set of weights (K_a=K_b=0.35, K_c=K_d=K_e=0.1). This therefore, will represent one point on the $\dot{m}_a/\overline{P_o}$ Pareto front. This $\boldsymbol{x^*_{Best}}$ individual along with 8 other most fit individuals found using the fixed set of weights, while varying the parameters m, F, and C_r are shown in Table 3.2.

Table 3.2: Top 8 fit individuals found vs the known best individual.

Rank	Fitness	$\widetilde{\Psi}_e$	$\widetilde{\Psi}_g$	$\widetilde{z}_g$	$\widetilde{r}_g$	$\widetilde{z}_2$	$\widetilde{t}_3$	$\widetilde{r}_{CB1}$	CR	Dev_i (%)
$\boldsymbol{x}^*_{\boldsymbol{Best}}$	0.63844	0.98	0.3	0.5	0.55	0.36	0.1	3.5	1.4	-
1	0.63826	0.98	0.3	0.5	0.55	0.36	0.12	3.5	1.4	1.56
2	0.63818	0.98	0.3	0.5	0.55	0.36	0.06	3.5	1.4	3.13
3	0.6361	0.66	0.3	0.5	0.5	0.32	0.06	3	1.4	12.75
4	0.63582	0.98	0.3	0.5	0.55	0.36	0.08	4	1.4	2.52
5	0.63575	0.98	0.3	0.5	0.55	0.36	0.06	4	1.4	4.09
6	0.63397	0.98	0.3	0.5	0.6	0.38	0.06	4	1.4	6.06
7	0.63239	0.96	0.3	0.5	0.6	0.38	0.06	2	1.4	8.33
8	0.63186	0.98	0.3	0.35	0.65	0.44	0.06	5	1.4	14.72

The individuals listed in Table 3.2 are the 8 different final individuals found during 55 runs that are part of the DE algorithm parameter tuning. Out of the 55 runs conducted during the algorithm tuning, the single $\boldsymbol{x}^*_{\boldsymbol{Best}}$ individual is found 27% of time. The Rank 3 individual represents a near local optimum with a Dev_i=12.75%. The $\boldsymbol{x}^*_{\boldsymbol{Best}}$ individual is the known best and is used as the benchmark for detecting a global optimal region, in the same manner as section 3.2 demonstrated for the rocket path. Though it is not possible to state with 100% confidence that the known best is the true global optimum, the random distribution of the initial population is employed to ensure no large regions of the search space remain unexplored. To improve search space coverage, repeating runs for each parameter setting is used in combination with random initial populations.

There are 8 unique parameter combinations of m, F, and C_r for which there are five repeated runs. The final parameter settings which are selected as the tuned settings represent a 9th combination of ($m = 75$,$F = 0.85$,$C_r = 0.3$), which is run 15 times for improved accuracy, see Table 3.3.

Table 3.3: Parameter combinations used in DE tuning.

Combination	m	F	C_r	Runs
1	25	0.9	0.5	5
2	50	0.9	0.5	5
3	75	0.9	0.5	5
4	75	0.85	0.5	5
5	75	0.95	0.5	5
6	75	0.9	0.9	5
7	75	0.9	0.7	5
8	75	0.9	0.3	5
9†	75	0.85	0.3	15

† *Final selection is run* 10 *additional times.*

The initial search space coverage is examined by the use of hyperplanes. The amount of coverage will depend on the number of runs and the size of the hyperplane. Four hyperplanes are illustrated in Fig 3.8, showing the locations of the initial ($k = 1$) population members for 5 runs (different markers) at $m = 75$, $F = 0.9$ and $C_r = 0.5$.

As can be seen in the figures, the largest hyperplane is the $\widetilde{\Psi}_e$, $\widetilde{\Psi}_g$ hyperplane, with 1116 possible locations determined by the upper and lower bounds, as well as the gene resolutions. This hyperplane shows 28% coverage for 5 runs, with a uniform distribution. The smallest hyperplane is the $\widetilde{z}_2$, $\widetilde{t}_3$ hyperplane, with 88 possible locations and 97% coverage. By repeating runs for each setting and demonstrating a uniform search space coverage, the probability of an unknown and undetected global optimum region is decreased. Therefore, the probability the known best $\boldsymbol{x}^*_{\boldsymbol{Best}}$ is in the true global region is increased.

As with the rocket path in section 3.2, the path of the fitness of the most fit individual in the population f^k_{best} is different for each run. The number of non-zero

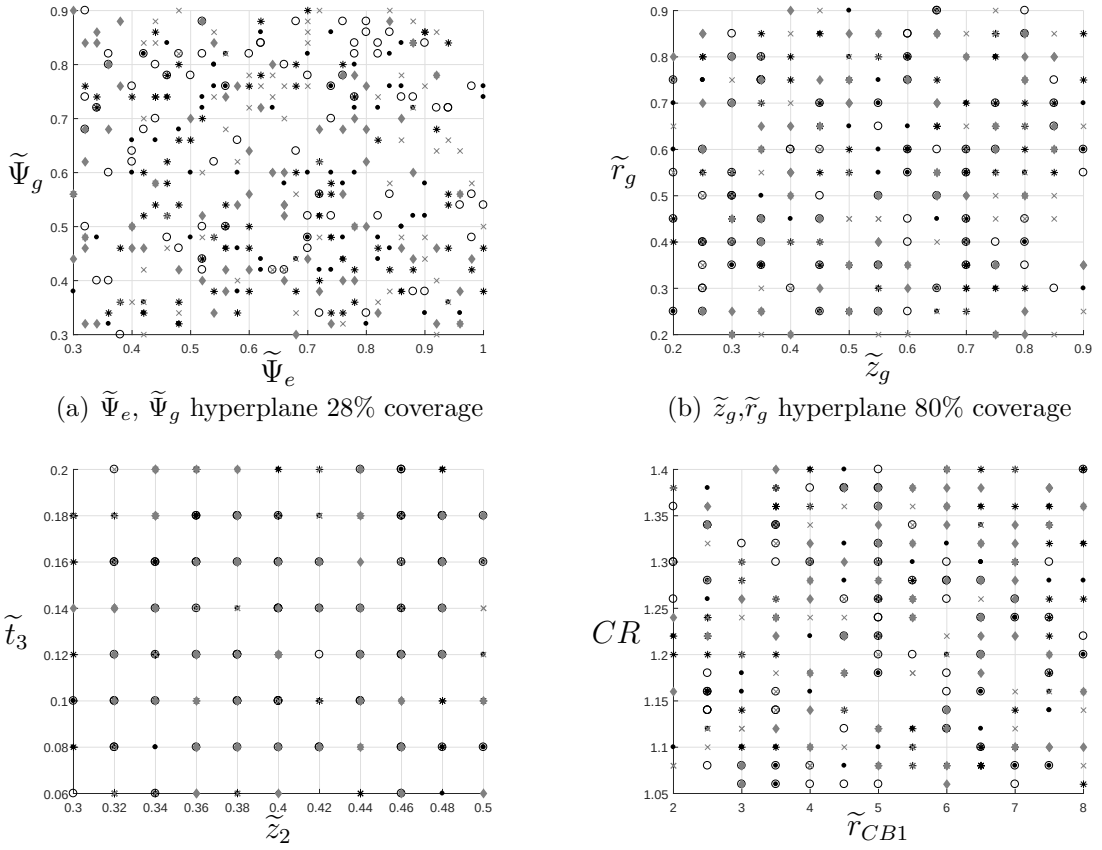

(a) $\widetilde{\Psi}_e$, $\widetilde{\Psi}_g$ hyperplane 28% coverage

(b) $\widetilde{z}_g$,$\widetilde{r}_g$ hyperplane 80% coverage

(c) $\widetilde{z}_2$, $\widetilde{t}_3$ hyperplane 97% coverage

(d) $\widetilde{r}_{CB1}$, CR hyperplane 81% coverage

Figure 3.8: Initial % coverage of search space hyperplanes for 5 runs at $m = 75$, $F = 0.9$ and $C_r = 0.5$

fitness NNZ and population fitness variance $Var(f_i^k)$ also follows a similar trend as seen in section 3.2. This is illustrated, for example, in Fig. 3.9 to Fig. 3.11 for 5 runs, at $m = 75$, $F = 0.9$ and $C_r = 0.5$.

As the plots in Fig. 3.10 and Fig. 3.11 show, the number of non-zero fitness individuals and population fitness variance both stabilize around 100 generations (Γ=7500). This is far sooner than the plot in Fig. 3.9 which stabilizes as late as 250 generations (Γ=18750). This indicates that although after 100 generations the algorithm has found 75 fit individuals near the optimal region, it requires as much as another 150 generations to refine the solution and exploit the genes of the individuals in the population.

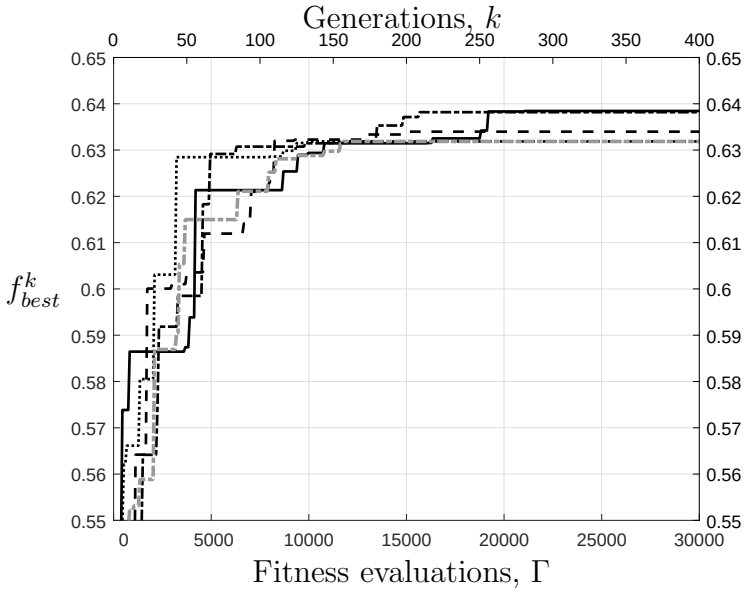

Figure 3.9: Fitness of most fit individual vs total evaluations for EI at $m = 75$, $F = 0.9$ and $C_r = 0.5$.

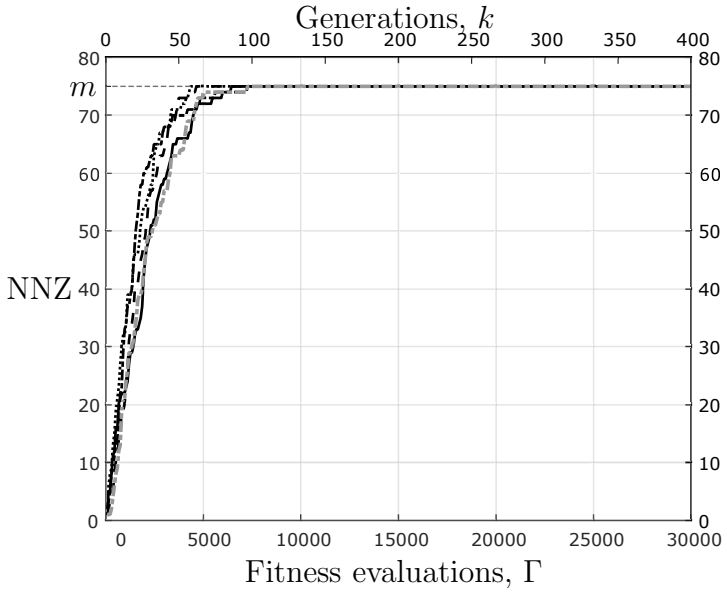

Figure 3.10: Number of non-zero fitness values vs total evaluations for EI at $m = 75$, $F = 0.9$ and $C_r = 0.5$.

The plots in Fig. 3.9 to Fig. 3.11 represent runs at a single setting of input parameters (m, F, C_r). For clarity during parameter tuning, however, it is preferable

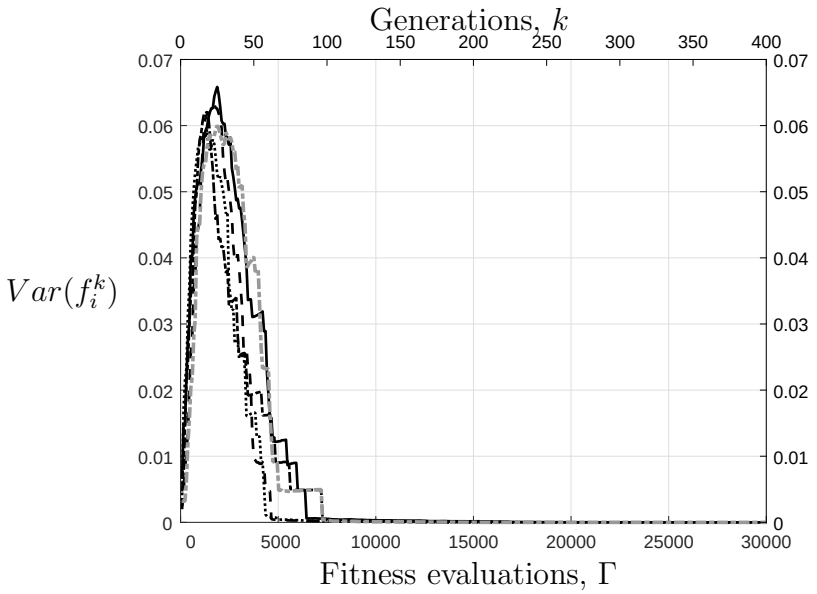

Figure 3.11: Variance of population fitness values vs total evaluations for EI at $m = 75$, $F = 0.9$ and $C_r = 0.5$.

to compare the average values of all 5 runs for each setting. The three input parameters of population size (m), differential weight (F), and crossover probability (C_r) can be varied sequentially, to determine which combination most often results in a near optimal solution, based on the known best $\boldsymbol{x}^*_{\boldsymbol{Best}}$. All tuning is performed at a freestream Mach number of $M_\infty = 2.5$, as it represents the transition point from ejector to ramjet mode and is near the middle of the supersonic range $M_\infty = 1.2$ to $M_\infty = 4$ considered.

3.3.1 Effect of Population Size

The input parameter of population size is varied between $m = 25, 50,$ & 75, which corresponds to $3.125n, 6.25n,$ & $9.375n$. The purpose of tuning is to examine the effect of the input parameters on the average fitness of the most fit individuals $\overline{f}^k_{best}$, the average population fitness variance $\overline{Var}(f_i^k)$, and the occurrence vs average genome deviation Dev_i from the known best. The average population fitness variance $\overline{Var}(f_i^k)$

provides information about the rate of the total population convergence. It is also a measure of the population diversity, as more individuals that converge on optimal regions become identical. The occurrence demonstrates how often the parameter setting results in an individual at or near the known best individual $\boldsymbol{x}^*_{\boldsymbol{Best}}$. For each population size the values of F and C_r are kept constant, see Table 3.3.

Since m varies in size, Γ is used as the comparative metric (rather than (k)) since smaller populations sizes have fewer individuals to evaluate for each generation. Therefore, a smaller population size will require more generations to evalute the same number of individuals as a larger population, refer to Eq. (3.4). Thus, the averaged values ($\overline{f}^k_{best}$, $\overline{Var}(f^k_i)$) will be compared over the number of evaluations Γ only, since the number of generations will differ between the population sizes. The average fitness $\overline{f}^k_{best}$ and average variance $\overline{Var}(f^k_i)$ are shown in Fig. 3.12 and Fig 3.13.

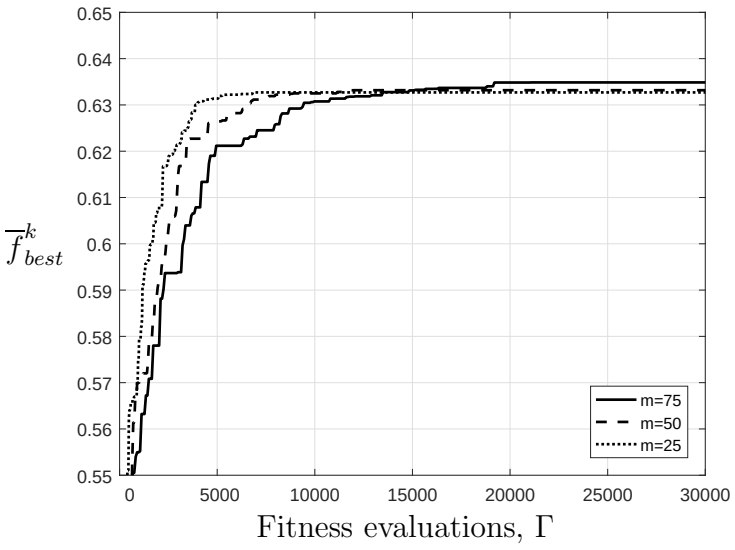

Figure 3.12: EI average fitness of most fit individual vs total evaluations for varying m ($F = 0.9$, $C_r = 0.5$).

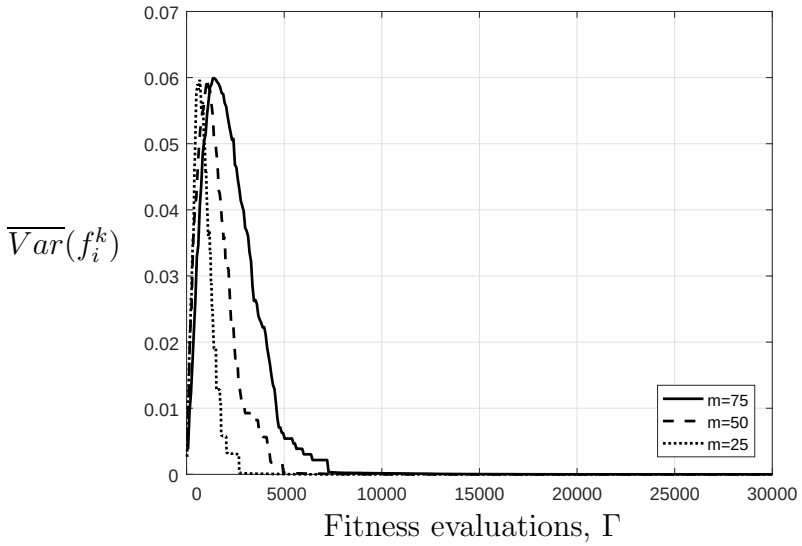

Figure 3.13: EI average population fitness variance vs total evaluations for varying m ($F = 0.9$, $C_r = 0.5$).

As shown in Fig. 3.12 the average fitness $\overline{f}_{best}^{k}$ of the 5 runs for each population size increases with population size. This is expected as larger populations would have more potential child candidates, thereby increasing the amount of search space that is explored. However, as noted in section 2.2.1, the population size cannot be arbitrarily increased. If the population size is set too large ($> 10n$) it can result in long run times. This can be seen in Fig. 3.12, as larger population sizes tend to take longer to reach a similar fitness value. This is because larger population sizes will slow the rate of population convergence of the algorithm, as seen in Fig. 3.13. The effect, therefore, of slowing the convergence is to give the DE algorithm more time to explore the search space. This results in higher average fitness values. Though smaller population sizes have better run times, due to faster convergence, they run the risk of premature convergence. The premature convergence is a result of the smaller population size losing diversity too quickly, as more and more individuals become similar or identical.

In Fig. 3.13, the variance $\overline{Var}(f_i^k)$ starts off low as few fit individuals exist in the initial population, however this rapidly increases with each generation. After the diversity peaks, the selection pressure begins reducing the diversity of the population. This occurs as the population evolves towards more fit regions of the search space, as individuals become replaced with more fit children at each generation. Eventually, the selection pressure will force the population to converge into the most optimal region or regions, corresponding to either a single individual or a very small number of individuals.

The population size m=75 shows the slowest convergence, but also the best average fitness value. This population size is also not considered to be too large, as is falls within the accepted range suggested by Mallipeddi et al. [66] and Storn & Price [50]. The average fitness value, however, does not indicate if these individuals are near the global region, or if they are distant local optimums with high peak values. Therefore, the performance of occurrence near the known best $\boldsymbol{x}^*_{\boldsymbol{Best}}$ for each population size is shown in Fig 3.14.

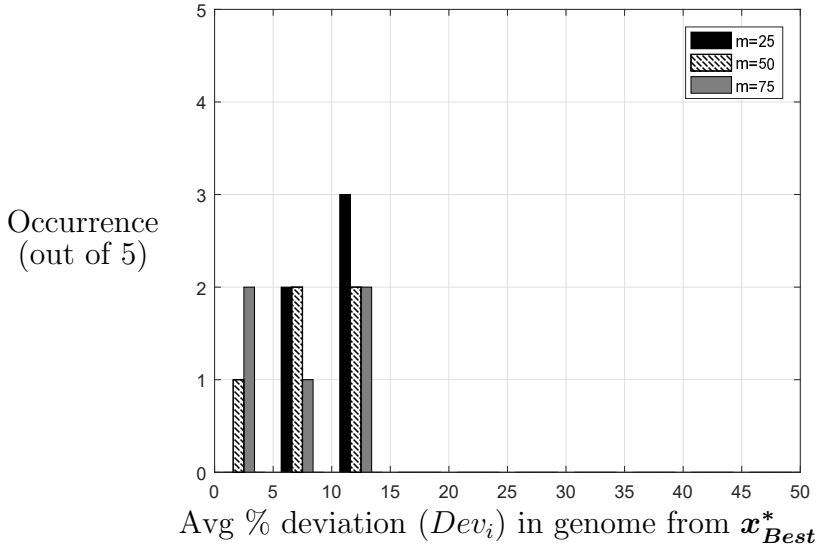

Figure 3.14: EI occurrence vs average genome deviation (Dev_i) for 5 runs at m=25, 50 & 75 ($F = 0.9$, $C_r = 0.5$).

The occurrence of each population size, in Fig 3.14, shows that the larger the population size, the higher the chance it will converge closer to the known best $\boldsymbol{x}^*_{\boldsymbol{Best}}$, or the only known potential global region. Though the figures show no distant local optima, Table 3.2 does indicate there is a local optimum near the global region with a 12.75% (Rank 3 individual) deviation from the known best. This local optimum, however, falls into the 10-15% Dev_i region along with the Rank 8 individual from Table 3.2.

The results of Fig. 3.12 to Fig. 3.14 show that although a smaller population converges faster, it is less likely to produce an individual at (or very near) $\boldsymbol{x}^*_{\boldsymbol{Best}}$. Figure 3.14 indicates that the population converges too quickly for smaller populations as it approaches the potential global region. Thus, in the case m=25 it never comes within 5% of this region, where as for m=50 and m=75 it occurs 1/5 and 2/5 times respectively. For the given range tested, the value of m=75 is the best choice of population size, without arbitrarily increasing beyond $10n$.

3.3.2 Effect of Differential Weight

The second input parameter, the differential weight F, is examined in the same manner as population size. With population size fixed at $m = 75$, and a default value of $C_r = 0.5$, the differential weight can be varied over the range $F = 0.85, 0.9, \&0.95$ as discussed in section 2.2.1. The resulting effect on both the average fitness of the most fit individual $\overline{f}^k_{best}$ and the average population fitness variance $\overline{Var}(f^k_i)$ are averaged over 5 runs. Each run has a different initial population with a uniform random distribution. The results of $\overline{f}^k_{best}$ and $\overline{Var}(f^k_i)$ vs the number of evaluations Γ (& Generations k) are shown Fig. 3.15 and Fig. 3.16.

Both Fig. 3.15 and Fig. 3.16 show that varying the differential weight over the range $F = 0.85$ to $F = 0.95$, did not have a significant effect on the average fitness $\overline{f}^k_{best}$ or the average variance $\overline{Var}(f^k_i)$. The average variance was not significantly

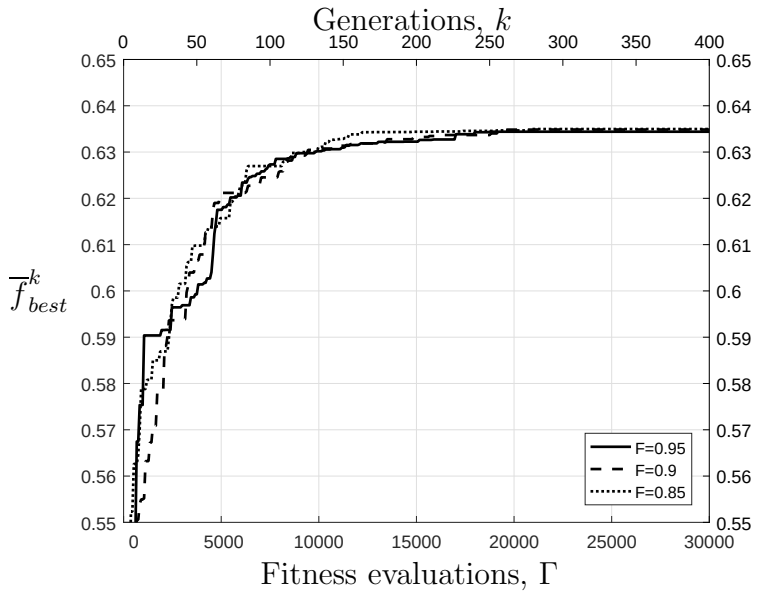

Figure 3.15: EI average fitness of most fit individual vs total evaluations for varying F ($m = 75$, $C_r = 0.5$).

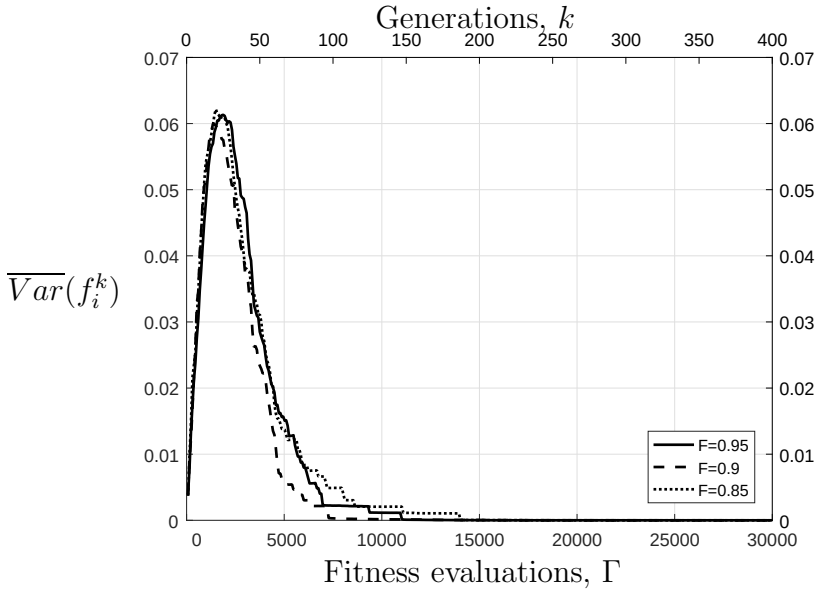

Figure 3.16: EI average population fitness variance vs total evaluations for varying F ($m = 75$, $C_r = 0.5$).

affected over most of the range, only differing slightly at very low levels of variance. The results on the occurrence out of 5 runs for F=0.85, F=0.9 and F=0.95 are shown in Fig. 3.17.

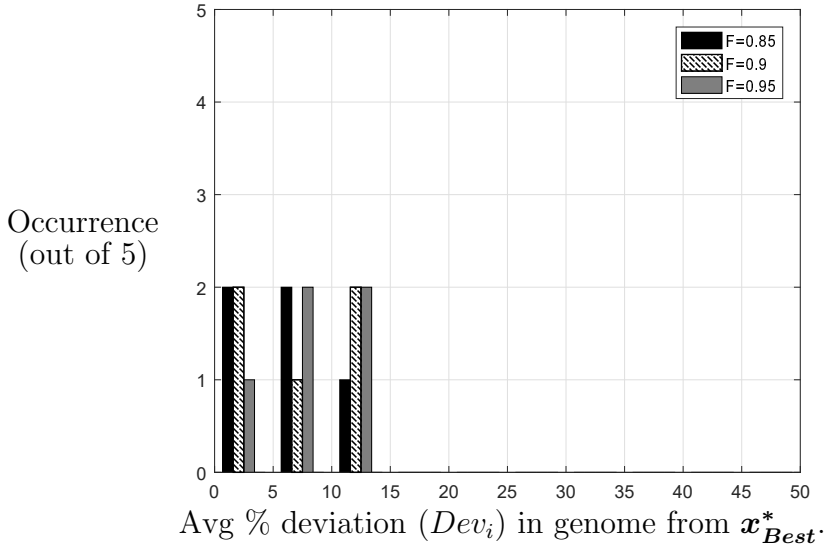

Figure 3.17: EI occurrence vs average genome deviation (Dev_i) for 5 runs at F=0.85, 0.9 & 0.95 ($m = 75$, $C_r = 0.5$).

Though the results did not differ significantly, Fig. 3.17 shows that only 1 out of 5 times does $F = 0.95$ result in an individual that is within 5% average genome deviation from the known best individual $\boldsymbol{x}^*_{\boldsymbol{Best}}$. Both $F = 0.9$ and $F = 0.85$ show the same 2/5 occurrence for the 5% deviation range, however, in the 5-10% range the $F = 0.85$ shows slightly better results at 2/5 occurrence, vs 1/5 for $F = 0.9$. Therefore, both $F = 0.9$ and $F = 0.85$ will be investigated in the following sections.

3.3.3 Effect of Crossover Probability

The final input parameter is the crossover probability C_r, which is varied from $C_r = 0.3, 0.5, 0.7, \&0.9$, as discussed in section 2.2.1. This is done initially with $m = 75$ and $F = 0.9$ for all C_r values. The best value of C_r, however, is also compared for $F = 0.9$ vs $F = 0.85$, as the results from section 3.3.2 indicated $F = 0.85$ might be a better choice. The results of $\overline{f}^k_{best}$ and $\overline{Var}(f^k_i)$ vs the number of evaluations Γ are shown in Fig. 3.18 and Fig. 3.19.

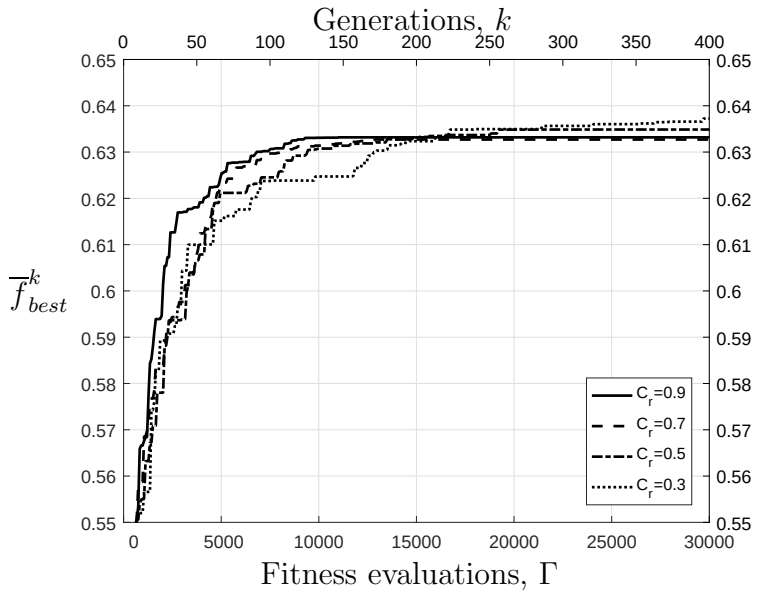

Figure 3.18: EI average fitness of most fit individual vs total evaluations for varying C_r ($m = 75$, $F = 0.9$).

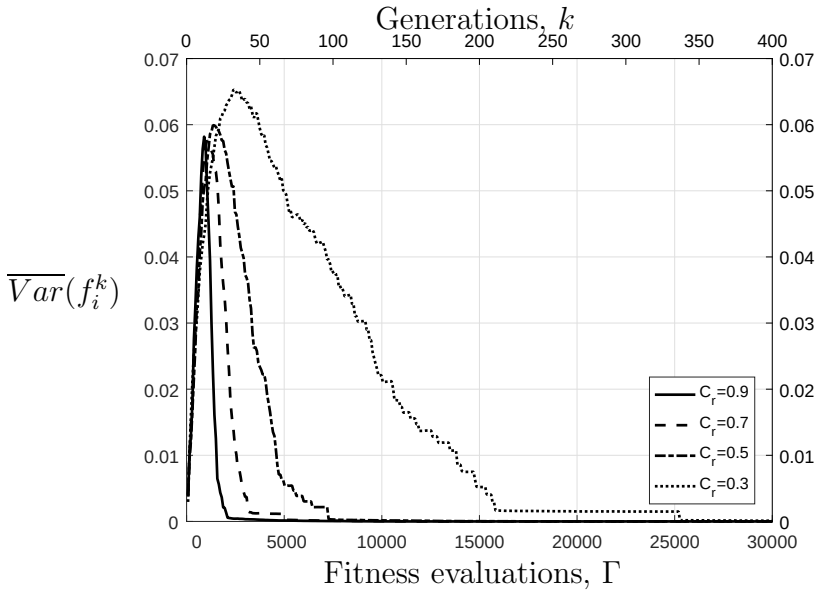

Figure 3.19: EI average population fitness variance vs total evaluations for varying C_r ($m = 75$, $F = 0.9$).

The results of Fig. 3.18 show a general improvement for average fitness $\overline{f}^k_{best}$ as C_r is decreased below 0.7. The value of $C_r = 0.9$, however, shows a slight improvement

over $C_r = 0.7$. Higher C_r values mean a higher probability that child $\boldsymbol{u_i^{k+1}}$ will inherit genes from the donor $\boldsymbol{v_i^k}$ individual. This can increase the explorative properties of the algorithm, as it results in large multi-dimensional jumps in the search space. On any given run, this can result in rapidly locating an optimal region. However, it can also result in many jumps to unfit or invalid regions as well. The result is that even if an optimal region is found, the algorithm many not progress further if too many of the crossover operations result in less fit or unfit individuals. In this case, the algorithm can prematurely converge on the location of the current optimum, before it has a chance to find a better location. This can be the case if the global optimum is close to a local optimum. The algorithm may not be exploitative enough to find nearby optimal regions, as it is exploring on too many axes at once. This is more likely to be the case when the search space axes and objective space axes are closely aligned. In this case, lower C_r values are preferred.

The rapid convergence for higher C_r values is illustrated in Fig. 3.19, which shows the average fitness variance $\overline{Var}(f_i^k)$ as a function of the number of evaluations Γ. The lower values of C_r not only show higher peak diversity, but also a slower rate of population convergence. The population diversity, therefore, is prolonged and gives the algorithm more time to not only explore regions, but exploit them, by exploring on fewer axes at a time. The slower convergence does, however, result in a slower algorithm. The value of $C_r = 0.5$, for example, takes on average 2 days to run, whereas $C_r = 0.3$ take almost 4 days. To compare the results of nearly doubling the run time, the improvement in the probability of finding an individual near or at $\boldsymbol{x^*_{Best}}$ must be examined. The results on the occurrence out of 5 runs are shown in Fig. 3.20.

The results of Fig. 3.20 demonstrate why the $C_r = 0.9$ value showed slightly higher average fitness $\overline{f}^k_{best}$, than the $C_r = 0.7$ value. The $C_r = 0.9$ parameter setting did find a value within 5% of $\boldsymbol{x^*_{Best}}$ 1 out of 5 times, while the $C_r = 0.7$

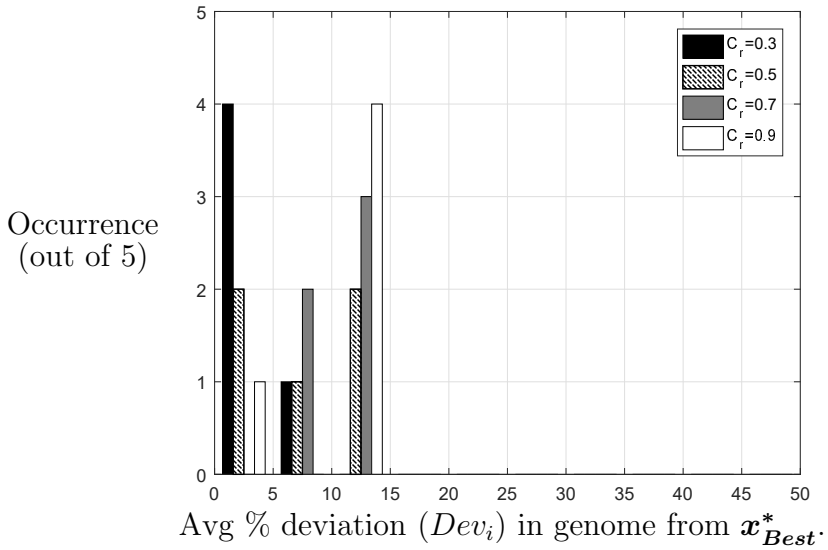

Figure 3.20: EI occurrence vs average genome deviation (Dev_i) for 5 runs at C_r=0.3, 0.5, 0.7 & 0.9 ($m = 75$, $F = 0.9$).

never did. The $C_r = 0.7$ did have better results in the 5-10% of known best $\boldsymbol{x}^*_{\boldsymbol{Best}}$ range, while $C_r = 0.9$ prematurely converged on the 10-15% range 4 out of 5 times. Neither of these values are considered good settings for C_r in the exchange inlet problem. The values of $C_r = 0.5$ showed individuals within 5% of $\boldsymbol{x}^*_{\boldsymbol{Best}}$ 2 out of 5 times, while this value doubled to 4/5 occurrence for $C_r = 0.3$. Therefore, while $C_r = 0.3$ requires approximately double the run time, it also doubled the probability of finding an individual at or near $\boldsymbol{x}^*_{\boldsymbol{Best}}$. Values below $C_r = 0.3$, however, required excessively long run times and are not considered here, since a 4/5 success rate is deemed acceptable. In addition, the remaining 1/5 of the time the $C_r = 0.3$ produces individuals within 5-10% of $\boldsymbol{x}^*_{\boldsymbol{Best}}$.

3.3.4 Final Parameter Selection

The results from Fig. 3.20 are all at F=0.9. However, the values of m=75 and C_r=0.3 will be used in combination with F=0.85. This is due to the slight improvement of

F=0.85 over F=0.9 that is seen in section 3.3.2. Additionally, since this input parameter combination (m=75, F=0.85, C_r=0.3) is selected based on the best performance of the previous results, 15 runs will be used instead of 5. This is to ensure accuracy of the final parameter selection in terms of % occurrence. The results are shown in Fig. 3.21.

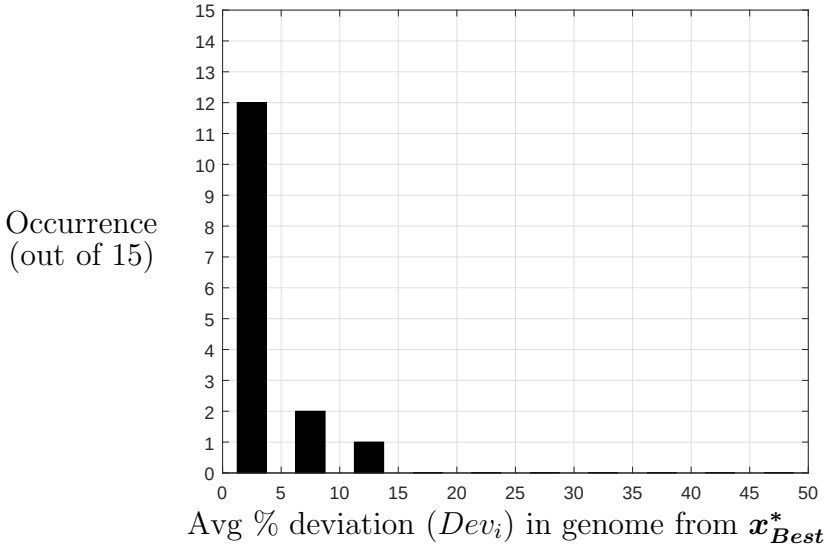

Figure 3.21: EI % occurrence vs average genome deviation (Dev_i) for 15 runs at m=75, F=0.85, C_r=0.3.

The Fig. 3.21 shows similar results to the m=75, F=0.9, and C_r=0.3 combination in Fig. 3.20. The m=75, F=0.85, and C_r=0.3 combination occurred in the 0-5% Dev_i range in 12 out of 15 runs, or 80% of the time, while Dev_i was in the 5-10% range 2/15 or 13.3% of the time. The remaining run occurred in the 10-15% Dev_i range, which is not considered acceptable as it contains a local optimum, refer to Table 3.2. Therefore, the settings in Fig. 3.21 are in the acceptable range in 14/15 runs, or 93.3% of the time. The values of m=75, F=0.85, and C_r=0.3 are selected for the remainder of this work. The final input parameter values are listed in Table 3.4.

Table 3.4: Final input parameter settings for DE algorithm.

Input parameter	Value
Population size (m)	75
Differential weight (F)	0.85
Crossover probability (C_r)	0.3

Chapter 4

Exchange Inlet Optimization Results

4.1 Supersonic Trajectory and Overview

To follow a path similar to the airbreathing flight requirement laid out by Whitehead [8] in Fig. 1.2 of Chapter 1, the freestream velocity (and Mach number) is increased with altitude to allow the oxygen flux needed for airbreathing propulsion. However, rather than a constant oxygen flux, this is done by maintaining a constant dynamic pressure (q) of 30 kPa, given by Eq. (4.1).

$$q = \frac{\gamma P_\infty M_\infty^2}{2} \tag{4.1}$$

The resulting flight profile for the RBCC engine is determined by this dynamic pressure (as described by Murzionak [36]) using a NASA atmospheric model. The constant dynamic pressure is selected to be within both structural/thermal limits of materials and combustion stability [36]. A flight profile of the RBCC engine from M_∞=1.2 (363 m/s) to M_∞=4 (1180 m/s) is shown in Fig. 4.1, along with both the rocket and airbreathing engine profiles, and the oxygen flux lines (1,10,100 $\frac{kg}{s*m^2}$) from Fig. 1.2.

As Fig.4.1 shows, the RBCC flight profile starts off near the rocket trajectory,

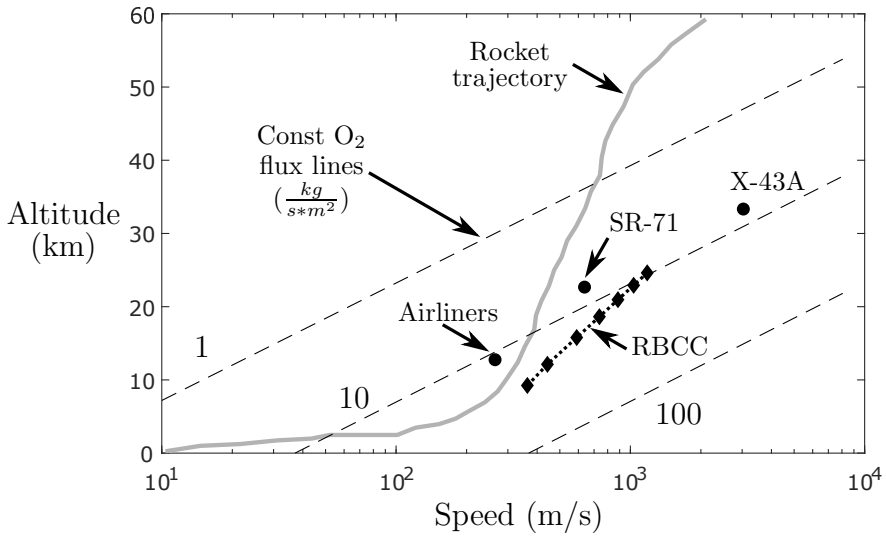

Figure 4.1: RBCC engine flight profile [8, 36].

however, as its speed increases it begins to assume a profile closer to other air-breathing vehicles. To maintain a constant dynamic pressure of 30 kPa, the altitude increases with increasing RBCC vehicle speed. Correspondingly, the density (and temperature) change as a function of altitude based on the NASA atmospheric model. Therefore, since the air mass flow $\dot{m}_a$ and total pressure recovery $\overline{P_o}$ are normalized in the fitness function using theoretical maximums ($\dot{m}_{max}$ & P_{o_∞}, refer to Eq.(2.18) & Eq.(2.20)) from freestream properties, each flight speed will require a different theoretical maximum value of $\dot{m}_{max}$ and P_{o_∞}. Each point on the RBCC flight profile in Fig. 4.1 represents a different vehicle speed between M_∞=1.2 and M_∞=4, however, only M_∞=1.5, M_∞=2.5 and M_∞=3.5 will be examined for optimization in this work. The altitude, freestream values, and theoretical maximums $\dot{m}_{max}$ & P_{o_∞} for each of the RBCC vehicle flight speeds shown in Fig. 4.1 are listed in Table 4.1.

Table 4.1: Altitude and freestream air properties over a flight profile at constant dynamic pressure of 30 kPa.

Mach	Speed (m/s)	Altitude (km)	Static pressure $P_\infty(kPa)$	Static Temp. $T_\infty(K)$	Total pressure $P_{o_\infty}(kPa)$	Max air mass flow $\dot{m}_{max}(kg/s)$
1.2	363	9.24	29.76	228.25	72.17	4984.6
1.5†	443	12.12	19.04	216.69	69.91	4091.7
2	590	15.79	10.71	216.69	83.82	3069.1
2.5†	738	18.63	6.86	216.69	117.16	2455.5
3	885	20.95	4.76	216.69	174.87	2045.8
3.5†	1032	22.92	3.50	216.69	266.76	1753.5
4	1180	24.62	2.68	216.69	406.64	1534.5

†*Freestream Mach number used in optimization.*

Recalling Fig. 2.20, each of the three exchange inlet components (center body, fairings, cowl) generates a shock wave. These shock waves affect both the air mass flow and total pressure recovery at the inlet. For a fixed geometry then, these shock waves will change in shape and strength as the freestream Mach number changes. Therefore, a fixed geometry can only be optimized at a single flight Mach number. The alternative is to use a geometry than can vary in shape as the freestream Mach number is increased, however, this would add extra complexity to the design of the engine inlet.

To optimize the exchange inlet (assuming a fixed geometry) over the supersonic flight regime, a Pareto front is developed at M_∞=2.5. From the Pareto front, a single individual corresponding to a single weight setting can be selected as the most fit individual for that freestream flight Mach number. This will be done for two other

Mach numbers, M_∞=1.5 and M_∞=3.5, which will result in three different optimized fixed geometries for three different flight Mach numbers.

Each of the three most fit geometries, corresponding to M_∞=1.5, 2.5 & 3.5, can then be observed over the full flight range M_∞=1.2 to M_∞=4 to compare their performance for the $\dot{m}_a$ and $\overline{P_o}$ objectives. Using fixed geometries, each design is expected to be the most optimal near its corresponding flight (M_∞) number. The trade off between using a fixed or variable geometry can then by seen by examining the performance improvements in the off design flight conditions over the supersonic range. The following results show the RBCC inlet performance objectives, and the Pareto fronts for each of the three Mach numbers.

4.2 Fixed Geometries at a Single Mach Number

4.2.1 Mach 2.5 Results

4.2.1.1 K_a vs K_b Pareto front

The exchange inlet fitness function, Eq.(2.20), has five objectives, each with its own weight. Each of these objectives represents an axis of the objective space. Therefore, the objective space is a 5-dimensional space, which contains a feasible region (5-dimensional 'volume') of all possible solutions. The Pareto front is then a 4-dimensional 'surface' at the boundary of the feasible region, which contains the most fit (or optimal) individuals. A two-dimensional example was given in section 2.1 with Fig. 2.2 & Fig. 2.3. As discussed in section 2.1, with all multi-objective problems the optimal or most fit individuals will consist of many solutions along the Pareto front corresponding to all possible weight vectors. The location of the most fit individual (on this front) is a function of the weights. In order to determine a desired optimum, a Pareto front must be obtained to observe the effect of the weights on the desired

objectives. In addition, for a true Pareto front to exist the objectives must be competitive with each other, i.e. they must have a negative correlation. If the objectives do not compete with each other, then there is no trade off and the objectives can simply be maximized.

Since the objective space is 5-dimensional, hyperplanes are used to observe two objectives at a time. To investigate the Pareto front then, only two weights will be varied at a time with their sum remaining constant. The remaining objectives are assigned a fixed weight of 0.1, or 10% of the fitness function contribution. This means that the two weights investigated will sum to 0.7, or 70% of the fitness function contribution.

The two primary objectives which vary over the supersonic range are the air mass flow $\dot{m}_a$ and total pressure recovery $\overline{P_o}$. These objectives are important for the air breathing ramjet (& scramjet) flight modes. Using a single set of weights (K_a,K_b) for these two objectives, the fitness function and selection process of the DE algorithm will direct the evolution of an initial population towards a specific point on the Pareto front hyperplane of the $\dot{m}_a$ and $\overline{P_o}$ objectives. This is illustrated in Fig. 4.2 and Fig. 4.3 for weights K_a=K_b=0.35.

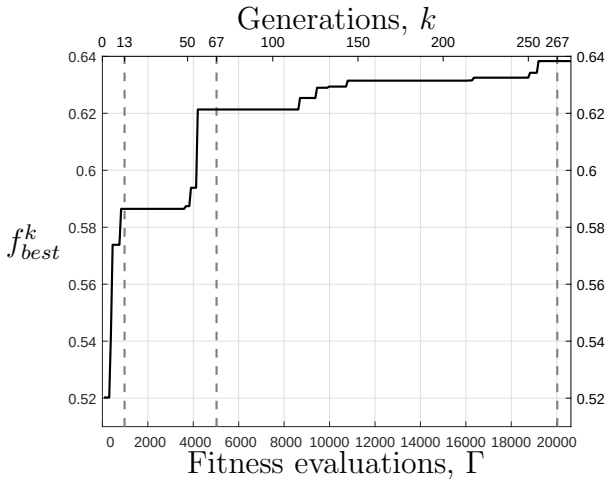

Figure 4.2: Evolution of f^k_{best} vs Γ, k for K_a=K_b=0.35 (K_c=K_d=K_e=0.1)

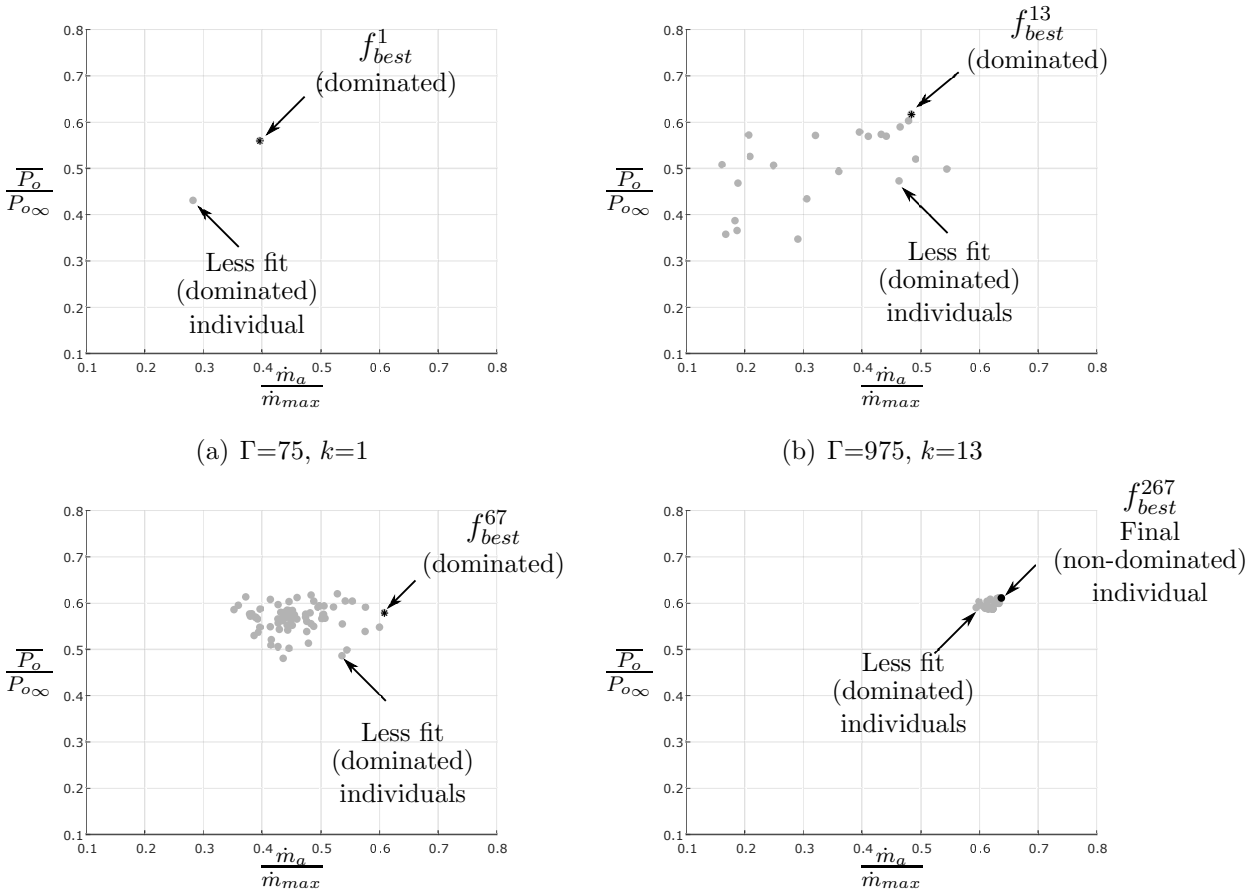

(a) Γ=75, k=1

(b) Γ=975, k=13

(c) Γ=5025, k=67

(d) Γ=20025, k=267

Figure 4.3: Objective space $\frac{\dot{m}_a}{\dot{m}_{max}}$, $\frac{\overline{P_o}}{P_{o\infty}}$ hyperplane evolution vs Γ, k for K_a=K_b=0.35 (K_c=K_d=K_e=0.1)

Figure 4.2 shows the evolution of the most fit individual f^k_{best} for each generation k (as was demonstrated in section 3.3). Correspondingly, Fig. 4.3 shows this evolution in the objective space $\frac{\dot{m}_a}{\dot{m}_{max}}$, $\frac{\overline{P_o}}{P_{o\infty}}$ hyperplane for the single set of weights at the initial (k=1) generation and later at k=13, 67 and 267. The initial population is randomly generated with only two valid ($f^k_i \neq 0$) individuals in the plane, but as the selection process occurs at each generation more valid individuals appear, and the population moves towards a specific location on the Pareto front. The most fit individual at each generation f^k_{best} is shown in black, while the less fit (but valid) members of the population are shown as grey dots. All individuals which are behind the Pareto front

are said to be dominated (refer to section 2.1). Even the most fit individuals at generations (k=1,13 & 67) are considered dominated as they have not yet reached the Pareto front, and are still improving. Eventually, the population converges on a single location on the Pareto front as seen at k=267 in Fig. 4.3(d), which represents the most fit individual for a specific set of weights (K_a=K_b=0.35). The Pareto front is considered to be reached in this case as the individual f_{best}^{267} is the known best $\boldsymbol{x}^*_{\boldsymbol{Best}}$ individual from Table 3.2. Subsequently, this individual can no longer be improved in one objective, without compromising another. The individual is then said to be non-dominated and therefore lies on the Pareto front. As the population moves towards this point in Fig. 4.3 (a)-(d), the diversity of the population decreases as the individuals become clustered together. This is the result of all members of the population converging towards the most optimal location. If the weights are changed then the fitness function will direct the DE algorithm to a new location on the Pareto front. By repeating the process for each new set of weights the shape of the Pareto front (in this hyperplane) can be realized.

For each weight setting of K_a and K_b, therefore, there will be a new most fit individual f_{best}^k, which corresponds to a new non-dominated point in the $\frac{\dot{m}_a}{\dot{m}_{max}}$, $\frac{\overline{P_o}}{P_{o_\infty}}$ hyperplane. Combining these points will define the shape of the Pareto front in the hyperplane. By varying the weights K_a and K_b (both sum to 0.7) this effect can be observed in Fig. 4.4, at $M_\infty = 2.5$, with the weights listed in Table 4.2 along with the objectives of f_{best}^k for each weight setting (maximums in bold).

The Pareto front points (black dots) in Fig. 4.4 represent the most fit individual for each of the different weight settings shown in Table 4.2, while the dominated (grey dots) represent the less fit possibilities that demonstrate the shape of the feasible region (section 2.1). These less fit (dominated) individuals are shown simply for observing the general shape of the feasible region. They are the locations of population members from earlier generations, before they converged onto the Pareto front.

Table 4.2: Weights K_a & K_b and objectives of f^k_{best} for M_∞=2.5 (K_c=K_d=K_e=0.1)

Point	K_a	K_b	$\dot{m}_a$ (kg/s)	$\overline{P_o}$ (kPa)	ϕ $(^\circ)$	L_{arc} (m)	$\frac{d^2\widetilde{r}}{d\widetilde{z}^2}$
1	0	0.7	872.14	74.48	**11.10**	9.15	**0.01321**
2	0.15	0.55	1210.6	**74.72**	55.39	17.66	0.03736
3	0.25	0.45	1568.3	71.46	56.71	19.45	0.12564
4	0.35	0.35	1568.3	71.46	56.71	19.45	0.12564
5	0.45	0.25	1569.5	71.44	56.71	**19.46**	0.12564
6	0.55	0.15	**1705.3**	72.50	47.57	15.82	0.30061
7	0.7	0	1550.7	68.04	60.73	18.37	0.05068

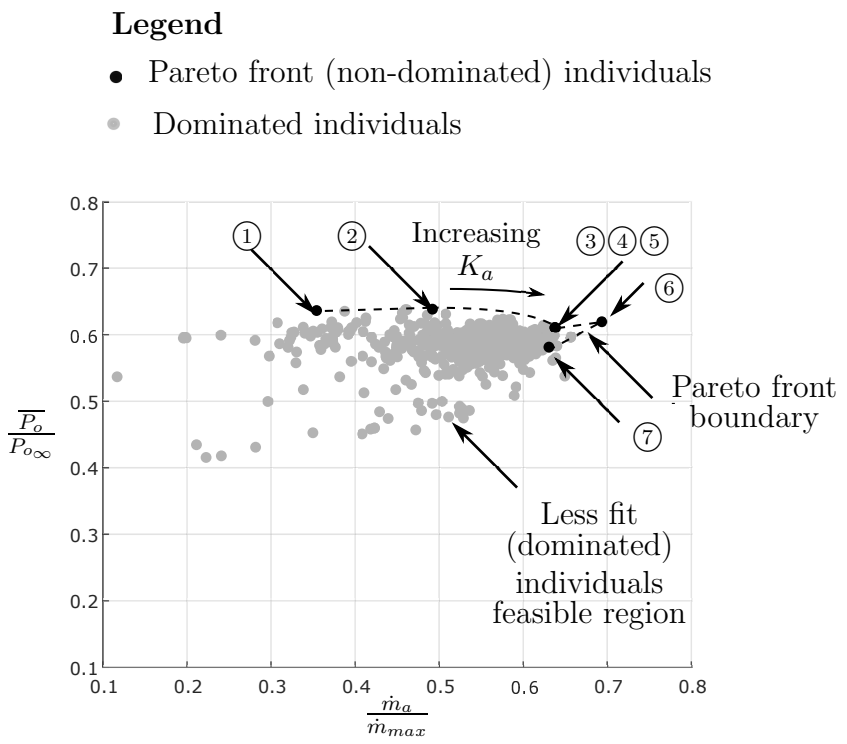

Figure 4.4: Pareto front for K_a and K_b objectives at $M_\infty = 2.5$ (K_c=K_d=K_e=0.1).

As K_a increases (K_b decreases) the location of the most fit individual moves along the Pareto front towards higher values of $\dot{m}_a$ (recall K_a is the weight associated

with $\dot{m}_a$ from Eq.(2.20)). This hyperplane is only a 2-dimensional slice of a higher dimensional space, therefore, there are some less fit individuals near Point ⑦ which appear to be near the Pareto front boundary. These individuals, however, are less fit than those on the Pareto front as the shape of the Pareto front is multi-dimensional. For a Pareto front in a two-objective problem, all less fit (dominated) individuals would be located behind the front. The other objectives (dimensions) are weighted much lower at 10% of the fitness function, therefore, they do have a minor affect on this boundary in other dimensions outside of the hyperplane. The Pareto front boundary is not defined after K_a=0.7 (Point ⑦).

The objective space hyperplane in Fig. 4.4 shows that the Pareto front appears relatively flat with a triangular point near the maximum for both objectives. This shape does not involve a gradual trade off, as would be expected with a concave shaped Pareto front (refer to Fig. 2.2 & Fig. 2.3). By increasing the weight K_a of the air mass flow $\dot{m}_a$ objective, the total pressure objective $\overline{P_o}$ first decreases slightly between Points ① & ③ then increases between Points ③ & ⑥, even though its own weight continues to decrease. The flatness of the upper boundary also shows little variation in the total pressure recovery objective. The total pressure recovery noticeably decreases at the extreme value at Point ⑦, where it is effectively removed as an objective due to $K_b = 0$. There is in fact a positive correlation between Points ③ & ⑦ for the two objectives for different weight settings, which can be illustrated by plotting the objectives as a function of their weights, see Fig. 4.5.

As Fig. 4.5 shows, for values below $K_a = 0.25$, there is a slight trade off as the value of K_a increases. This was also seen as a slight dip in $\frac{\overline{P_o}}{P_{o\infty}}$ from Points ① to ③ in Fig. 4.4. The value of $\dot{m}_a$ increases with K_a, while the value of $\overline{P_o}$ decreases slightly. However, for K_a values above 0.25, there is indeed a positive correlation between the normalized value of $\dot{m}_a$ and $\overline{P_o}$ as K_a is increased, with a maximum occurring around $K_a = 0.55$.

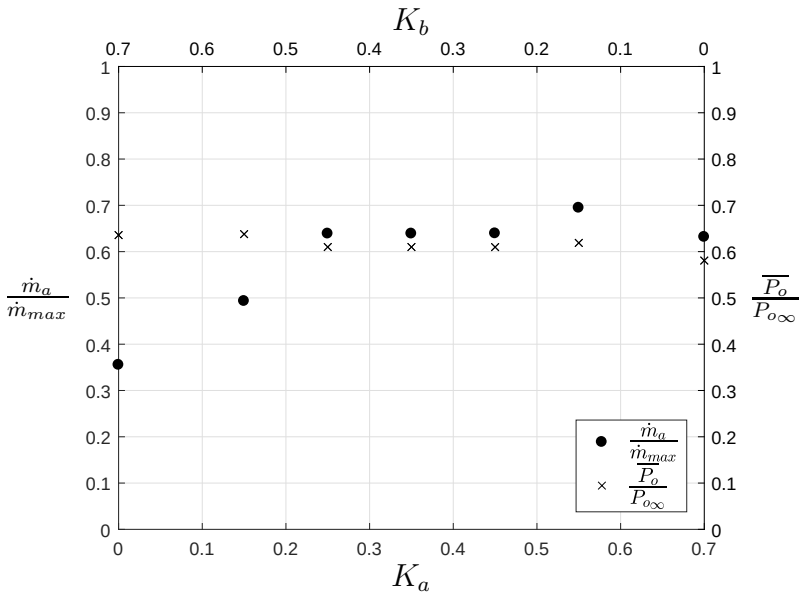

Figure 4.5: Effect of varying weights (K_a&K_b) on normalized objectives at M_∞ = 2.5 (K_c=K_d=K_e=0.1).

These two objectives, therefore, are not directly competitive with each other for most weight settings of K_a and K_b. In fact, other than for very low $K_a < 0.25$ ($K_b > 0.45$) the air mass flow is proportional to the total pressure. The relationship between air mass flow and total pressure drop is illustrated in Fig. 4.6 and Eq.(4.2) [36].

$$\dot{m}_a = \sqrt{\frac{\gamma}{R_{air}T_o}} \left(\int_{r=r_{CB}}^{r=a} M_{x1} A_{EI} P_{o1} \left(\frac{2}{2+(\gamma-1)M_{x1}^2} \right)^{\frac{\gamma+1}{2(\gamma-1)}} dA \right) \tag{4.2}$$

The air mass flow is also calculated for the condition where the mass flow rate is choked using Eq.(4.3) [36]. The minimum mass flow rate between Eq.(4.2) & Eq.(4.3) is used as the $\dot{m}_a$ objective. However, none of the individuals in Table 4.2, Fig. 4.4 & Fig. 4.5 are in a choked condition.

$$\dot{m}_a^* = \sqrt{\frac{\gamma}{R_{air}T_o}} \left(A_2 \overline{P_o} \left(\frac{2}{2+(\gamma-1)} \right)^{\frac{\gamma+1}{2(\gamma-1)}} \right) \tag{4.3}$$

As described in section 2.3.2.2, the air mass flow in Eq.(4.2) is integrated along the

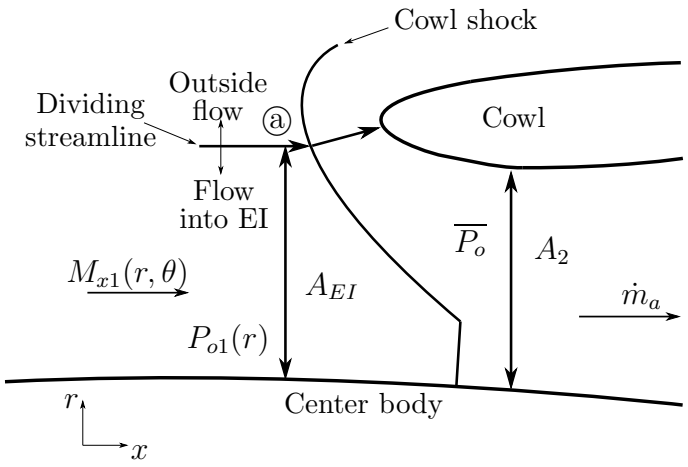

Figure 4.6: EI cross section for air mass flow rate calculation variables [36].

area A_{EI}, which is below the dividing streamline, shown in Fig. 4.6. Since the area A_{EI} is integrated ($dA = rdrd\theta$) around the center body, it is affected by the shape of all three EI components (center body, fairings & cowl). Equation (4.2) shows that air mass flow is proportional to both the inlet area A_{EI} and the total pressure after the fairing shock P_{o1}, but before the cowl shock. The total pressure recovery objective $\overline{P_o}$ is the resulting average total pressure behind the cowl shock. Therefore, improvements in the average total pressure recovery after the fairing shock $\overline{P_{o1}}$ can improve both $\dot{m}_a$ and $\overline{P_o}$, for a similar area A_{EI} and cowl shock strength. The values of A_{EI} and $\overline{P_{o1}}$ are listed in Table 4.3 along with the $\dot{m}_a$ and $\overline{P_o}$ objectives.

Between Points ③ & ⑦ ($K_a \geq$0.25) the area A_{EI} only varies between 18-19.4 m^2, however, at Point ② (K_a=0.15) this rapidly decreases to 15.2 m^2 and again to 11.8 m^2 at Point ① (K_a=0). At these points ① & ② the value of $\overline{P_{o1}}$ also decreases, while $\overline{P_o}$ increases. This indicates that the cowl shock for these two geometries has become much weaker (as A_{EI} is much lower) than for the remaining points. Thus, below K_a=0.25 the reduction in area dominates the air mass flow objective, but as the area A_{EI} begins to stabilize after K_a=0.25 the air mass flow is improved by both $\overline{P_{o1}}$ and A_{EI} improvements.

Table 4.3: Area A_{EI} and total pressure $\overline{P_{o1}}$ change with weights K_a & K_b and objectives of f^k_{best} for M_∞=2.5 (K_c=K_d=K_e=0.1)

Point	K_a	K_b	A_{EI} (m^2)	$\overline{P_{o1}}$ (kPa)	$\dot{m}_a$ (kg/s)	$\overline{P_o}$ (kPa)
1	0	0.7	11.83	99.36	872.14	74.48
2	0.15	0.55	15.15	99.18	1210.6	74.72
3	0.25	0.45	18.01	104.73	1568.3	71.46
4	0.35	0.35	18.01	104.73	1568.3	71.46
5	0.45	0.25	18.04	104.70	1569.5	71.44
6	0.55	0.15	19.40	106.03	1705.3	72.50
7	0.7	0	19.17	105.3	1550.7	68.04

These two objectives, therefore, are not suitable for demonstrating the trade-off of the Pareto front due to their positive correlation for most weight settings. The trade-off must occur between two or more objectives which are competitive with each other. Thus, another set of weights must be selected in order to observe a more complete Pareto front and objective trade off. The following section will evaluate using K_a and K_c as the trade off objectives.

4.2.1.2 K_a vs K_c Pareto front

The air mass flow is considered to be a primary objective, due to the ramjet air breathing mode requirements. The shear layer area objective L_{arc} is also a concern for the ejector mode. As was seen in Fig. 2.17, of subsection 2.3.2.1, it is possible to have a large frontal area A_{in} and a large L_{arc}, at the expense of increased turn angle objective ϕ. This effectively becomes a three-way trade-off (for the rocket path) between A_{in}, L_{arc} and ϕ, as both A_{in} and L_{arc} are desired to be maximized, while ϕ is to be minimized.

The inlet area A_{in} represents the frontal area of the rocket path only, which only considers the area between the rocket clovers (refer to Fig. 2.17)). As shown in Fig. 2.13 in subsection 2.3.1, the maximum chord width of the fairings for the external geometry follows the radial profile of the rocket clovers. This means that as the clovers increase in frontal area (A_{in} reduced), the width of the fairings also increases proportionally. The exchange inlet frontal area, however, is also affected by the shape of both the center body and cowl, in addition to the fairings.

The air mass flow objective $\dot{m}_a$ is proportional to the external geometry inlet area below the dividing streamline A_{EI} (refer to Fig. 4.6 & Eq.(4.2)). This EI inlet area is directly affected by the opening between the fairings, in addition to the center body and cowl shapes. The opening between the fairings is proportional to the area between the clovers A_{in}. Therefore, A_{in} indirectly affects $\dot{m}_a$, by affecting the value of A_{EI}.

The two objectives $\dot{m}_a$ and L_{arc}, therefore, can become competitive with each other through the turn angle ϕ in a similar manner as A_{in} and L_{arc} can for the rocket path, if the weight K_c is increased. In addition, as shown in Fig. 4.5, $\dot{m}_a$ and $\overline{P_o}$ show a positive correlation for higher values of K_a. A Pareto front trade off between $\dot{m}_a$ and ϕ will, thus, also indirectly involve $\overline{P_o}$ and L_{arc}.

To observe the trade off between the objectives $\dot{m}_a$ and ϕ, the weights of K_a and K_c will be varied (both sum to 0.7) to develop a Pareto front, in the $\frac{\dot{m}_a}{\dot{m}_{max}}$ and $1 - \frac{\phi}{90}$ objective space hyperplane. Varying the weight K_a ensures that the primary objective of air mass flow is observed in the Pareto front. As was shown in the previous section, each new weight setting will correspond to a new most fit individual f^k_{best} on the Pareto front. The weights and resulting objectives are shown in Table 4.4, while the Pareto front for the $\frac{\dot{m}_a}{\dot{m}_{max}}$ and $1 - \frac{\phi}{90}$ objectives is shown in Fig. 4.7.

Table 4.4: Weights K_a & K_c and objectives of f^k_{best} for M_∞=2.5 (K_b=K_d=K_e=0.1)

Point	K_a	K_c	$\dot{m}_a$ (kg/s)	$\overline{P_o}$ (kPa)	ϕ $(^\circ)$	L_{arc} (m)	$\frac{d^2\widetilde{r}}{d\widetilde{z}^2}$
1	0.15	0.55	908.43	55.08	**1.02**	12.75	**0.01479**
2	0.25	0.45	964.2	54.71	**1.02**	12.75	0.01479
3	0.35	0.35	1185.7	61.94	4.64	10.39	0.01583
4	0.45	0.25	1284.6	69.39	6.08	8.30	0.05211
5	0.47	0.23	1367.9	70.10	15.29	10.10	0.05063
6	0.50	0.20	1367.9	70.10	15.29	10.10	0.05063
7	0.52	0.18	**1684.0**	**72.72**	39.64	13.98	0.23954
8	0.55	0.15	1644.6	70.71	47.19	16.94	0.22755
9	0.58	0.12	1632.3	67.17	51.96	19.10	0.18734
10	0.65	0.05	1566.2	71.47	56.71	**19.46**	0.12564

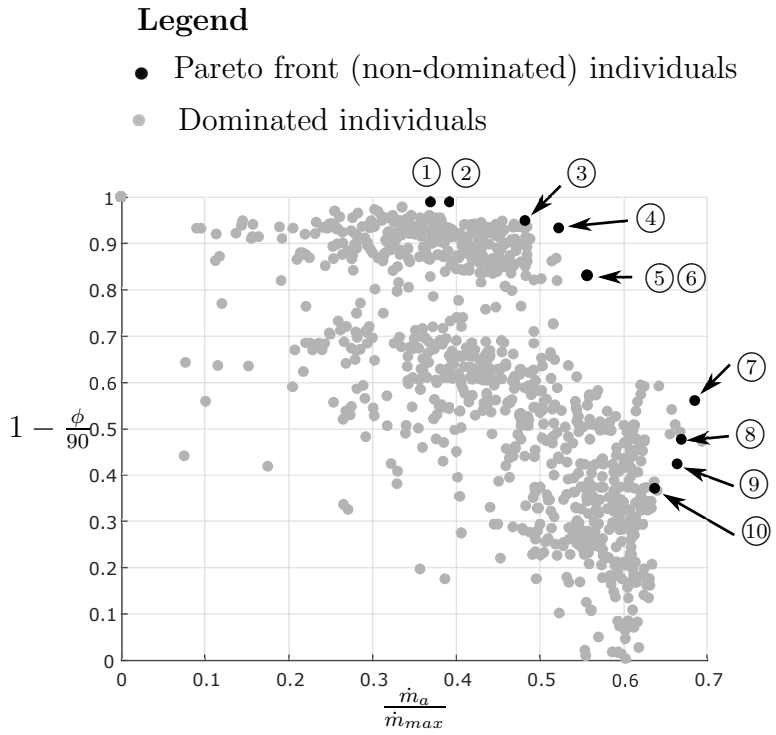

Figure 4.7: Pareto front for K_a and K_c objectives at M_∞=2.5 (K_b=K_d=K_e=0.1).

As Fig. 4.7 indicates, there are two regions in the Pareto front. Initially, the turn angle objective $1-\frac{\phi}{90}$ shows high values for low K_a (high K_c). The turn angle ϕ is to be minimized ($1-\frac{\phi}{90}$ maximized). As K_a increases, however, the turn angle objective $1-\frac{\phi}{90}$ begins to decrease (ϕ increases). This occurs slowly until the value of $0.47 \geq K_a \leq 0.5$ (Points ⑤ & ⑥), beyond which there is a sudden change in the Pareto front shape. This is shown in Table 4.4 as ϕ increases from 15.29° to 39.64° between points ⑥ & ⑦. This sudden change is the result of the turn angle becoming competitive with the arc length L_{arc}, as the turn angle weight K_c is reduced to a critical point relative to both the K_a and $K_d = 0.1$ (arc weight) values. The competition between L_{arc} and ϕ with an increasing K_a (decreasing K_c) value is illustrated in Fig. 4.8 for the rocket path. (Recall A_{in} directly affects A_{EI} which is proportional to $\dot{m}_a$ in Eq.(4.2)).

As shown in Fig. 4.8(a) and Fig. 4.8(b) the turn angle is relatively small, which forces a near triangular profile of the rocket clovers. As K_a is increased, this clover frontal profile is forced to become narrower to increase $\dot{m}_a{=}f(A_{EI}) \approx f(A_{in})$, which in turn decreases the arc length L_{arc} (increasing A_{in}). At $K_a = 0.47/0.50$, however, the turn angle begins to increase due to the decreasing weight of K_c, until it rapidly transitions from Point ⑥ to Point ⑦ (corresponding to $K_a = 0.5$ and $K_a = 0.52$) in Fig. 4.8(c) and Fig. 4.8(d). This sudden change in the Pareto front objectives is best illustrated in a plot of the weights and objectives shown in Fig. 4.9.

From Fig. 4.9(a), the peak values of both $\dot{m}_a$ and $\overline{P_o}$ occur around $K_a = 0.52$, right after the change in the Pareto front (from Point ⑥ to ⑦). After $K_a = 0.52$ the mass flow begins to decrease as it begins competing with L_{arc}. The turn angle ϕ strongly competes with L_{arc} after $K_a = 0.52$, as shown by their negative correlation in Fig. 4.9(b). The two points of interest are at K_a=0.50 (⑥) & K_a=0.52 (⑦) as this is where the critical trade-off or compromise is occurring between $\dot{m}_a$ (& correspondingly $\overline{P_o}$), L_{arc} and ϕ. It is also noted that neither of these points are in a choked air mass

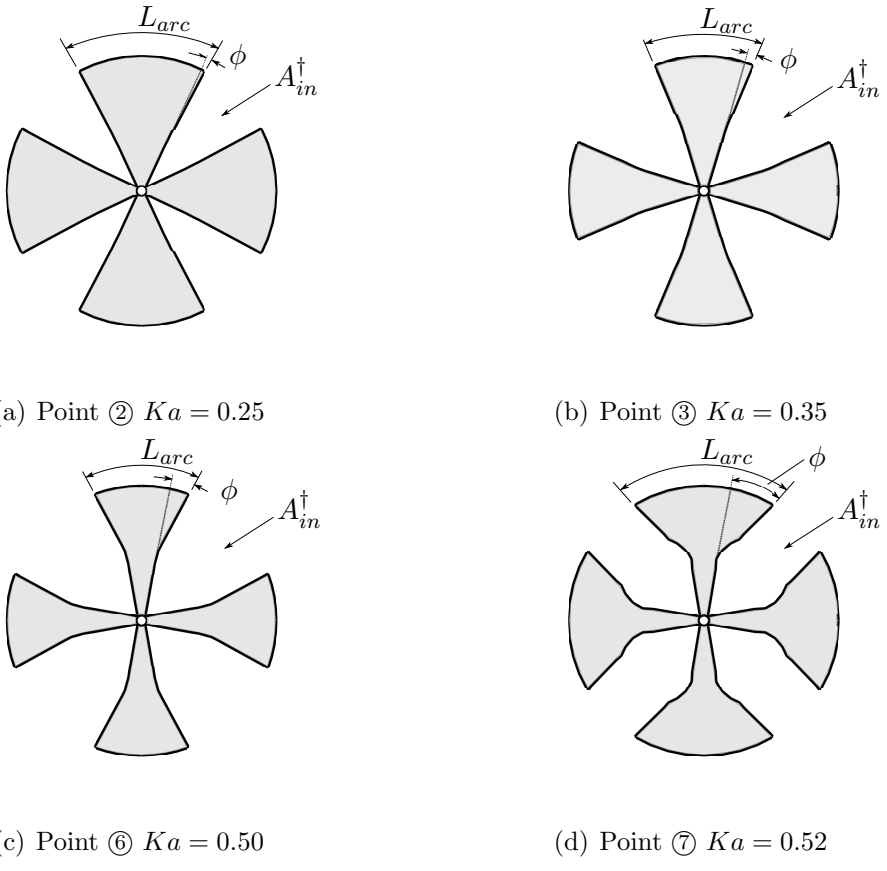

(a) Point ② $Ka = 0.25$

(b) Point ③ $Ka = 0.35$

(c) Point ⑥ $Ka = 0.50$

(d) Point ⑦ $Ka = 0.52$

Figure 4.8: Rocket path frontal area profiles for varying K_a values at M_∞=2.5 (K_b=K_d=K_e=0.1). †Area $A_{EI} \approx f(A_{in})$ is also affected by center body radius & cowl (shock) shape.

flow condition. The changes in the exchange inlet external geometry between these two points (⑥ & ⑦) are illustrated in the images shown in Fig. 4.10 and Fig. 4.11.

The images in Fig. 4.10 and Fig.4.11 appear to show a larger frontal area at Point ⑥ (K_a=0.5) than at Point ⑦ (K_a=0.52). This is true for A_{in}, but not for A_{EI} as the inlet area is also affected by the center body and the shape of the cowl shock & corresponding location of the dividing streamline shown in Fig. 4.6. The area A_{EI} increases from 16.1 m^2 at Point ⑥ to 19.1 m^2 at Point ⑦. The improvement in A_{EI} is due to the indirect affect the rocket area A_R has on the area of the leading edge of the cowl A_{LE} (see Fig. 2.12). As described in subsection 2.3.1, the area at leading edge of the cowl A_{LE} is controlled by the gene CR and the area $A_2 \propto A_3 \propto A_R$ (see

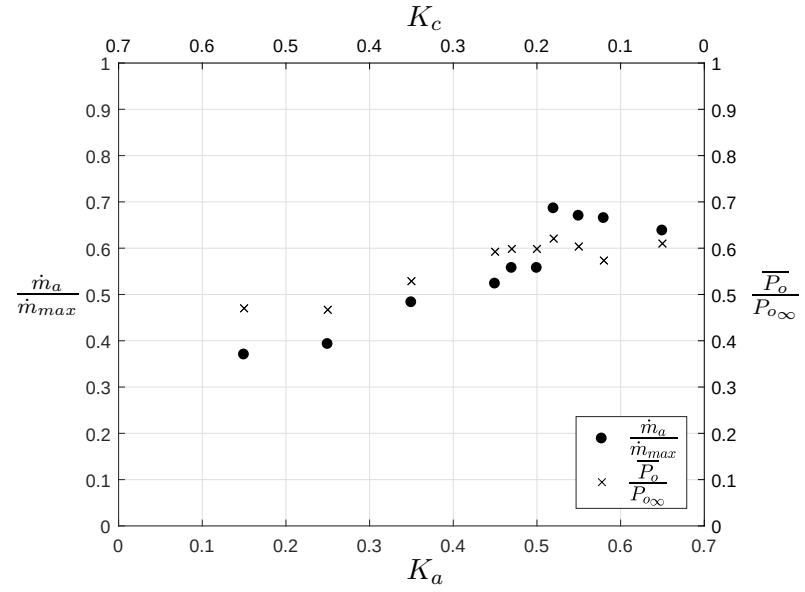

(a) Air mass flow and total pressure recovery objectives.

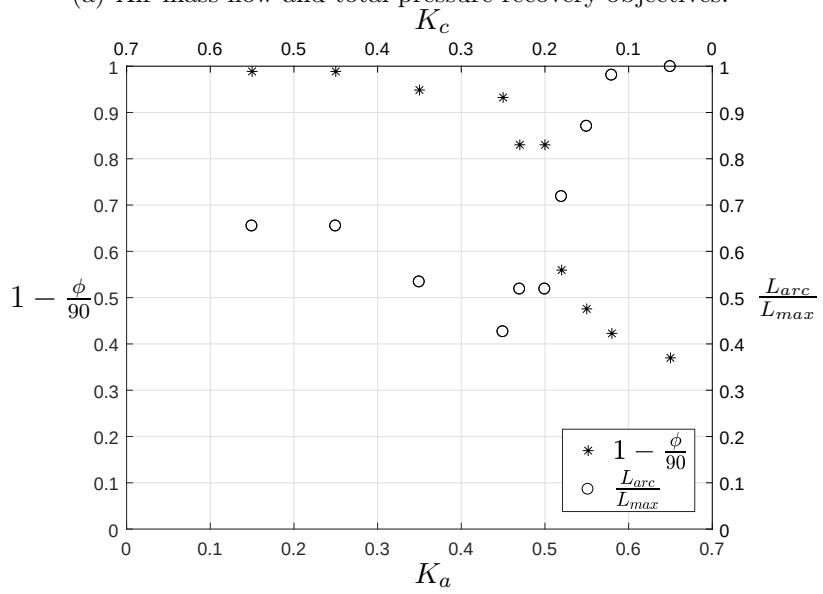

(b) Turn angle and arc length objectives.

Figure 4.9: Effect of varying weights (K_a&K_c) on normalized objectives at M_∞=2.5 (K_b=K_d=K_e=0.1).

Eq.(2.14) and (2.15)). The gene CR is the same (1.4) for the individuals at both points ⑥ and ⑦.

Once the turn angle begins to compromise, then the fairing can maintain a narrower frontal profile (at lower radial locations) to maintain frontal area, while allowing

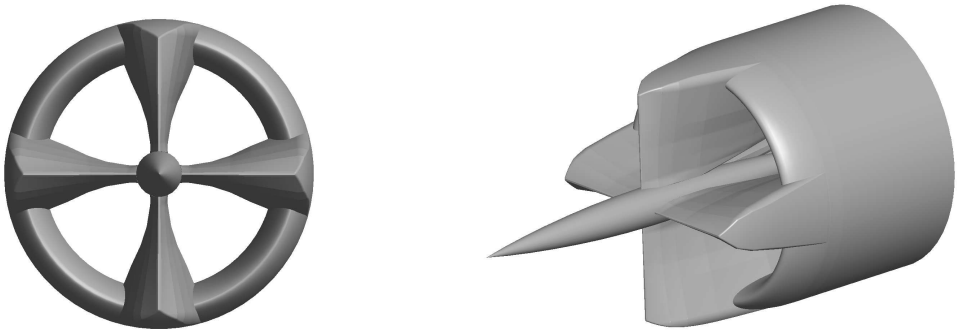

(a) Front view (b) Isometric view

Figure 4.10: External geometry at Point ⑥ K_a=0.50, K_c=0.20 at M_∞=2.5 (K_b=K_d=K_e=0.1).

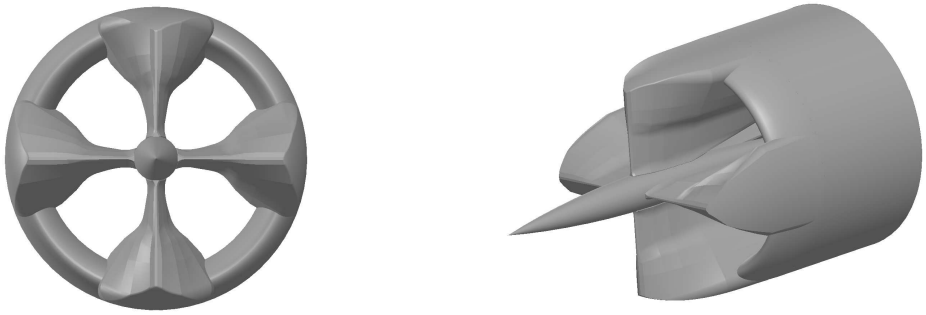

(a) Front view (b) Isometric view

Figure 4.11: External geometry at Point ⑦ K_a=0.52, K_c=0.18 at M_∞=2.5 (K_b=K_d=K_e=0.1).

L_{arc} to increase again. A larger value of L_{arc} can result in a larger A_R value, which is the area slice at the rocket exit plane shown in Fig. 2.9. This in turn increases A_{LE} in Fig. 2.16 via Eq.(2.14), (2.15) and (2.16). The value of the area at the cowl leading edge A_{LE} affects the shape of the cowl shock wave, and the resulting exchange inlet area A_{EI} shown in Fig. 4.6. Therefore, larger values of A_R can improve the frontal area A_{EI} between the cowl and center body. This occurs in the geometries between Point ⑥ and Point ⑦, as A_R increases from $1.88m^2$ to $2.15m^2$. This benefit of increasing A_R, however, is limited by the external geometry creation as the cowl leading

edge area A_{LE} can only be increased so far, as the outer radius of the rocket path is fixed ($r_e = 3.1m$). Thus, increasing L_{arc} beyond Point ⑦ ($K_c = 0.52$) does not show additional benefit, and results in a decreasing area due to further increasing L_{arc} and affecting the frontal area of the fairing. This is due to a resulting wider fairing profile at higher radial locations. Furthermore, in the Pareto front 2D hyperplane of Fig. 4.7 and again in Fig. 4.9, the optimal trade-off occurs at the points which show the largest improvement on one axis at the expense of another. In this case, in Fig. 4.7, the two points of interest (⑥ & ⑦) in this front correspond to weights $K_a = 0.5$ and $K_a = 0.52$. The difference in frontal area and cowl shape between these two points is further illustrated in Fig. 4.12.

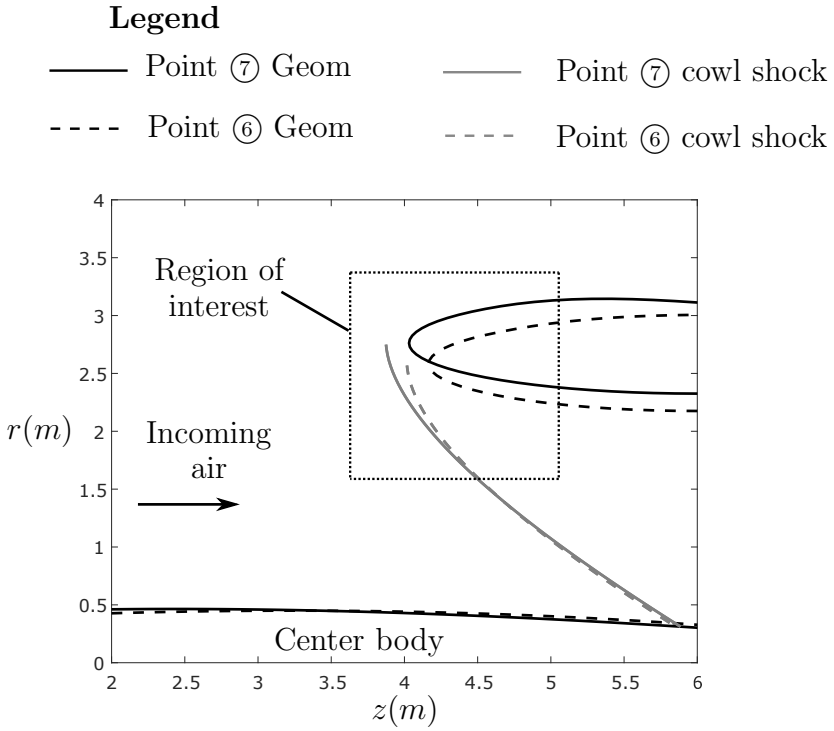

Figure 4.12: Side profile for Point ⑥ (K_a=0.50) & ⑦ (K_a=0.52) at M_∞=2.5 (K_b=K_d=K_e=0.1)

The shape of the cowls shown in Fig. 4.12 affects the cowl shock wave, which in turn affects the total pressure drop across it. The external geometry of Point ⑥ shows

that near the cowl its corresponding shock wave has a sharper turn relative to the flow direction. The more normal the shock wave is to the flow direction the stronger the shock wave is, and the larger the total pressure drop across it will be. The optimal choice based on weight selection is the peak at $K_a = 0.52$, since it corresponds with the highest $\dot{m}_a$ and $\overline{P_o}$ values, and an increase of 23.1% and 3.73% respectively over $K_a = 0.5$. An averaged total pressure comparison is shown in Table 4.5.

Table 4.5: Avg. total pressure (kPa) behind shocks for Point ⑥ (K_a=0.50) & ⑦ (K_a=0.52) at M_∞=2.5 (K_b=K_d=K_e=0.1).

	after center body shock (kPa)	after fairing shocks ($\overline{P_{o1}}$) (kPa)	after cowl shock ($\overline{P_o}$) (kPa)
Point ⑥	117.08	104.36	70.10
Point ⑦	117.08	105.89	72.72
% change	-	+1.46	+3.74

The results in Table 4.5 show that the individual at Point ⑦ has a higher average total pressure after the fairing shock ($\overline{P_{o1}}$). This higher $\overline{P_{o1}}$ value, in addition to its larger area A_{EI}, gives a higher $\dot{m}_a$ via Eq.(4.2). Table 4.5 also shows its average total pressure recovery objective ($\overline{P_o}$) is larger than the individual at Point ⑥. Therefore, if the rocket turn angle of $\phi = 39.64°$ (Table 4.4) is considered to be acceptable, then the individual at Point ⑦ is considered to be the optimal individual due to its higher $\dot{m}_a$ and $\overline{P_o}$ objectives. If a lower turn angle $\phi = 15.29°$ (Table 4.4) is required then the individual at Point ⑥ would be considered the optimal individual. For this work the individual at Point ⑦ (shown in Fig. 4.11) is selected as the optimal individual for its higher $\dot{m}_a$ and $\overline{P_o}$ objectives (the $\frac{d^2\tilde{r}}{d\tilde{z}^2}$ objective exists only to weed out geometries with poor radial contours).

These results demonstrate the behaviour of varying weights, and selection for the

optimal exchange inlet geometry at a single Mach number (M_∞=2.5). However, in order to provide more information about optimization over the full flight range, two other Mach numbers will be selected to determine additional optimal geometries. These three geometries will be compared over the supersonic flight range profile to evaluate their overall performance at off-design conditions.

4.2.2 Mach 1.5 and 3.5 Results

Using the same procedure as subsection 4.2.1.2, the weights of K_a & K_c are varied (both sum to 0.7) at the freestream Mach number M_∞=1.5 and then again at M_∞=3.5. The remaining weights stay at K_b=K_d=K_e=0.1. The results of varying the weights K_a and K_c at M_∞=1.5 are shown in Table 4.6, with the Pareto front in Fig. 4.13.

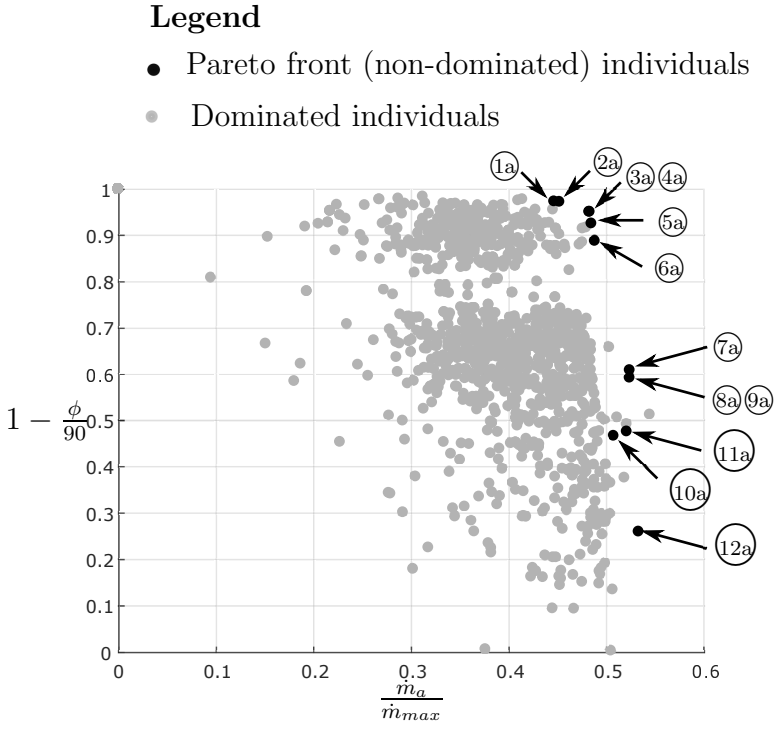

Figure 4.13: Pareto front for K_a and K_c objectives at M_∞=1.5 (K_b=K_d=K_e=0.1).

Table 4.6: Weights K_a & K_c and objectives of f^k_{best} for M_∞=1.5 (K_b=K_d=K_e=0.1)

Point	K_a	K_c	$\dot{m}_a$ (kg/s)	$\overline{P_o}$ (kPa)	ϕ $(^\circ)$	L_{arc} (m)	$\frac{d^2\widetilde{r}}{d\widetilde{z}^2}$
1a	0.25	0.45	1826.1	65.70	**2.39**	13.78	0.01464
2a	0.35	0.35	1848.5	65.75	2.48	13.44	0.01462
3a	0.45	0.25	1973.0	65.75	4.41	13.77	**0.01375**
4a	0.5	0.2	1975.3	66.01	4.41	12.41	0.01462
5a	0.52	0.18	1982.5	65.82	6.68	13.42	0.01425
6a	0.55	0.15	1996.6	65.83	10.08	13.76	0.01430
7a	0.58	0.12	2143.0	66.02	35.20	18.73	0.03484
8a	0.6	0.1	2142.6	66.02	36.68	19.10	0.03226
9a	0.62	0.08	2142.6	66.02	36.68	19.10	0.03226
10a	0.65	0.05	2075.5	65.90	47.97	**19.46**	0.01827
11a	0.68	0.02	2130.5	66.26	47.13	**19.46**	0.04748
12a	0.7	0	**2180.2**	**66.96**	66.6	18.73	0.05143

As with the results from the previous section there is a trade-off point where the turn angle jumps from $\phi = 10.08^\circ$ at Point (6a) ($K_a = 0.55$) to $\phi = 35.2^\circ$ at Point (7a) ($K_a = 0.58$) in Fig. 4.13. The air mass flow increases from 1996.6 kg/s to 2143 kg/s respectively. This is illustrated in the weight vs objective plots for M_∞=1.5 shown in Fig. 4.14.

The Fig. 4.14(a) shows a similar but less pronounced profile to that which was observed for $\dot{m}_a$ and $\overline{P_o}$ shown in Fig. 4.9(a). The normalized total pressure recovery shows little variation over the range, however, the normalized air mass flow shows a jump between $K_a = 0.55$ ($K_c = 0.15$) and $K_a = 0.58$ ($K_c = 0.12$). The increase in $\dot{m}_a$ comes at the expense of ϕ, as indicated by its drop between $K_a = 0.55$ and $K_a = 0.58$ in Fig. 4.14(b). This transition also occurs at the same point where ϕ

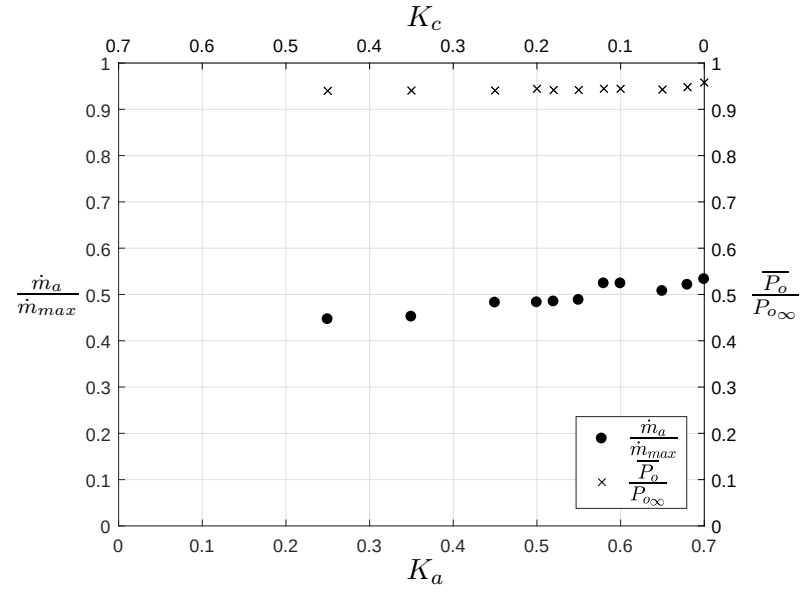

(a) Air mass flow and total pressure recovery objectives.

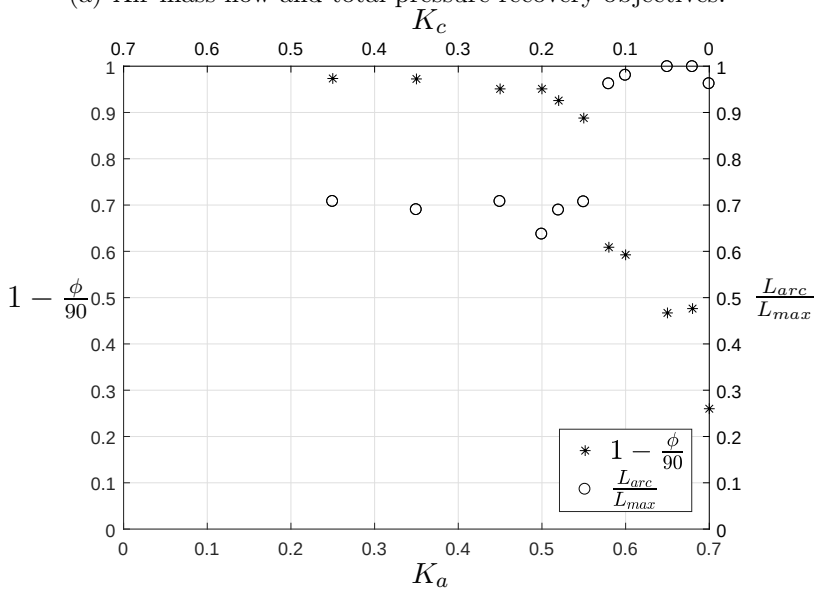

(b) Turn angle and arc length objectives.

Figure 4.14: Effect of varying weights (K_a & K_c) on normalized objectives at M_∞=1.5 (K_b=K_d=K_e=0.1).

and L_{arc} also begin to become competitive with each other as shown in Fig. 4.14(b) . As with Fig. 4.9, increasing K_a beyond 0.58 does not provide additional gain in $\dot{m}_a$, rather it serves to reduce the value of K_c so that ϕ competes mainly with L_{arc}. The exception to this is at K_a=0.7 in Fig. 4.14 (Point (12a) in Table 4.6), where

the mass flow increases to 2180.2 ks/s or 1.74% higher than the value at K_a=0.58 (Point ⑦ₐ in Table 4.6). This however comes at a significant increase in the turn angle from $\phi = 35.2°$ at K_a=0.58 to $\phi = 66.6°$ at K_a=0.7, or an 89% increase. This represents a poor trade-off (at K_a=0.7) between $\dot{m}_a$ and ϕ, as excessively large turn angles can lead to excessive circumferential expansion and shock waves in the rocket path as discussed in subsection 2.3.2.1. The selection of the most fit individual for M_∞=1.5, therefore, is selected to be at the weight setting of K_a=0.58 as it provides a relatively large value of $\dot{m}_a$, while not excessively compromising the turn angle ϕ. This individual is shown in Fig. 4.15.

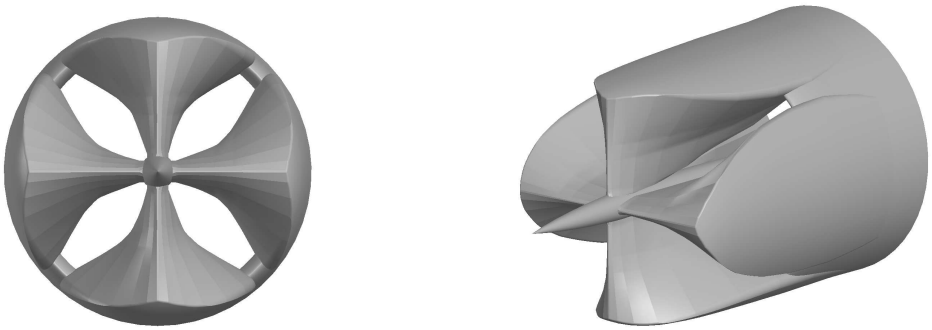

(a) Front view (b) Isometric view

Figure 4.15: External geometry at Point ⑦ₐ K_a=0.58, K_c=0.12 at M_∞=1.5 (K_b=K_d=K_e=0.1).

The optimal individual (geometry) at M_∞=1.5 in Fig. 4.15 shows a much wider fairing profile than the optimal individual at M_∞=2.5. This results in a much stronger fairing shock in the M_∞=1.5 optimal individual as indicated in Table 4.7.

The average local Mach number $\overline{M_1}$ after the fairing shock is subsonic, indicating the fairing shock has a large region where the bow shock is more normal to the flow, refer to Fig. 1.8. The subsonic flow then does not generate a cowl shock and subsequently no further decrease in the total pressure. The flow through this individual geometry is also choked, meaning the flow at A_2 (refer to Fig. 4.6) is sonic

Table 4.7: Avg. total pressure and local Mach number of f^k_{best} at K_a=0.58 for M_∞=1.5 (K_b=K_d=K_e=0.1)

	After center body shock	After fairing shock ($\overline{P_{o1}}$, $\overline{M_1}$)	After cowl ($\overline{P_o}$, $\overline{M_2}$)
Total pressure (kPa)	69.90	66.02	66.02
Local ($\overline{M}$)	1.47	0.92	0.92

(M=1) and, therefore, calculated by Eq. (4.3) using $\overline{P_o}$ which is the same as $\overline{P_{o1}}$. Since there is no cowl shock, there is no further decrease in total pressure after the fairing as isentropic flow is assumed between shocks. Thus, at this freestream Mach number (M_∞=1.5) having a strong fairing shock appears to be beneficial as it causes subsonic flow into the cowl and a maximum flow which is choked.

With an optimal individual selected for M_∞=1.5 (Fig. 4.15) and at M_∞=2.5 (Fig. 4.11), the same proceedure is repeated at M_∞=3.5. The weights K_a and K_c are varied, while the remaining weights stay at K_b=K_d=K_e=0.1. The results of varying the weights K_a and K_c at M_∞=3.5 are shown in Table 4.8 and Fig. 4.16.

As Table 4.8 and Fig. 4.16 show, there are two jumps in air mass flow and the corresponding turn angle. The first occurs between Point ⑤b (K_a=0.5) and Points ⑥b/⑦b (K_a=0.52/0.55). Between these points, the air mass flow increases from 1138.5 kg/s to 1272.5 kg/s, while the turn angle increases from $\phi = 6.2°$ to $\phi = 36.61°$. The total pressure recovery also sees a corresponding jump from 68.46 kPa to 82.2 kPa. The turn angle $\phi = 36.61°$ is also in a similar range to the geometries selected at the other two Mach numbers. This jump in the objective values can also be seen in Fig. 4.17.

Both Table 4.8 and Fig. 4.17 also show there is a second jump in $\dot{m}_a$ and ϕ, however, from Points ⑥b/⑦b (K_a=0.52/0.55) to Point ⑧b (K_a=0.58). This second jump shows an increase in $\dot{m}_a$ to 1354.6 kg/s or 6.5%, while the turn angle jumps

Table 4.8: Weights K_a & K_c and objectives of f^k_{best} for M_∞=3.5 (K_b=K_d=K_e=0.1)

Point	K_a	K_c	$\dot{m}_a$ (kg/s)	$\overline{P_o}$ (kPa)	ϕ $(^\circ)$	L_{arc} (m)	$\frac{d^2\widetilde{r}}{d\widetilde{z}^2}$
1b	0.15	0.55	1054.9	67.19	1.45	13.10	**0.01458**
2b	0.25	0.45	961.84	64.32	**1.18**	14.11	0.01542
3b	0.35	0.35	961.84	64.32	**1.18**	14.11	0.01542
4b	0.45	0.25	1069.0	68.68	2.48	13.44	0.01462
5b	0.5	0.2	1138.5	68.46	6.20	12.73	0.01468
6b	0.52	0.18	1272.5	**82.20**	36.61	18.73	0.01657
7b	0.55	0.15	1272.5	**82.20**	36.61	18.73	0.01657
8b	0.58	0.12	**1354.6**	79.06	66.65	**19.46**	0.04539
9b	0.65	0.05	**1354.6**	79.06	66.65	**19.46**	0.04539
10b	0.7	0	1347.0	78.94	66.65	**19.46**	0.04539

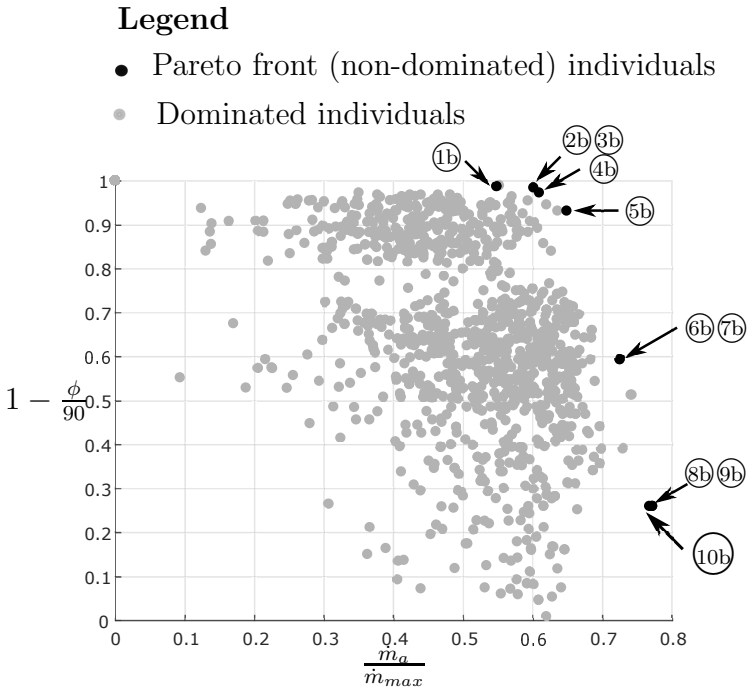

Figure 4.16: Pareto front for K_a and K_c objectives at M_∞=3.5 (K_b=K_d=K_e=0.1).

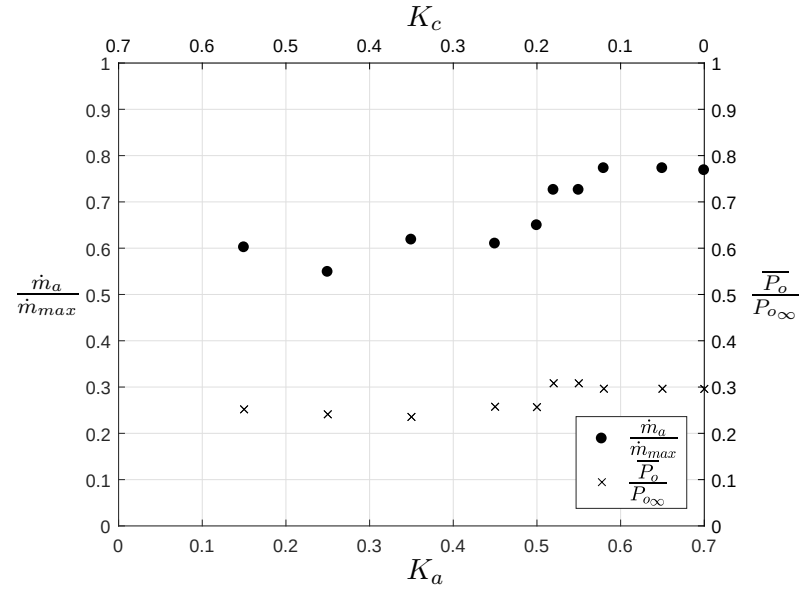

(a) Air mass flow and total pressure recovery objectives.

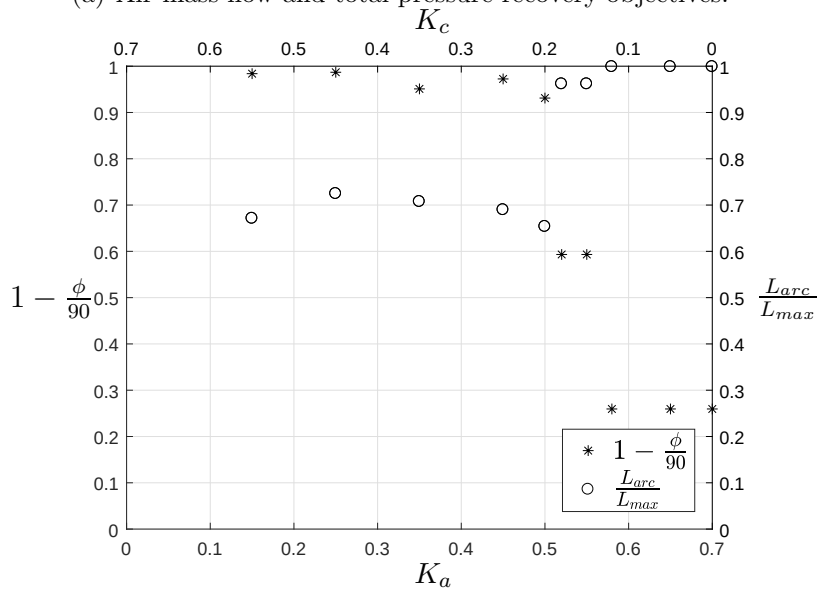

(b) Turn angle and arc length objectives.

Figure 4.17: Effect of varying weights (K_a & K_c) on normalized objectives at M_∞=3.5 (K_b=K_d=K_e=0.1).

to $\phi = 66.65°$ or an 82% increase. As with the M_∞=1.5 case, this represents a poor trade-off as the turn angle is significantly increased for a minimal increase in air mass flow. In addition, the total pressure between Points ⑥ᵇ/⑦ᵇ (K_a=0.52/0.55) and Point ⑧ᵇ (K_a=0.58) actually shows a slight decrease from 82.2 kPa to 79.06 kPa. Therefore,

the individual at Points ⑥b/⑦b (K_a=0.52/0.55) is selected as the most optimal. This individual is shown in Fig. 4.18.

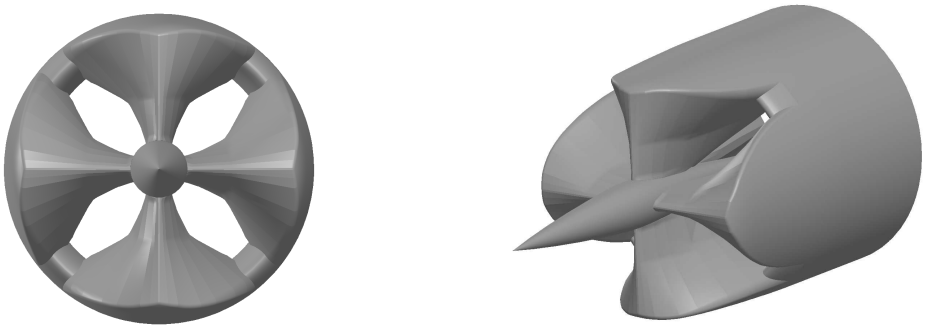

(a) Front view (b) Isometric view

Figure 4.18: External geometry at Point ⑦b K_a=0.55, K_c=0.15 at M_∞=3.5 (K_b=K_d=K_e=0.1).

Figure 4.18 shows that the optimal individual at M_∞=3.5 again shows a wider fairing profile than the optimal individual at M_∞=2.5. Unlike the individual at M_∞=1.5, however, this individual at M_∞=3.5 is not in a choked condition and the flow after the fairing remains supersonic at $\overline{M_1}$=1.52.

In order to accurately compare all three geometries, they will need to be investigated at similar Mach numbers in their off-design conditions. In addition, each one of these optimal geometries (M=1.5, 2.5 & 3.5) is a fixed geometry, however, by examining their off-design performance the benefit of using a variable geometry can be examined. This is the focus of the next section.

4.3 Variable Geometry and Off-Design Performance Comparison

A side profile wire frame cross section of each of the three optimal selected geometries from Fig. 4.11(M_∞=2.5), 4.15 (M_∞=1.5) & 4.18 (M_∞=3.5) is shown in Fig. 4.19.

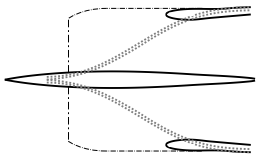

(a) $M_\infty = 1.5$ ($K_a = 0.58$)

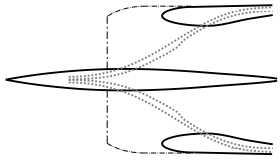

(b) $M_\infty = 2.5$ ($K_a = 0.52$)

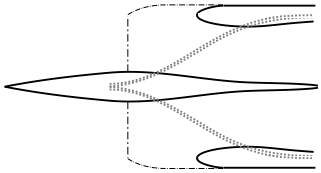

(c) $M_\infty = 3.5$ ($K_a = 0.55$)

Figure 4.19: Cross sections of optimized designs for $M_\infty = 1.5$, 2.5 & 3.5.

Each of the cross sections in Fig. 4.19 show a general trend of increasing center body (and cowl) thickness. The question of which design is best, however, will vary with freestream Mach number since each one is only optimized at a single flight Mach number. Therefore, the overall flight performance of each design must be viewed over the supersonic flight range. This is illustrated for both the air mass flow and total pressure recovery objectives in Fig. 4.20 and Fig. 4.21 respectively.

The results of Fig. 4.20 and Fig. 4.21 show that even though the M_∞=1.5 and $M_\infty = 3.5$ optimal geometry designs have better values of $\frac{\dot{m}_a}{\dot{m}_{max}}$ near their respective Mach numbers, those improvements rapidly diminish over the flight range. The optimal design at M_∞=1.5 shows higher peak $\dot{m}_a$ (11% @ M_∞=1.9) and $\overline{P_o}$ (14% @ M_∞=1.9) objectives vs the M_∞=2.5 optimal design at freestream Mach numbers $M_\infty \leq 2.0$. The optimal design at M_∞=3.5 shows higher peak $\dot{m}_a$ (12% @ M_∞=3.7) and $\overline{P_o}$ (19% @ M_∞=3.7) objectives vs the M_∞=2.5 optimal design at freestream Mach number ranges of $3.2 \leq M_\infty \leq 4$ and $3.5 \leq M_\infty \leq 4$ respectively.

Both the M_∞=1.5 optimal design and M_∞=2.5 optimal design experience choked flow at $M_\infty \leq 2.0$ (the M_∞=3.5 could not be evaluated below M_∞=2.3 due the

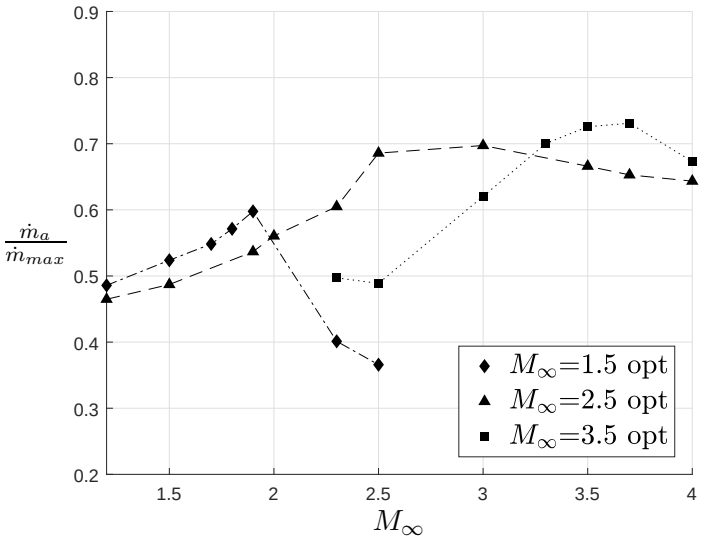

Figure 4.20: Performance of different geometries over flight range for $\dot{m}_a$.

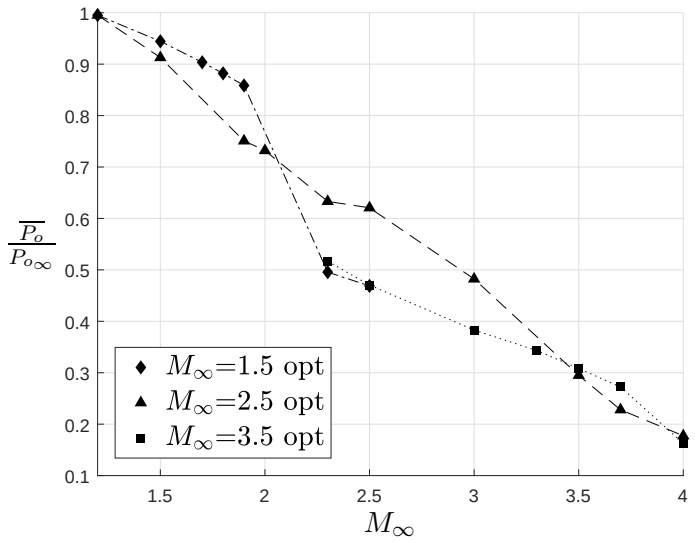

Figure 4.21: Performance of different geometries over flight range for $\overline{P_o}$.

assumed shock structure of the estimation code). However, the M_∞=2.5 optimal design has a weaker fairing shock and therefore a cowl shock at the off-design condition M_∞=1.5 vs the M_∞=1.5 optimal design. As a result, the flow in the M_∞=2.5 optimal design passes through two bow shocks (fairing & cowl), whereas in the M_∞=1.5

optimal design the flow only passes through the fairing shock as the cowl shock does not exist. This results in lower total pressure objective for the M_∞=2.5 optimal design of $\overline{P_o}$=63.81 kPa at the off-design condition M_∞=1.5, vs the M_∞=1.5 optimal design from Table 4.7 $\overline{P_o}$=66.02 kPa (recall that for choked flow Eq.(4.3) is used to calculate $\dot{m}_a$ using the total pressure after the cowl $\overline{P_o}$). Therefore, the M_∞=2.5 optimal design also has a lower $\dot{m}_a$ than the M_∞=1.5 optimal design at this off-design condition (M_∞=1.5). After a freestream Mach number of M_∞=2, however, the flow is no longer choked and the fairing shock in the M_∞=1.5 optimal design can no longer reduce the flow to subsonic speeds. Therefore, a cowl shock forms as the freestream Mach number increases, resulting in a rapid drop off in both $\dot{m}_a$ and $\overline{P_o}$ for the M_∞=1.5 optimal design, as seen in both Fig. 4.20 and Fig. 4.21.

At the freestream Mach number of M_∞=3.5, neither the M_∞=3.5 optimal design or the M_∞=2.5 optimal design is in a choked condition (the M_∞=1.5 optimal design could not be evaluated above M_∞=2.5 due the cowl shock passing beyond the exit Plane 3). A comparison of their Mach numbers and total pressure at the freestream Mach number of M_∞=3.5 is shown in Table 4.9.

Table 4.9: Avg. total pressure and local Mach number of M_∞=2.5 (off-design) and M_∞=3.5 optimal designs at freestream M_∞=3.5

	After center body shock	After fairing shock ($\overline{P_{o1}}$, $\overline{M_1}$)	After cowl ($\overline{P_o}$, $\overline{M_2}$)
Total pressure (kPa)			
M_∞=2.5 opt	265	220.3	78.69
M_∞=3.5 opt	265	152.1	82.20
Local ($\overline{M}$)			
M_∞=2.5 opt	3.22	2.82	1.00
M_∞=3.5 opt	3.21	2.51	1.18

As shown in Table 4.9 the fairing shock for the M_∞=3.5 optimal design is much stronger than for the M_∞=2.5 optimal design (off-design condition) at the freestream M_∞=3.5. This is indicated by the differences in the total pressure and Mach number after the fairings and would be expected given the wider fairing profile of the M_∞=3.5 optimal design. The relative change in Mach number across the fairing and cowl shocks for the M_∞=3.5 optimal design are -22% and -53% respectively, whereas for the M_∞=2.5 optimal design they are -12% and -65% respectively. The weaker fairing shock of the M_∞=2.5 optimal design, however, results in a much stronger cowl shock as indicated by the local average Mach number drop of 2.82 after the fairing to 1.0 after the cowl. The result is a lower $\overline{P_o}$ objective of 78.69 kPa for the M_∞=2.5 optimal design vs 82.2 kPa for the M_∞=3.5 optimal design. It would appear that at higher Mach numbers, having a more even deceleration of the flow through the fairing and cowl shocks is advantageous, rather than weakening one shock and strengthening another.

For a fixed geometry, the optimal design at $M_\infty = 2.5$ shows a more consistent performance over the range considered. It has superior performance at $2.0 \leq M_\infty \leq 3.2$ flight speeds and only under performs in $\dot{m}_a$ by 11-12% and 14-19% in $\overline{P_o}$ over a small range of both high and low Mach numbers (these values are larger than the simulation errors presented in Table 2.2). A variable geometry would have a $\frac{\dot{m}_a}{\dot{m}_{max}}$ and $\frac{\overline{P_o}}{P_{o_\infty}}$ curve that follows the highest curves in Fig. 4.20 and Fig. 4.21, however, the added complexity of achieving such a design would not be worth the relatively small gains over a small flight range.

Based on the off design conditions of Fig. 4.20 and Fig. 4.21, the optimal design at $M_\infty = 2.5$ would appear to be a better choice for a fixed geometry inlet. These results are based on a particular design choice to maximize air mass flow $\dot{m}_a$ and total pressure recovery $\overline{P_o}$, while not selecting designs with excessively large turn angles ϕ. The final design choice for a fixed geometry is the optimal design at M_∞=2.5

(K_a=0.52), shown in Fig. 4.22.

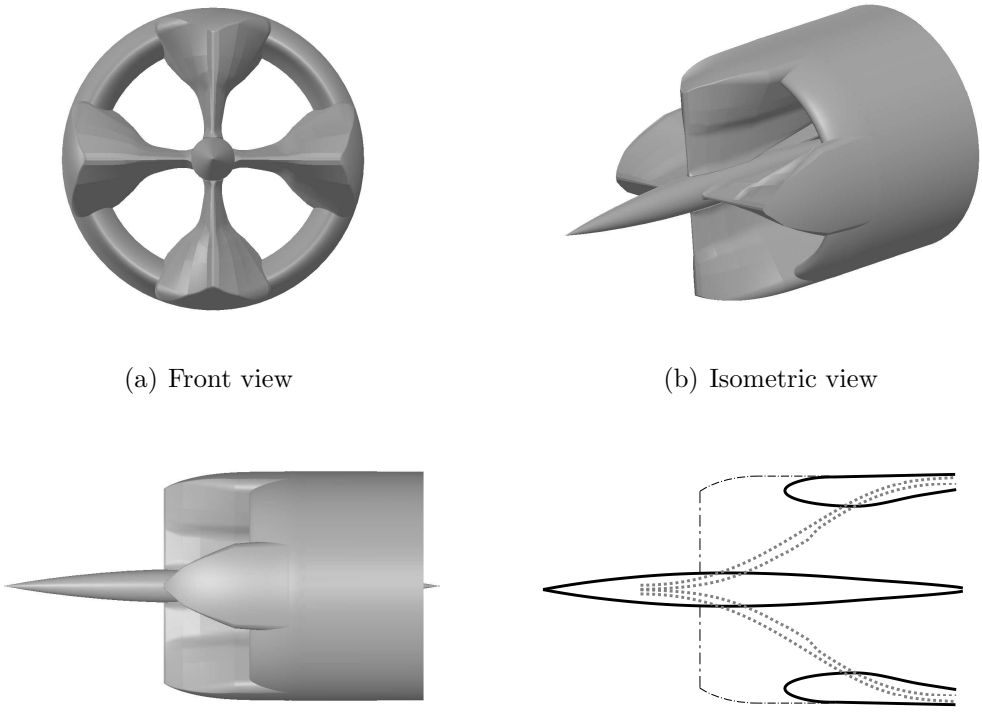

(a) Front view

(b) Isometric view

(c) Side view

(d) Wire frame section

Figure 4.22: Optimal individual for fixed geometry design (selected from M_∞=2.5 design **W**=[0.52,0.18,0.1,0.1,0.1]).

Chapter 5

Conclusion and Recommendations

5.1 Conclusion

The focus of this work is the optimization of a novel rocket based combined cycle (RBCC) inlet over the supersonic flight regime. To facilitate the selection of an optimal design geometry, differential evolution (DE) is used to optimize the design by treating each geometry as an individual in a population. The DE algorithm requires three input parameters of population size (m), differential weight (F) and crossover probability (C_r) to define the population size and determine how it evolves using reproduction and selection. Therefore, using the rocket path as a test case, a method of tuning DE based on how often it finds the best possible individual was established.

The result of tuning the parameters shows that larger population sizes improve performance, as they allowed more individuals to be evaluated with each generation. However, population size could not be arbitrarily increased as it would eventually result in slower performance. The differential weight was shown to have little effect over the range tested, thus, a value close to the recommended default is used. The crossover probability shows improving performance with lower values, which results in individuals crossing over fewer genes during the reproduction process. This leads to a larger population peak diversity and a slower decline diversity as measured by

the variance in the fitness values. This slows the rate of convergence of the algorithm, thus, reducing the likelyhood of premature convergence. The tuning for the exchange inlet also shows no distant local optima, thereby, eliminating the risk of an alternate (local) optimum with a radically different geometry.

Since there are multiple objectives, the Pareto front for this work is multi-dimensional. Therefore, only two weights are varied at time to view the Pareto front in a two-dimension hyperplane. Using the Pareto front hyperplane, and the relationship between weights and resulting objectives, an optimal individual can be found for a given Mach number. This individual represents a fixed geometry, which is only optimized at a single flight speed. To observe how this optimal geometry changes as Mach number increases, three optimal fixed geometries are found using flight speeds of M_∞=1.5, M_∞=2.5 and M_∞=3.5. At most flight speeds, each of the three exchange inlet components (center body, fairings & cowl) generate shock waves, which affect the air mass flow and total pressure recovery objectives.

The results of the fixed geometries show that at lower Mach numbers (M_∞ <2.3) the air flow into the inlet becomes choked. In addition, the optimal geometry at M_∞=1.5 shows having a wider fairing profile results in a strong (normal) fairing shock, which eliminates the cowl shock. This results in 11% and 14% higher performance in the $\dot{m}_a$ and $\overline{P_o}$ objectives respectively vs the M_∞=2.5 optimal design at the same flight speed (M_∞=1.5). The M_∞=2.5 optimal design shows a weaker fairing shock and, therefore, results in a cowl shock at the same flight speed (M_∞=1.5) in its off-design condition. The additional cowl shock, thereby, reduces its performance.

The M_∞=3.5 optimal design also shows a wider fairing profile was beneficial at higher Mach numbers (M_∞ >3.2). The M_∞=2.5 optimal design is also compared at an off-design condition (M_∞=3.5) to the M_∞=3.5 optimal design. The results show that the M_∞=3.5 optimal design has better performance (12% in $\dot{m}_a$ and 19% in $\overline{P_o}$), as the stronger fairing shock, stemming from its wider profile, reduces the

subsequent cowl shock strength. The M_∞=2.5 optimal design had the narrowest fairing profile, which results in a weaker fairing shock at the off-design condition of M_∞=3.5, however, this results in a stronger cowl shock, which reduces its performance vs the M_∞=3.5 optimal design at Mach numbers > 3.2. A narrower fairing profile may appear desirable, due to its resulting weaker shock wave; however, this only serves to increase the strength of the cowl shock. This results in varying performance based on the freestream Mach number. Therefore, this indicates that there is a careful balance between the strength of the fairing and cowl shock waves (the center body oblique shocks had only minimal effects).

The M_∞=2.5 optimal design shows the best overall performance for a fixed geometry over the supersonic range tested. It has superior performance between $2.0 \leq M_\infty \leq 3.2$ and although it did not perform as well as the other two fixed geometries at high and low Mach numbers, it did not show a rapid fall off in objectives outside of its optimal range. This rapid fall off is seen for the high and low Mach number optimal designs. A variable geometry could have maximum performance at all Mach numbers, however, the additional complexity of moving parts and added weight would not justify such minimal increase in performance over such a narrow range of flight speeds. Therefore, a fixed geometry based on the M_∞=2.5 optimal design is selected as the optimal geometry for the supersonic range.

5.2 Recommendations

Recommendations for future work include the determination of constraints on the objectives, particularly on the turn angle ϕ, and CFD validation of the optimal geometries presented. The selection of the optimal design for any flight speed is based on a trade-off involving the design objectives, mainly $\dot{m}_a$ and the turn angle ϕ. As shown in the selection of the M_∞=2.5 optimal design, the turn angle of $\phi = 39.64°$

is selected as an acceptable trade-off. However, further work needs to be conducted on the rocket path to determine constraints on the turn angle objective, to determine if this angle is indeed acceptable. Similarly, minimum values for air mass flow $\dot{m}_a$, total pressure recovery $\overline{P_o}$, and arc length L_{arc} should to be determined. This will eliminate designs that do not fall within the constraints. By having a narrower range of designs, a higher resolution of genes and weights can be explored without adding excessive computational time. In addition, each of the optimal designs presented in this work should be validated using CFD analysis to ensure that the results from the supersonic estimation method are still valid for these very distinct geometries.

Future recommendations also include comparing the selected supersonic optimal design with the previous subsonic optimal designs to further evaluate their off-design performance. If the off-design conditions show radical differences in the performance objectives, then a future optimization should be conducted in the transonic range, to evaluate if there is an optimal compromise between the two designs. The external geometry creation results in a vertical leading edge for the fairing. This design is based on a subsonic model, where analysis showed that a sloped leading edge could result in air passing around the inlet rather than into it. However, future work should be done to investigate alternate configurations on the leading edge of the fairing at supersonic speeds. This may include sloping the leading edge of the fairing such that it blends into the center body.

Small scale wind tunnel testing could be done on the external geometry using 3D printed models. For full scale testing, a feasibility study should also be conducted into potential methods of how this geometry could be created with an internal rocket path. This study would need to address both manufacturing techniques, as well as materials that are suitable for both the structural and thermal limits of the vehicle. These limits were considered for the external geometry when selecting the flight trajectory using a constant dynamic pressure of 30 kPa.

List of References

[1] S. R. Turns. *An Introduction to Combustion: Concepts and Applications*. McGraw Hill, New York, 3 edition (2011).

[2] D. R. Greatrix. *Powered Flight-The Engineering of Aerospace Propulsion*, chapter 13, pages 435–456. Springer-Verlag London Limited, London, U.K. ISBN 978-1-4471-2484-9 (2012).

[3] S. Post. *Applied and Computational Fluid Mechanics*, chapter 8, pages 395–397. Jones and Bartlett Publishers LLC, Sudbury,MA. ISBN-13 978-1-934015-47-6 (2011).

[4] R. Daines and C. Segal. "Combined rocket and air breathing propulsion systems for space-launch applications." *Journal of Propulsion and Power* **14**(5), 605–612 (1998).

[5] NASA. "Armstrong fact sheet: SR-71 blackbird." Accessed online Sept 2017. Https:// www.nasa.gov/ centers/armstrong/news/FactSheets/ FS-030-DFRC.html (2014).

[6] C. Segal. *The Scramjet Engine*. Cambridge University Press, New York, N.Y. ISBN 978-1-107-40252-2 (2009).

[7] NASA. "NASA's X43A news release." Accessed online Sept 2017. Https:// www.nasa.gov/ missions/research/ x43-main.html (2004).

[8] J. C. Whitehead. "Airbreathing acceleration toward earth orbit." 43rd AIAA/ASME/SAE/ASEE Joint Propulsion Conference and Exhibit Cincinnati, OH, Lawrence Livermore National Laboratory, Livermore, CA 94551. AIAA-2007-5837 (2007).

[9] NASA. "Advanced space transportation program: Paving the highway to space." Accessed online June 2017. Https:// www.nasa.gov/ centers/marshall/news/background/ facts/astp.html (2008).

[10] NASA Glenn Research Center. "Specific impulse." Accessed online June 2017. Https:// www.grc.nasa.gov/ www/k-12/ airplane/ specimp.html (2015).

[11] W. Huang, L. Yan, and J. guo Tan. "Survey on the mode transition technique in combined cycle propulsion systems." *Aerospace Science and Technology* **39**, 685–691 (2014).

[12] M. Chen, Z. L. Zhu, H. L. Tang, D. M. Zhu, and J. Zhang. "Mode transition study of turbine-based combined cycle engine concepts." 43rd AIAA/ASME/SAE/ASEE Joint Propulsion Conference & Exhibit Cincinnati, OH, Beihang University, Beijing, China. AIAA-2007-5374 (2007).

[13] J. T. Csank and T. J. Stueber. "A turbine based combined cycle engine inlet model and mode transition simulation based on hitecc tool." Technical Report 217714, NASA Glenn Research Center, Cleveland, Ohio (2012).

[14] J. Liu, H. Yuan, Z. Hua, W. Chen, and N. Ge. "Experimental and numerical investigation of smooth turbine-based combined-cycle inlet mode transition." *Aerospace Science and Technology* **60**, 124–130 (2017).

[15] E. Gamble, D. Haid, S. D'Alessandro, and R. DeFrancesco. "Dual-mode scramjet performance model for tbcc simulation." AIAA-2009-5298, Denver, Colorado (2009).

[16] V. V. Balepin, P. A. Czysz, and R. H. Moszee. "Combined engine for reusable launch vehicle (klin cycle)." *Journal of Propulsion and Power* **17**(6), 1239–1346 (2001).

[17] T. M. Krivanek, J. M. Roche, and J. P. Riehl. "Affordable flight demonstration of the gtx air-breathing SSTO vehicle concept." Technical Report 212315, NASA Glenn Research Center, Cleveland, Ohio (2003).

[18] W. Escher, F. Hyde, and D. Anderson. "A user's primer for comparative assessments of all-rocket and rocket-based combined-cycle propulsion systems for advanced earth-to-orbit space transport applications." 31st Joint Propulsion Conference and Exhibit, Joint Propulsion Conferences, San Diego,CA. AIAA paper 95-2474 (1995).

[19] W. H. Heiser. "Ejector thrust augmentation." *Journal of Propulsion and Power* **26**(6), 1325–1329. Technical Notes (2010).

[20] M. N. Jahingir and Z. Huque. "Design optimization of rocket-based combined-cycle inlet/ejector system." *Journal of Propulsion and Power* **21**(4), 650–655 (2005).

[21] Q. Yang, W. Shi, J. Chang, and W. Bao. "Maximum thrust for the rocket-ejector mode of the hydrogen fueled rocket-based combined cycle engine." *International Journal of Hydrogen Energy* **40**(9), 3771–3776 (2015).

[22] W. Presz, G. Reynolds, and C. Hunter. "Thrust augmentation with mixer/ejector systems." page 10. 40th AIAA Aerospace Sciences Meeting & Exhibit, Reno, NV. AIAA 2002-0230 (2002).

[23] S. Yungster and C. Trefny. "Analysis of a new rocket-based combined-cycle engine concept at low speed." Technical Report 209393, Institute for Computational Mechanics in Propulsion, NASA Glenn Research Center, Cleveland, Ohio. AIAA 99-2393 (1999).

[24] W. Escher and R. E. Schnurstein. "A retrospective on early cryogenic primary rocket subsystem designs as integrated into rocket-based-combined-cycle (RBCC) engines." 29th Joint Propulsion Conference, Monterey,CA. AIAA paper 93-1944 (1993).

[25] L. Shi, X. Liu, G. He, F. Qin, X. Wei, B. Yang, and J. Liu. "Numerical analysis of flow features and operation characteristics of a rocket-based combined-cycle inlet in ejector mode." *Acta Astronautica* **127**, 182–196 (2016).

[26] A. Gerber. *Numerical Investigation of a Novel RBCC Ejector Configuration Compared to a Traditional Circular Ejector*. Master's thesis, Carleton University, Ottawa, Ontario, Canada (2015).

[27] J. Etele, S. Hasegawa, and S. Ueda. "Experimental investigation of an alternative rocket configuration for rocket-based combined cycle engines." *Journal of Propulsion and Power* **30**(4), 944–951 (2014).

[28] J. Etele, M. Kodera, and S. Ueda. "Experiments with ejector rocket entrainment." *Journal of Propulsion and Power* **32**(5), 1110–1118 (2016).

[29] L. Yang, H. Guo-qiang, L. Pei-jin, and L. Xiang. "Selection of ejector-ramjet mode transition interval on RBCC." *Journal of Solid Rocket Technology* **32**(5), 500–505 (2009).

[30] W. Huang, L. Ma, M. Pourkashanian, D. B. Ingham, S. bin Luo, J. Liu, and Z. guo Wang. "Flow-field analysis of a typical hydrogen-fueled dual-mode scramjet combustor." *Journal of Aerospace Engineering* **25**(3), 336–346 (2012).

[31] L. Shi, G. He, F. Qin, and X. Wei. "Numerical study of a boundary layer bleedfor a rocket-based combined-cycle inlet in ejector mode." *International Journal of Turbo and Jet-Engines* **31**(4), 347–359 (2014).

[32] NASA Glenn Research Center. "Inlet performance." Accessed online August 2017. Https:// www.grc.nasa.gov /www/k-12/ airplane/ inleth.html (2015).

[33] D. Reddy and D. Sree. "Computational study of flow in a rocket-based combined cycle (RBCC) engine inlet." *Computers & Fluids* **35**(7), 724–732 (2006).

[34] D. Cerantola. *Rocket Nozzle Design with Ejector Effect Potential*. Master's thesis, Carleton University, Ottawa, Canada (2007).

[35] T. Waung. *An Ejector Air Intake Design Method for a Novel Rocket Based Combined-Cycle Rocket Nozzle*. Master's thesis, Carleton University, Ottawa, Canada (2010).

[36] A. Murzionak. *Rocket Based Combined Cycle Exchange Inlet Performance Estimation at Supersonic Speeds*. Master's thesis, Carleton University, Ottawa, Ontario, Canada (2013).

[37] J. Anderson. *Fundamentals of Aerodynamics*, chapter 1, pages 6–8. McGraw Hill, New York. ISBN 0-07-001656-9 (1984).

[38] J. Anderson. *Computational Fluid Dynamics, The Basics with Applications*, chapter 1, pages 3–32. McGraw Hill, New York. ISBN 978-1-25-902596-9 (1995).

[39] M. Zucrow and J. Hoffman. *Gas Dynamics*, volume 1, chapter 7, pages 327–421. John Wiley & Sons, New York. ISBN 0-471-98440-X (1976).

[40] D. Goldberg. *Genetic Algorithms in Search, Optimization, and Machine Learning*. Addison-Wesley Publishing Company. ISBN ISBN 0-201-15767-5 (1988).

[41] X. Yang. *Nature-Inspired Optimization Algorithms*. Elsevier, London, U.K. ISBN ISBN-13 978-0-12-416743-8 (2014).

[42] J. P. Li, M. E. Balazs, and G. T. Parks. "Engineering design optimization using species conserving genetic algorithm." *Engineering Optimization* **39**(2), 147–161 (2007).

[43] G. Chorkawy. *Exchange Inlet Design Optimization by Genetic Algorithm.* Master's thesis, Carleton University, Ottawa, Ontario (2011).

[44] S. Farahat, S. M. Javadpour, H. Hamidi, and E. Kadivar. "Optimization of a supersonic wind tunnel diffuser using genetic algorithm." *Engineering Computations* **32**(6), 1691–1707 (2015).

[45] W. Huang, S. bin Li, L. Yan, and J. guo Tan. "Multiobjective design optimization of a cantilevered ramp injector using the surrogate-assisted evolutionary algorithm." *Journal of Aerospace Engineering* **28**(5), 1–8 (2015).

[46] W. Huang, J. Yang, and L. Yan. "Multi-objective design optimization of the transverse gaseous jet in supersonic flows." *Acta Astronautica* **93**, 13–22 (2014).

[47] H. Ogawa and R. R. Boyce. "Physical insight into scramjet inlet behavior via multi-objective design optimization." *AIAA Journal* **50**(8), 1773–1783 (2012).

[48] V. Ahuja and R. J. Hartfield. "Optimization of combined rocket and ramjet/scramjet ballistic missile designs." *Journal of Propulsion and Power* **31**(6), 1544–1550 (2015).

[49] M. Bessaou and P. Siarry. "A genetic algorithm with real-value coding to optimize multimodal continuous functions." *Structural and Multidisciplinary Optimization* **23**(1), 63–74 (2001).

[50] R. Storn and K. Price. "Differential evolution a simple and efficient heuristic for global optimization over continuous spaces." *Journal of Global Optimization* **11**(4), 341–359 (1997).

[51] M. Khademi, P. Setoodeh, M. Rahimpour, and A. Jahanmiri. "Optimization of methanol synthesis and cyclohexane dehydrogenation in a thermally coupled reactor using differential evolution (DE) method." *International Journal of Hydrogen Energy* **34**(16), 6930–6944 (2009).

[52] A. D. Olds, C. A. Kluever, and M. L. Cupples. "Interplanetary mission design using differential evolution." *Journal of Spacecraft and Rockets* **44**(5), 1060–1070 (2007).

[53] D. Pastrone and M. R. Sentinella. "Multi-objective optimization of rocket-based combined-cycle engine performance using a hybrid evolutionary algorithm." *Journal of Propulsion and Power* **25**(5), 1140–1145 (2009).

[54] T. Tusar and B. Filipic. "Differential evolution versus genetic algorithms in multiobjective optimization." In S. Obayashi, K. Deb, C. Poloni, T. Hiroyasu, and T. Murata, editors, "Evolutionary Multi-Criterion Optimization," page 257. International Conference on Evolutionary Multi-Criterion Optimization, Lecture Notes in Computer Science, vol 4403. Springer, Berlin, Heidelberg, Matsushima, Japan (2007).

[55] A. Deb, J. S. Roy, and B. Gupta. "Performance comparison of differential evolution, particle swarm optimization and genetic algorithm in the design of circularly polarized microstrip antennas." *IEEE Transactions on Antennas and Propagation* **62**(8), 3920–3928 (2014).

[56] E. P. dos Santos Amorim, C. R. Xavier, R. S. Campos, and R. W. dos Santos. "Comparison between genetic algorithms and differential evolution for solving the history matching problem." In B. Murgante, editor, "Computational Science and Its Applications-ICCSA 2012," page 635. ICCSA 2012, Lecture Notes in Computer Science, vol 7333. Springer, Berlin, Heidelberg, Brazil (2012).

[57] I. Y. Kim and O. de Weck. "Adaptive weighted sum method for multiobjective optimization: a new method for pareto front generation." *Structural and Multidisciplinary Optimization* **31**(2), 105–116 (2006).

[58] R. T. Marler and J. S. Arora. "The weighted sum method for multi-objective optimization: new insights." *Structural and Multidisciplinary Optimization* **41**(6), 853–862 (2010).

[59] M. Ehrgott. *Multicriteria optimization*. Springer, Berlin, 2 edition. ISBN 9783540276593 (2005).

[60] I. Steponavičė, R. J. Hyndman, K. Smith-Miles, and L. Villanova. "Dynamic algorithm selection for pareto optimal set approximation." *Journal of Global Optimization* **67**(1), 263–282 (2017).

[61] N. K. Madavan. "Multiobjective optimization using a pareto differential evolution approach." page 1145. Evolutionary Computation, 2002. CEC 2002. Proceedings of the 2002 Congress, Honolulu (2002).

[62] M. Li and X. Yao. "What weights work for you? adapting weights for any pareto front shape in decomposition-based evolutionary multi-objective optimisation." Cornell University Library (2017).

[63] R. Storn, K. Price, and J. Lampinen. *Differential Evolution - A Practical Approach to Global Optimization*. Springer-Verlag, Berlin. ISBN ISBN-13 978-3-540-20950-8 (2005).

[64] C. Lin, A. Qing, and Q. Feng. "A comparative study of crossover in differential evolution." *Journal of Heuristics* **17**, 675–703 (2011).

[65] M. Weber and F. Neri. "Contiguous binomial crossover in differential evolution." *Swarm and Evolutionary Computation* **7269**, 145–153 (2012).

[66] R. Mallipeddi and P. Suganthan. "Empirical study on the effect of population size on differential evolution algorithm." page 3663. Proceedings of the 2008 IEEE Congress on Evolutionary Computation, Hong Kong, China (2008).

[67] J. Ronkkonen, S. Kukkonen, and K. Price. "Real-parameter optimization with differential evolution." page 506. Proceedings of the 2005 IEEE Congress on Evolutionary Computation, Edinburgh, Scotland, UK (2005).

[68] M. Weber, F. Neri, and V. Tirronen. "A study on scale factor in distributed differential evolution." *Information Sciences* **181**, 2488–2511 (2011).

[69] D. Zaharie. "Critical values for the control parameters of differential evolution algorithms." page 62. Institute of Automation and Computer Science, Proceedings of MENDEL 8th international conference on soft computing, Brno, Czech Republic (2002).

[70] D. Zaharie. "Influence of crossover on the behavior of differential evolution algorithms." *Applied Soft Computing* **9**, 1126–1138 (2009).

[71] J. Montgomery and S. Chen. "An analysis of the operation of differential evolution at high and low crossover rates." Proceedings of the IEEE Congress on Evolutionary Computation, Barcelona, Spain (2010).

[72] S. Das and P. Suganthan. "Differential evolution: A survey of the state-of-the-art." *IEEE Transactions on Evolutionary Computation* **15**(1), 4–31 (2011).